



HAL
open science

ZnSnN₂ thin films for photovoltaic applications

Fahad Alnjiman

► **To cite this version:**

Fahad Alnjiman. ZnSnN₂ thin films for photovoltaic applications. Materials Science [cond-mat.mtrl-sci]. Université de Lorraine, 2018. English. NNT : 2018LORR0296 . tel-02109767

HAL Id: tel-02109767

<https://hal.univ-lorraine.fr/tel-02109767>

Submitted on 25 Apr 2019

HAL is a multi-disciplinary open access archive for the deposit and dissemination of scientific research documents, whether they are published or not. The documents may come from teaching and research institutions in France or abroad, or from public or private research centers.

L'archive ouverte pluridisciplinaire **HAL**, est destinée au dépôt et à la diffusion de documents scientifiques de niveau recherche, publiés ou non, émanant des établissements d'enseignement et de recherche français ou étrangers, des laboratoires publics ou privés.



AVERTISSEMENT

Ce document est le fruit d'un long travail approuvé par le jury de soutenance et mis à disposition de l'ensemble de la communauté universitaire élargie.

Il est soumis à la propriété intellectuelle de l'auteur. Ceci implique une obligation de citation et de référencement lors de l'utilisation de ce document.

D'autre part, toute contrefaçon, plagiat, reproduction illicite encourt une poursuite pénale.

Contact : ddoc-theses-contact@univ-lorraine.fr

LIENS

Code de la Propriété Intellectuelle. articles L 122. 4

Code de la Propriété Intellectuelle. articles L 335.2- L 335.10

http://www.cfcopies.com/V2/leg/leg_droi.php

<http://www.culture.gouv.fr/culture/infos-pratiques/droits/protection.htm>

THÈSE

Pour l'obtention du titre de

DOCTEUR de L'UNIVERSITÉ DE LORRAINE

Spécialité : Physique – Nanoscience

Présentée par

Fahad ALNJIMAN

ZnSnN₂ thin films for photovoltaic applications

Soutenance publique prévue le 21 Décembre 2018 à Nancy devant le jury composé de :

Angelique BOUSQUET	Rapporteur	Maitre de conférences – HDR, Institut de Chimie de Clermont-Ferrand, Université Clermont Auvergne – CNRS
Thomas FIX	Rapporteur	Chargé de recherche - HDR, Laboratoire ICUBE, Université Strasbourg – CNRS
Marie-Paule BESLAND	Examineur	Directeur de recherche, Institut des Matériaux de Nantes Jean Rouxel, Université de Nantes – CNRS
Frederic SANCHETTE	Examineur	Professeur, Institut Charles Delaunay, Université de Technologie de Troyes – CNRS
Jean-François PIERSON	Co-directeur de thèse	Professeur, Institut Jean Lamour, Université de Lorraine – CNRS
Patrice MISKA	Directeur de thèse	Maître de Conférences - HDR, Institut Jean Lamour, Université de Lorraine – CNRS

بِسْمِ اللَّهِ الرَّحْمَنِ الرَّحِيمِ

وَمَا أُوتِيتُمْ مِّنَ الْعِلْمِ إِلَّا قَلِيلًا

To my family
To my Mother

Acknowledgements

First, I would like to express my sincere gratitude to my supervisor Mr Patrice Miska for the continuous support of my Ph.D work and for our discussion, his patience, motivation, enthusiasm and knowledge.

Also, I wish to express my gratitude to my co-supervisor(frero) or my big brother Pr.Jean-François Pierson for providing me the opportunity to develop this work. He was always willing to share any ideas with me. Only through his fruitful discussion, strong experience and hard work, the completion of this thesis became possible.

I would like to thank to the members of the jury for agreeing to participate in my PhD defense.

A very special thanks goes out to Mr. Jaafar Ghanbaja, Ms. Stéphanie Bruyere, Ms. Sandrine Mathieu and Ms. Christine Gendarme for their important contribution during my PhD thesis.

I also want to express my great thanks to Ms. Sylvie Migot for his TEM sample preparation by FIB always in a short time.

Also, A very special thanks goes out to Mr. Sébastien Diliberto and Mr. Pascal Boulet for their important contribution during my PhD thesis

In the case of administration, I am grateful for the help from Valérie Tamburini, Valérie Madeline and the big boss Thierry Belmonte.

Special thank to Mr. Abdelkrim Redjaïmia for the discussions.

I would like to start to thanks all my friends in the lab and I hope that I will not forget one of them : First, I will start with PVD dream team, David Pilloud, Silvère Barrat, Alan Corvisier, Fabien Capon, David Horwat, Alaa Eldin Giba, Benjamin Gilbert, William Chamorro, Manuel Tresse, Martin Mickan, Emile Haye, Claudia De Melo Sanchez, Alejandro

Borroto, Alexis Garcia Wong, WANG Yong, Agathe Virfeu, Christophe Celindano, Joseph Antoine, Nicole Beddelem, Daria Kharkhan, Christy Fadel, Aurelien Didelot, Aurelien Etiemble and Osama Madkhali.

A very special thanks to Kosseila Ait Oukaci, Dorra Ibrahim, Hiba Kabbara, Saïma Siouane, Turki Alshammari, Osama Madkhali, Mahmoud Trad, Soufiane EL OUALID, Selma Sassi, Enaam Jamal Al Dine, Meriem Ben Haj Slama, Ziad Al Hallak, Zied Ferjaoui, Firas Abdel Hamid, Brigitte vigolo, Pascale Corne, Tom Ferte, Pauline Vilasi, and Abdallah Imam. All my friends from Saudi Arabia here in Nancy and all of my friends there.

Thanks the lab Institut Jean Lamour to give me the access to use so many equipments. Thanks the Saudi Arabia Embassy in France for the PhD grant.

Finally, I would like to thank my wife for sharing and spurting all the moments of study also my brother Majed and all my family. Thanks to my father. Also thanks to part of my heart Mohammed, Zainab and Youssef.

Contents

General introduction	1
Chapter 1. Zinc tin nitride: a new material with large applications for photovoltaics	5
1.1 Introduction	5
1.1.1 Context, Positioning and Objectives of the Work: The Need of New Material Developments.....	5
1.1.2 The Question of Realization Complexity and Indium Supply Shortage vs. Industrial Needs	5
1.1.3 Photovoltaics concerns.....	6
1.1.4 PV technologies	7
1.2 Potentialities of New ZnSnN₂ Material Physical Properties	10
1.2.1 ZnSnN ₂ historical aspects: an overview.....	11
1.2.2 Focus on the issue of the crystal structure.	14
1.2.3 The issue of the electronic structure, defects and band gap	19
1.3 Conclusion	23
References	25
Chapter 2. Synthesis of zinc tin nitride thin films and characterization methods.....	31
2.1 Introduction	31
2.2 Zinc tin nitride thin film growth	31
2.3 Structure zone diagram (SZD).....	33
2.4 Elaboration setup.....	34
2.5 X-ray diffraction (XRD).....	35
2.6 X-ray energy dispersive spectroscopy (EDS) and scanning electron microscopy (SEM)...	37
2.7 Conversion electron Mössbauer spectroscopy	38
2.8 Transmission electron microscopy (TEM).....	40
2.9 Four-point probe method.....	41
2.10 Hall effect measurements.....	42
2.11 UV-visible spectroscopy	43
2.12 Ellipsometry	46
2.13 X-ray photoelectron spectroscopy (XPS)	47
2.14 Conclusion	48
References	49
Chapter 3. ZnSnN₂ Thin Films: Synthesis and characterization	53
3.1 First attempt to grow zinc tin nitride thin films by PVD.....	53
3.1.1 Growth of ZnSnN ₂ by controlling the discharge current	53

3.1.2 Growth of ZnSnN ₂ by fixing the discharge voltage	55
3.1.3 Growth of ZnSnN ₂ by controlling the discharge voltage in a pure nitrogen plasma.....	57
3.1.4 Effect of the substrate nature.....	60
3.2 Crystalline ZnSnN₂ thin films structure, microstructure, physical and chemical properties	
.....	61
3.2.1 Introduction	61
3.2.2 Chemical composition.....	62
3.2.3 Structure of ZnSnN ₂ films.....	62
3.2.4 Microstructure and morphology of ZnSnN ₂ thin films	64
3.2.5 X-ray photoelectron spectroscopy analysis of ZnSnN ₂ thin films	68
3.2.6 Mossbauer spectrometry of ZnSnN ₂ thin films	70
3.2.7 Electrical and optical properties of ZnSnN ₂	71
3.3 Effect of base pressure before the film growth	76
3.4 Conclusion	82
Reference	84
Chapter 4 Microstructure and tuning the structure of ZnSnN₂ thin films	91
4.1 Focus on the structure of ZnSnN₂	91
4.1.1 Orthorhombic, monoclinic or hexagonal structures	91
4.1.2 Monoclinic vs orthorhombic	92
4.1.3 Monoclinic versus hexagonal phases	95
4.2 Tuning the structure of ZnSnN₂.....	98
4.2.1 Tuning the structure with the stoichiometry	98
4.2.2 Tuning the structure by changing the pressure	103
4.3 Conclusion	113
References	117
General conclusions	120

General introduction

The development of renewable energy sources is of an utmost importance for our societies. It is also a political issue due to the global warming. The optoelectronic industry is growing mainly based on the use of specific class of materials. If the classical GaN UV LEDs are well mastered, it is important to find and develop alternative materials. Such demand is also growing in the field of photovoltaic. Solar energy will be one of the main part of renewable energy system. To fulfil the challenging issues and to develop new markets the discover of new materials is essential.

III-V materials are commonly used as active layers in LEDs, transistors, solar cells and mechanical devices. The main spinneret is based on the use of InGaN alloys. However, such layers contain indium and gallium. Significant volatility in their price and supply over the past years has led to considerable concern given their critical roles and their use in a wide range of large-scale electronic devices. Moreover, at present the crystalline III-V materials require the use of epitaxial growth techniques with high cost and high complexity. It is important to study and develop new earth abundant materials with optimized properties for the realization of innovative optoelectronic devices that could be competitive cost for mass production.

In this work, we aim at developing a new kind of inexpensive, indium/gallium-free, nitride material. It could be the basis of new way for optoelectronic applications. The study of such very innovative material is an ambitious goal but has already started in various countries (China, India, USA) with different groups involved. The studies are focusing on the family of Zn-IV-N₂ alloys that is promising as its bandgap energy could span the solar spectrum and could then replace the InGaN alloys. We have chosen to use reactive magnetron sputtering that is an easily up-scalable production technique with a quite low cost.

Nonetheless, data about these ZnSnN₂ alloys remain scarce and sometimes contradictory. Numerous efforts remain to be done to better understand its fundamental properties. For example, the crystallographic structure of the material is not clearly defined. Additionally, ZnSnN₂ alloys seem to be difficult to control by PVD growth. All these aspects are studied in this work.

In the first chapter of this manuscript we will describe the large context of photovoltaic and few related concerns. Then, we will describe the solutions proposed in literature more especially by developing new materials. Among the recent suggestion found in literature, the

ZnSnN₂ alloy seems to be a good candidate. We will also describe the state of the art about the materials by showing the key points as well as the work that remain to be done.

In the second chapter of this manuscript we will describe the growth and characterization techniques used in this work and that are, for most of them, available on site at the Institut Jean Lamour.

The third chapter is dedicated to the first set of results. After a description of the optimization of the growth process, we will show the results focused on a first approach of the growth at room temperature of highly crystallized ZnSnN₂ thin films. Then we study the effect of the base pressure of the chamber on the structure and the properties of ZnSnN₂ thin films.

The fourth chapter is a focus on the film analysis by high-resolution transmission electron microscopy and electron diffraction. We used the top facility we have at the Institut Jean Lamour to determine the film structure. The second part of this chapter is dedicated to the effect of the film stoichiometry and the total pressure on the films properties.

Chapter 1. Zinc tin nitride: a new material with large applications for photovoltaics.....	5
1.1 Introduction.....	5
1.1.1 Context, Positioning and Objectives of the Work: The Need of New Material Developments	5
1.1.2 The Question of Realization Complexity and Indium Supply Shortage vs. Industrial Needs.....	5
1.1.3 Photovoltaics concerns.....	6
1.1.4 PV technologies	7
1.2 Potentialities of New ZnSnN₂ Material Physical Properties	10
1.2.1 ZnSnN ₂ historical aspects: an overview	11
1.2.2 Focus on the issue of the crystal structure.	14
1.2.3 The issue of the electronic structure, defects and band gap.....	19
1.3 Conclusion	23
References.....	25

Chapter 1. Zinc tin nitride: a new material with large applications for photovoltaics

1.1 Introduction

1.1.1 Context, Positioning and Objectives of the Work: The Need of New Material Developments

The development of alternative materials for photovoltaics has attracted much attention over the last decade and is currently of a crucial importance for our society. A reliable plan for the development of carbon free energy supply has become inevitably important for policy makers in many states all over the world. Regarding the societal context, many research programs are dedicated to new material discovery over the world. I will describe here these aspects.

1.1.2 The Question of Realization Complexity and Indium Supply Shortage vs. Industrial Needs

Although the InGaN route can be promising, large scale III-V (InGaN and InGaAsP) based devices will be limited by the quality of the material (indium incorporation in InGaN for example) but also by the growth technique used (epitaxy). Moreover, the reliance on indium and gallium, with its limited economically viable sources, could potentially limit its long term use in large-scale solar devices. Indeed, indium is primarily and profusely used in TCO for flat screens.

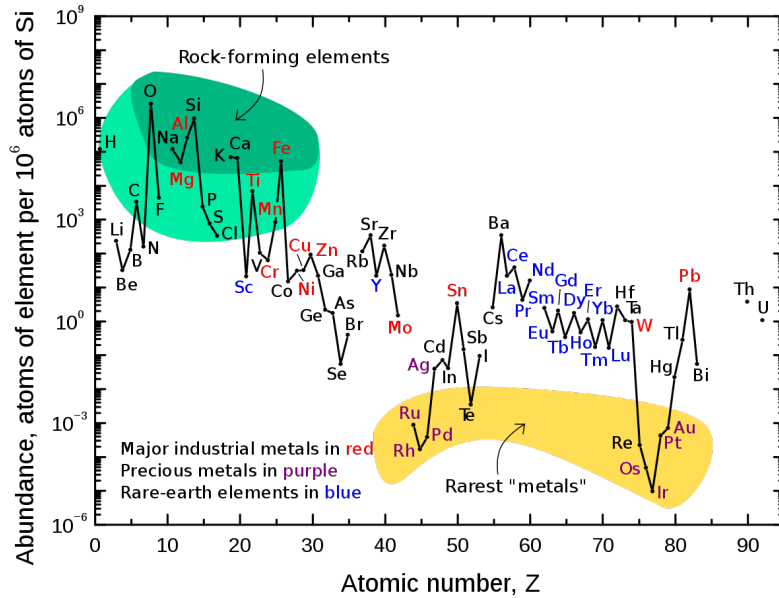


Figure 1.1 Abundance of elements in the Earth's crust as function of their atomic number[1].

The question of the material availability is exposed in many reports. (Figure 1.1) shows for example the abundance of different element in the Earth's crust. The indium is one of the scarcer elements. Indium reserves are then estimated at twenty years at current production rates. Indium recovery processes exist but are of little eco-friendly and energy-intensive concerns. Beyond questioning about its availability, a significant increase in indium price is to be feared due to speculation on raw materials observed in recent years. It is then of utmost importance to develop materials with earth abundant and using large scale growth methods.

1.1.3 Photovoltaics concerns

As the topic of this manuscript is dedicated to materials that could be useful for photovoltaic technologies, it is interesting to give a short description of the frame and of the needs in this field.

The energy demand is still increasing over the world and has reached 13 800 millions of oil equivalent tons according to a study from the International Energy Agency [2]. Among the current offer, a large part of the energy production uses non-renewable resources such as oil, coal, or uranium. On the contrary, the photovoltaic market is now under-developed with a rate of 1.2% of the electricity production. However, this market is rapidly growing because of the policies of the states. A 420 GigaWatts production capacity is now available and the market is growing with a rate of 25% per year (Fig. 1.2)[3].

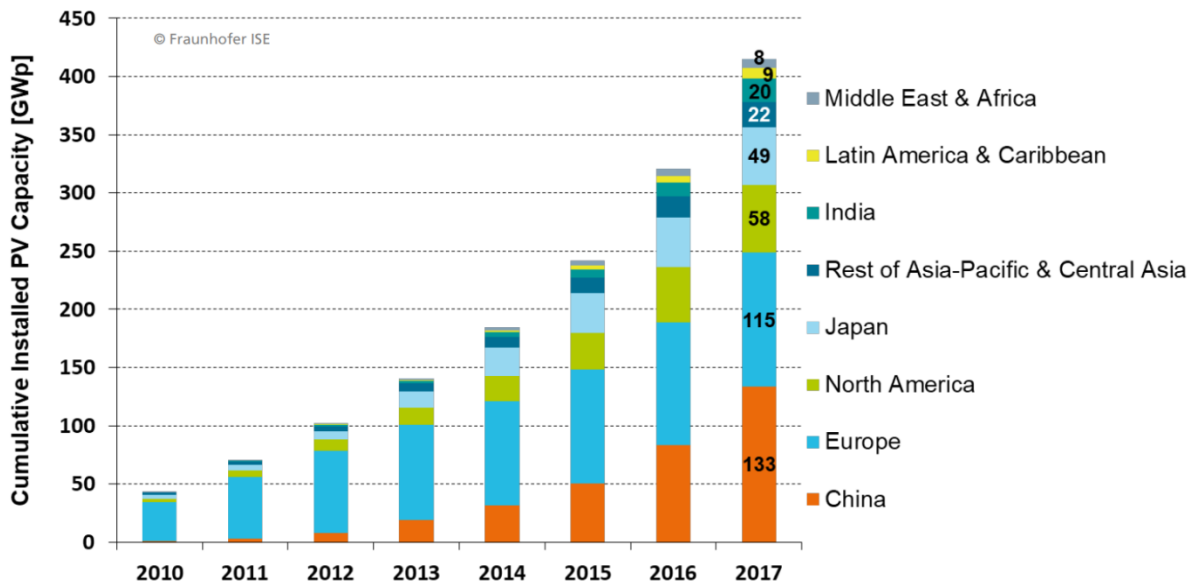


Figure 1.2 Global capacity of solar photovoltaic by some country and region[3].

Nevertheless, efforts still must be done to reach the global objectives of green energy production and for decarbonized energy generation. Among the possibilities, the production of green photovoltaic electricity is deeply studied. Indeed, the energy coming from the sun, an abundant and free source, can be considered as green if the sun energy harvesting technologies can be ecological. This point requires the photovoltaic technology competitiveness improvement to reduce the cost of the electricity produced and to take care of the ecological footprint of technologies used.

1.1.4 PV technologies

In 1839, a French physicist Edmond Becquerel had discovered the photovoltaic effect and he created the first photovoltaic cell in the world[4]. The principle of the photovoltaic is to convert the sunlight into electricity. Absorption of a photon in a material means that its energy is used to excite an electron from an initial energy with level E_i from valence band to a higher energy level E_f in conduction band as shown in Fig. 1.3. The photon energy must be can greater than the band gap energy E_g in order to create an electron-hole pair.

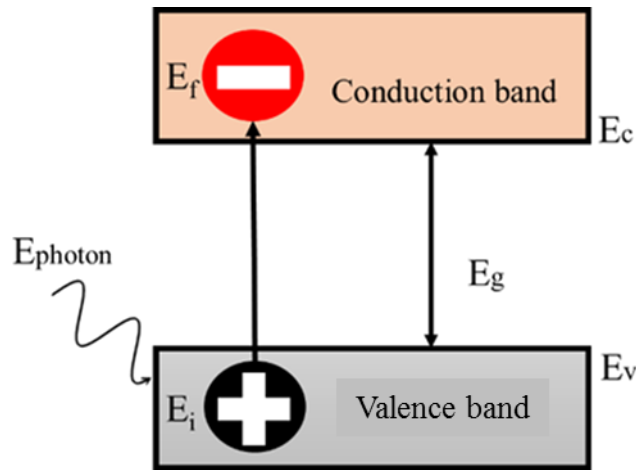


Figure 1.3 Generation of an electron-hole pair by absorption of a photon.

However, there are five main categories of solar cells. They are classified according to the materials used and the fabrication methods. The National Renewable Energy Laboratory (NREL) published every year the best research cell efficiencies charts that includes the evolution with the year for the five main categories shown in fig. 1.4.

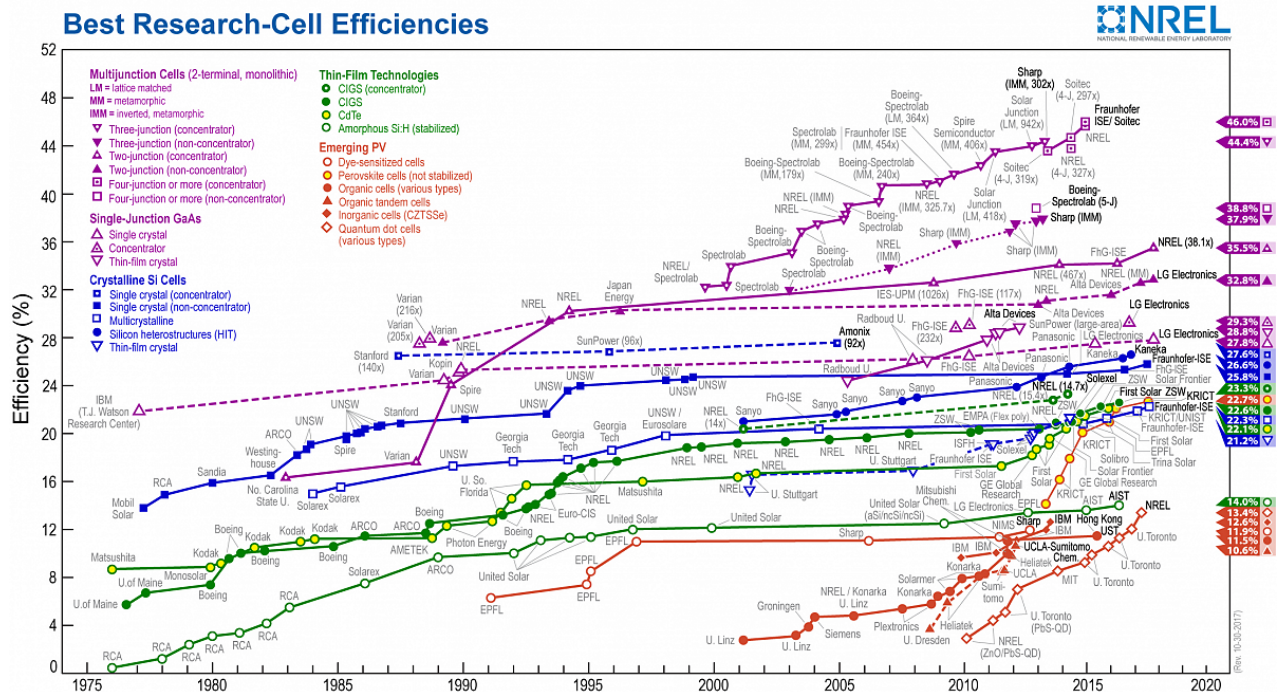


Figure 1.4 National Renewable Energy Laboratory graph of solar cell efficiency over the years.[5].

The five main categories are:

1. Multijunction cells.
2. Single-junction GaAs.
3. Crystalline Si cells.
4. Thin-film technologies.
5. Emerging PV concepts.

Among the possible solar cells, the multijunction one is the most efficient and has the current world record. The multijunction solar cell has multiple p–n junctions made with different semiconductor materials. Each junction creates an electric current in response to different wavelengths of the incoming light. The use of multiple semiconducting materials allows then the absorbance of a wide range of wavelengths. However, the multijunction solar cells have achieved the highest efficiencies performance of approx. 46% [6]. An example for multijunction solar cell shown in Fig. 1.5.

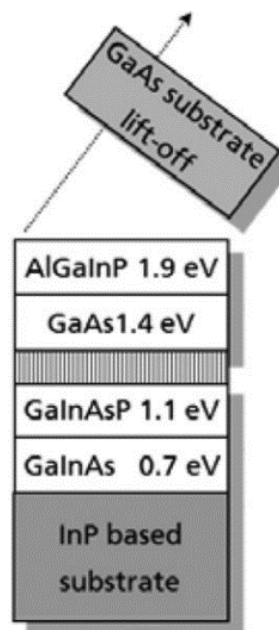


Figure 1.5 Four junction solar cells with efficiency word record at 46.1% [6].

The main problem of this kind of device is its elaboration complexity and the use of materials containing In and Ga as mentioned in section 1.1.2.

Another approach lies in the use of new materials such as $\text{CuInGaS}_2(\text{Se}_2)$ (CIGS). Such an approach has been widely developed in the last 10 years but the efficiencies are still low, around 22 % in laboratory for a 0.5 cm^2 cell with CIGS[7]. Moreover, CIGS cells contain indium that scarcity issue is a real problem. Additionally, these other technologies, that are in front competition with the c-Si one, are also suffering serious problems of toxicity by needing the use of alternative layers containing Cd or scarcity (Te-0.005 ppm and Se-0.05 ppm) for possible TW-scale deployment. Then different alternatives and more or less fruitful solutions have been proposed over the last years to replace the CIGS technology such as the development of $\text{I}_2\text{-II-IV-VI}_4$ materials like e.g. $\text{Cu}_2\text{ZnSnS}_4$ (CZTS). This could be a real interesting approach but unfortunately the efficiencies are also still low around 12%.

Finally, among the emerging technologies, we can quote the organic-inorganic perovskite materials. The efficiency of perovskite is rising today but the highly efficient stable and lead-free perovskite material route constitutes however the strongest challenging way. If the efficiencies are high, the stability of the perovskite is currently low and the realization of a stable device still requires a lot of work, until Turren-Crus [8] on 11-oct-2018 prove and demonstrate the perovskite solar cells are stable with high-performance.

1.2 Potentialities of New ZnSnN_2 Material Physical Properties

In a first approach focused on the study of new materials we would like to open a complementary route using nitrogen based materials. Following the inorganic thin film strategy where the III-N materials have already been proven to be very stable, it is so natural to focus on a still poorly investigated semiconductor material line closely related to the (In,Ga)N family and for which the column III element is replaced by an ordered cation sublattice composed of equal numbers of Zn and column IV (Si, Ge, Sn) atoms.

Zinc tin nitride (ZnSnN_2) is the last compound studied from the family of Zn-IV- N_2 semiconductors, where the IV element can be (Si-Ge-Sn). This compound of Zn-IV- N_2 is closely related to the III-N semiconductors [9],[10] where elements III are (Al-Ga-In). The family of III-nitrides are promising materials for semiconductor devices applications, more especially for optoelectronic applications for a wide range of photon energies. These compounds have optical band gaps of 6.2 eV for AlN, 3.4 eV for GaN and 0.7 eV for InN [11].

Furthermore, what makes these compounds interesting is the possibility of tuning of the band gap through alloying of $\text{III}_x\text{III}_{1-x}\text{N}$. For example $\text{Al}_x\text{Ga}_{1-x}\text{N}$ is a wide bandgap semiconductor reaching the band gap range from 6.2 eV to 3.4 eV by changing the ratio between Al and Ga [12]. The same property is obtained for $\text{In}_x\text{Ga}_{1-x}\text{N}$ with the possibility to tune the band gap range from 3.5 eV and 0.7 eV by using different ratio between In and Ga [13].

Quayle P. et al [14] have compared the band gap energies between these two nitrides families: III-N and Zn-IV-N₂. They reported the band gaps energies versus the material lattice constant (figure 1.6). Such a representation shows the possibility to get adjustable band gap for Zn-IV-N₂, which is then a potential good candidate for replacing the III-N materials.

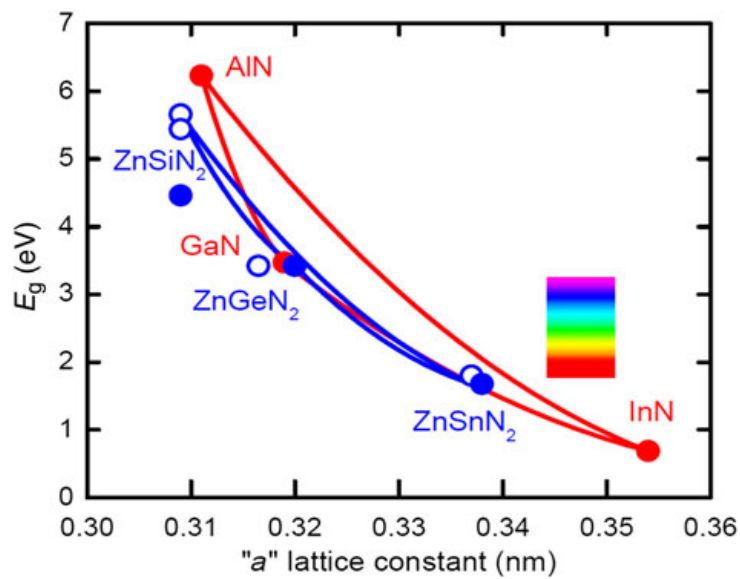


Figure 1.6 The band gaps versus “a” lattice constants for III-nitrides and Zn-IV-nitrides and their alloys.[14].

1.2.1 ZnSnN₂ historical aspects: an overview

ZnSnN₂ is a semiconducting material belonging to the family of Zn-IV-N₂. By changing the IV elements from (Si-Ge-Sn) the band gap and the lattice parameter can be tuned. Historically, Maunaye *et al.* [15] first reported in 1970 the growth of this kind of material, precisely ZnGeN₂. In 1992 Endo *et al.* [16] reported the first growth of ZnSiN₂ by using high-pressure synthesis.

So far, only ZnGeN₂ and ZnSiN₂ alloys have been synthesized and relatively well characterized. As an example we can mention the growth of ZnSiN₂ by MOCVD [17] on

sapphire or SiC substrates. Greater efforts have been devoted to ZnGeN₂: single crystals were obtained by VLS method, thin films were deposited on glass and silicon spray radiofrequency and MOCVD were used for growth on sapphire and SiC [18]

For ZnSnN₂ after the first publication related to the growth of ZnSnN₂ in 2011, the numbers of article published per year has increased as shown in figure 1.7 with data extracted from Web of science [19].

We can mention that ZnSn_xGe_{1-x}N₂ grown by RF sputtering have also shown a real potential for photonic and optoelectronic application, results published in 2015 by A. M. Shing *et al.* [20].

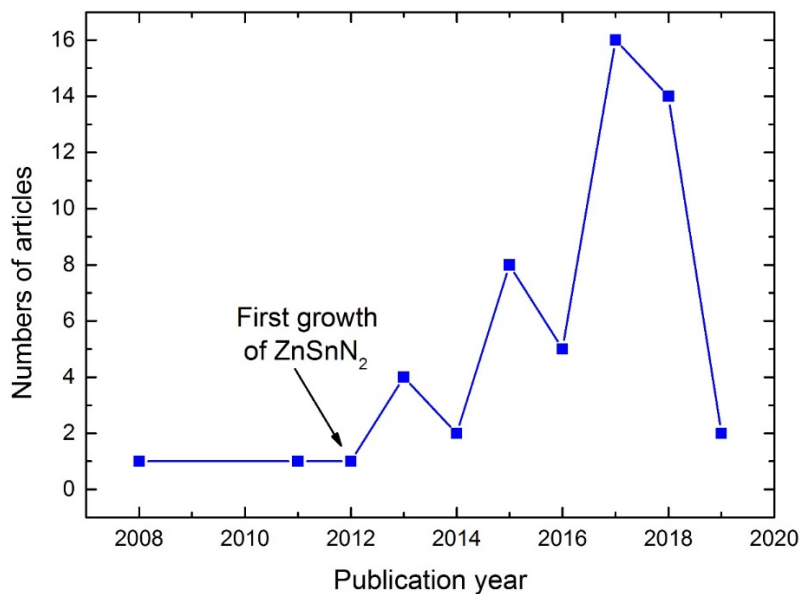


Figure 1.7 Number of articles on ZnSnN₂ published per year based from web of science up to date 18/12/2018.

Experimental studies on ZnSnN₂ are scarcer and the properties of this material are not well known. The first theoretical study has been realized by Paudel *et al.* [9] in 2008.

The first ZnSnN₂ developments in 2011 by N. Feldberg, *et al.* [21] show very interesting and encouraging results. In their study, the material is deposited using a molecular beam epitaxy process. The first experimental results in 2011 [21] and a theoretical study by A. Punya *et al.* [10] explicitly evoked the interest of ZnSnN₂ for optoelectronics.

In 2013, the California Institute of Technology published quite interesting results by L. Lahourcade *et al.* [22]. In particular, the authors presented some optical properties of ZnSnN₂ films obtained by sputtering and exhibiting an experimental band gap of 1.8 eV (Figure 1.8) which is in opposition to the theoretical prediction of 1.42 eV. The authors explain this

deviation with the existence of Burstein-Moss effect due to a significant n-type doping of the order of 10^{21} cm^{-3} . However, this issue remains to be clarified.

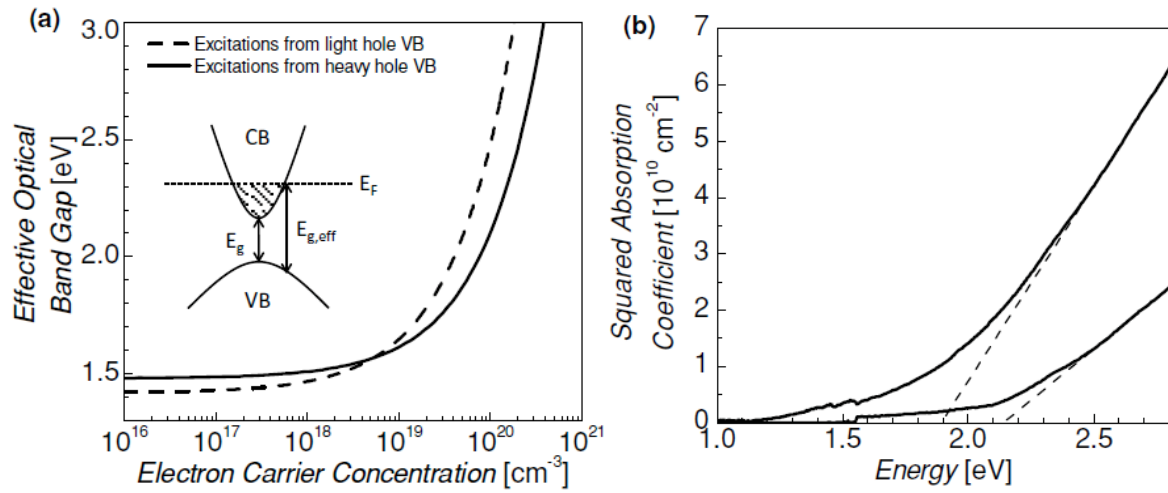


Figure 1.8 (a) Bandgap as a function of the carrier concentration, (b) evaluation of the bandgap and absorption coefficient of ZnSnN₂ by optical measurements [22].

Another study in 2013 also provides some theoretical and experimental optical data of ZnSnN₂ obtained by molecular beam epitaxy assisted by nitrogen plasma [23]. However, the authors contradict the results of the first two studies mentioned above about the crystallographic structure. They found it has a monoclinic structure instead of an orthorhombic as predicted. This change in the crystalline structure impacts the bandgap energy but the question remains open. They also predict the possibility of reducing the forbidden band gap to 0.95 eV related to the cationic disorder, which may allow a greater tuning of the bandgap of the material.

In 2015, a study from a Chinese group has reported electron concentration between 2.3×10^{17} and $1.6 \times 10^{18} \text{ cm}^{-3}$ with band gap estimated in the 1.82-1.95 eV range [24]. This group also revealed that the useful absorption range of the ZnSnN₂ compound is comparable to those of InP, CdTe and GaAs materials (Figure 1.9).

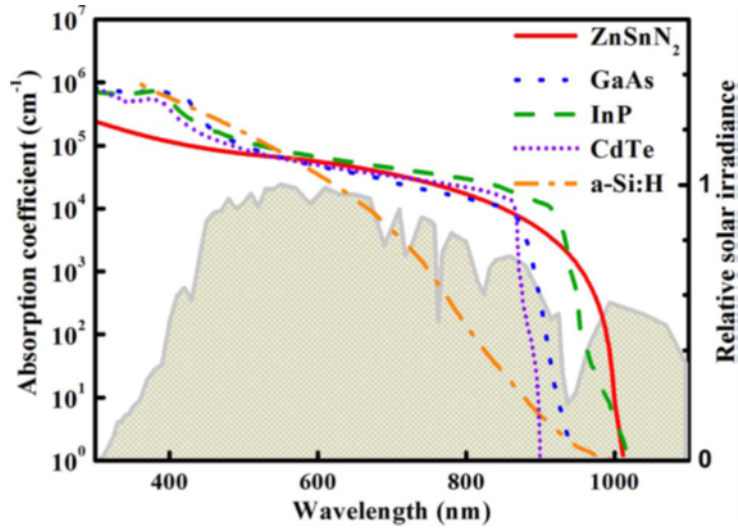


Figure 1.9 Plots of the AM1.5 solar spectrum and the absorption coefficient, comparing the evaluation of the bandgap and absorption coefficient of ZnSnN₂ with others materials [24].

In 2015, carrier densities of 1.8×10^{18} and $4.5 \times 10^{20} \text{ cm}^{-3}$ with the highest mobility being $8 \text{ cm}^2 \text{ V}^{-1} \text{ S}^{-1}$ have been reported. The authors also reported for the first time the possibility of doping control in ZnSnN₂ through varying cation off-stoichiometry [25].

In 2015 again, a paper published by Veal et al. showed the possibility to allow the bandgap variation between 1.33 and 2.38 eV by tuning the degree of cation disorder by varying the growth condition using plasma-assisted MBE [26].

Recently, a Chinese group has reported the high resistivity behavior of ZnSnN₂ sputtered films and also demonstrated satisfactory PN junction I(V) curve which is really encouraging for PV device realization R. Qin *et al.*[27].

1.2.2 Focus on the issue of the crystal structure.

ZnSnN₂ is a semiconductor material that is one of the family of II-IV-N₂. The crystal structure for this new family is considered as wurtzite structure with overall orthorhombic symmetry. T. R. Paudel *et al.* in first-principles study of phonons and related ground-state properties and spectra in Zn-IV-N₂ compounds defined the ideal structure as wurtzite structure with overall orthorhombic lattice vectors a, b and c [9]. Those vectors are related with the wurtzite lattice vectors a^w, b^w and c^w by $a = a^w, b = a^w + 2b^w$ and $c = c^w$.

For ZnSnN₂ the most stable and accepted crystal structure is orthorhombic (fig. 1.10) with 16 atoms per unit cell, 4 atoms of zinc, 4 atoms of tin and 8 atoms of nitrogen. The group

space for the orthorhombic is $Pna2_1$ which is known for β - NaFeO_2 or in general a I-III-VI₂ compound. By DFT calculations T. D. Veal *et al.* [26] have defined the difference between the two structures of the orthorhombic and wurtzite by the ordering in the cation sublattice of ZnSnN_2 . Orthorhombic structure has fully-cation-ordered while the wurtzite one has fully-disordered-cation sublattice.

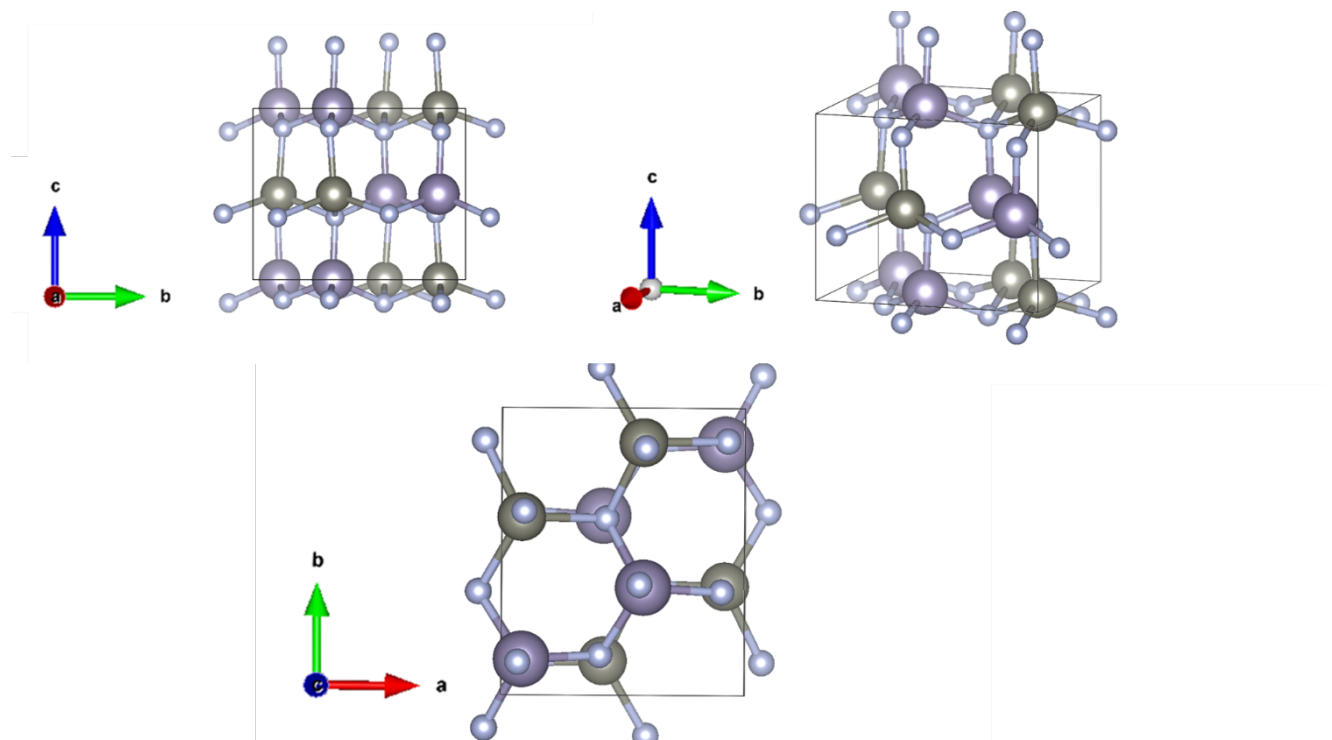


Figure 1.10 Orthorhombic crystal structure of ZnSnN_2 along different directions.

The wurtzite structure of ZnSnN_2 is close to the III-nitride (Al,Ga,In)-N material with hexagonal lattice and space group $P6_3mc$. This structure is known to be that of ZnO. As we mentioned before the wurtzite structure of ZnSnN_2 correspond to disorder cation position with randomly located Zn and Sn atoms. (Figure 1.11).

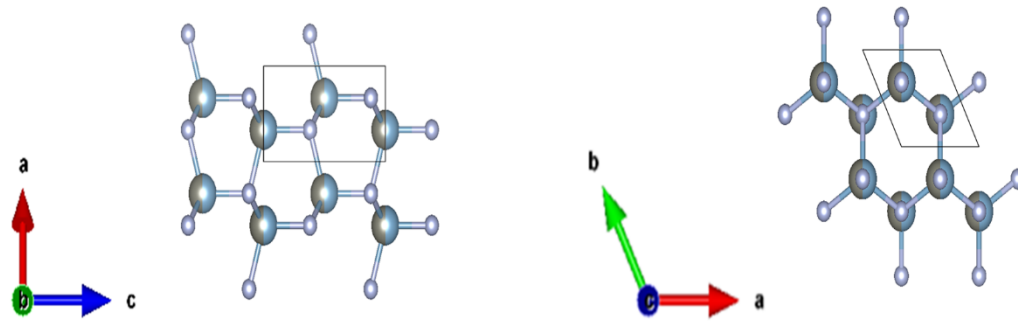


Figure 1.11 Hexagonal crystal structure of $ZnSnN_2$ along different directions.

However, one of the critical challenge is the understanding of the crystal structure of this material. Data extracted from literature and reported in table 1 gathered the information from the debate of previous works of $ZnSnN_2$. The debate is focused on the discussion about the nature of the crystal structure. Nine articles reveal calculations and experimental results showing an orthorhombic structure and seven articles describe a wurtzite one. However, an additional article has described a monoclinic structure but we can see in table 1 that the lattice parameter was very close to the hexagonal structure. Whatever the structure described in the literature, there is no discussion on the effect of the deposition parameters that may favor one specific structure. Indeed, most of the processes used in the literature are not at the thermodynamic equilibrium. Then, metastable structures may be formed.

Table 1. Crystallographic results of ZnSnN₂ in the previous works.

Structure	Calculated parameters (Å)			Experimental parameters (Å)			Reference
	<i>a</i>	<i>b</i>	<i>c</i>	<i>a</i>	<i>b</i>	<i>c</i>	
Orthorhombic	6.76	5.85	5.58	-	-	-	[9]
Orthorhombic	6.76	5.85	5.58	-	-	-	[10]
	6.59	5.70	5.41				
	6.70	5.80	5.53				
Monoclinic	-	-	-	3.395	3.400	5.534	[21]
				$\alpha = 89.885^\circ$	$\beta = 90.033^\circ$	$\gamma = 120.036^\circ$	
Orthorhombic	-	-	-	5.842	6.753	5.462	[14]
Orthorhombic				6.755	5.846	5.473	[23]
Orthorhombic	6.721	5.842	5.459	-	-	-	[22]
Orthorhombic	-	-	-	5.853	6.741	5.498	[24]
Wurtzite	-	-	-	-	-	-	[28]
Orthorhombic	-	-	-	6.721	5.842	5.459	
Wurtzite	-	-	-	6.755	5.846	5.473	[26]
Wurtzite	-	-	-	-	-	-	[29]
Orthorhombic	6.812	5.914	5.542	6.885	5.955	5.577	[30]
Wurtzite	-	-	-	3.366	3.366	5.842	
Orthorhombic	-	-	-	5.842	6.753	5.464	[31]
Wurtzite	-	-	-	3.376	3.376	5.467	
Wurtzite	-	-	-	-	-	-	[27]
Wurtzite	-	-	-	6.885	5.955	5.577	[32]
Orthorhombic	-	-	-	3.366	3.366	5.842	
Orthorhombic	6.82	5.91	5.54				[33]
Wurtzite	-	-	-	3.366	3.366	5.842	[34]

The fig. 1.12 presents the theoretical peak positions of X-ray diffractograms for the 3 structures of ZnSnN₂. As shown in this figure, the main diffraction peaks are superposed. for these structures The black ones correspond to the hexagonal structure with lattice parameter $a = 3.41 \text{ \AA}$, $c = 5.11 \text{ \AA}$, In red are the monoclinic structure with lattice parameter $a = 3.39 \text{ \AA}$, $b = 5.54 \text{ \AA}$, $c = 3.36 \text{ \AA}$ and $\beta = 119.136^\circ$, and in blue are the orthorhombic structure with lattice parameter $a = 5.84 \text{ \AA}$, $b = 6.89 \text{ \AA}$ and $c = 5.52 \text{ \AA}$. This figure clearly evidence that is is hard to distinguish the structure of ZnSnN₂ films from X-ray diffraction.

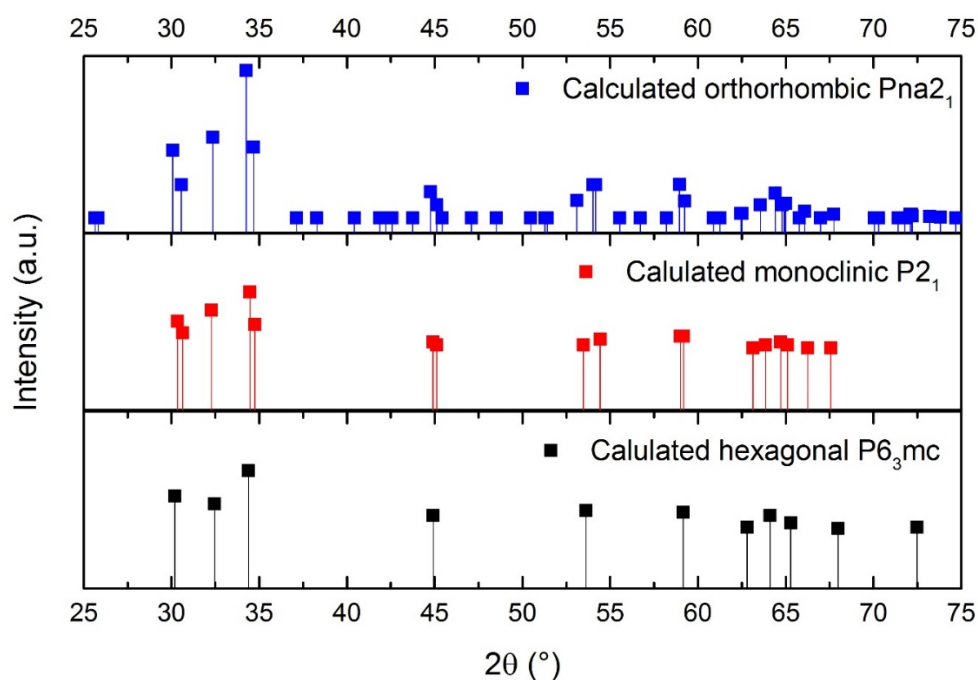


Figure 1.12 Peak positions calculated for 3 different structures. The black ones correspond to the hexagonal structure with lattice parameter $a=0.341$ nm $c=0.511$ nm, the red one correspond to the monoclinic structure with lattice parameter $a=0.339$ nm, $b=0.554$ nm, $c=0.336$ nm and $\beta=119.136^\circ$, and the blue one are related to the orthorhombic structure with lattice parameter $a=0.584$ nm, $b=0.689$ nm and $c=0.552$ nm.

The figure 1.13 shows the electron diffraction pattern simulation of three structures that can be encountered for ZnSnN₂. As for the XRD, the electron diffraction does not seem to be the more powerful method to distinguish the 3 main structures previously described for ZnSnN₂ in the literature.

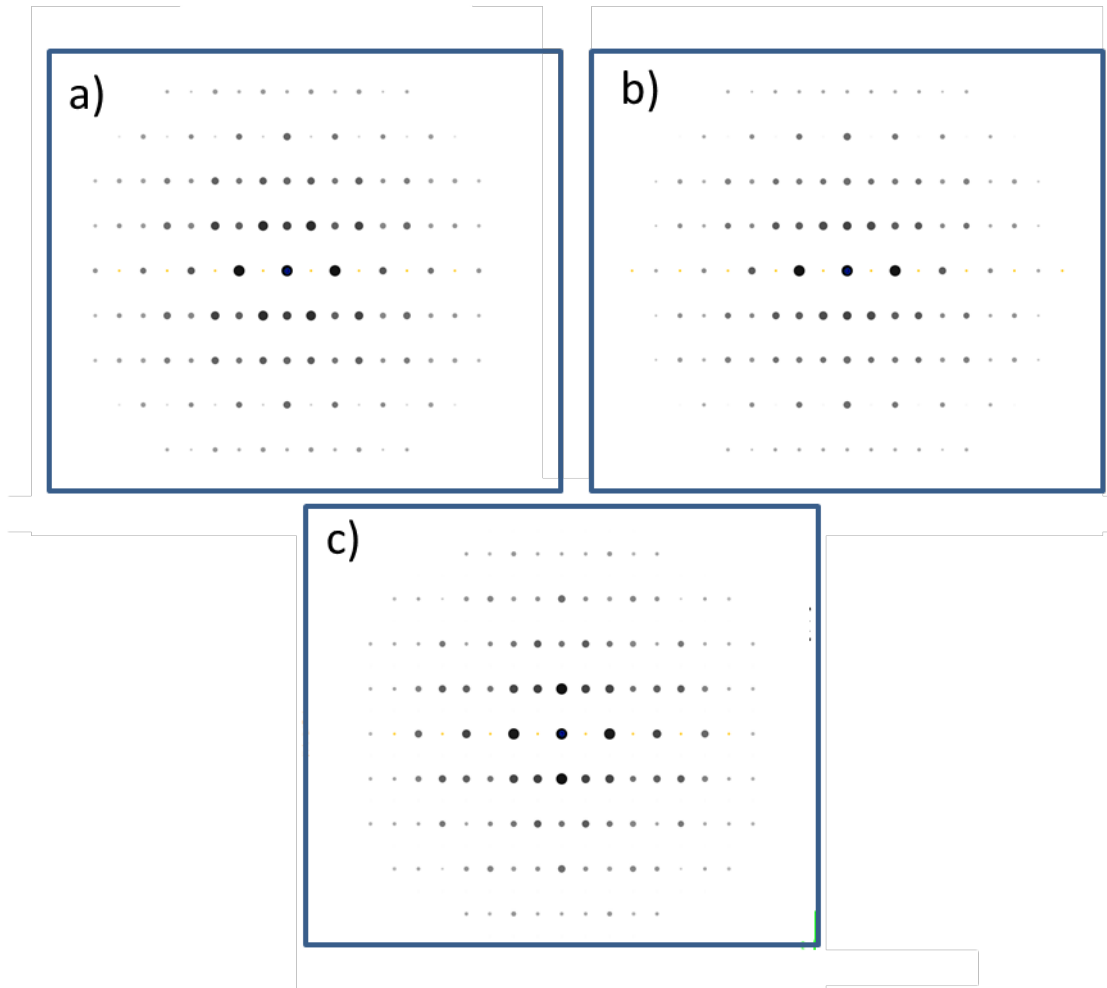


Figure 1.13 Theoretical electron pattern for 3 different structures, (a) Electron diffraction pattern simulation for monoclinic structure $P2_1$ in zone axis $[001]$, (b) Electron diffraction pattern simulation for hexagonal structure $P6_3mc$ in zone axis $[010]$, (c) Electron diffraction pattern simulation for orthorhombic structure $Pna2_1$ in zone axis $[010]$.

The question of the crystallographic structure is so still in debate and the question remains open.

1.2.3 The issue of the electronic structure, defects and band gap

$ZnSnN_2$ is a n-type semiconductor which has a theoretical direct band gap ranging between 1 and 2 eV depending on the cation disorder [21] [23]. As already mentioned in the crystal structure in section 1.2.2, there are two main expectations for the structure of $ZnSnN_2$. The orthorhombic structure has a fully-cation-ordered while the wurtzite structure has a fully-disordered-cation sublattice.

By using DFT calculations, N. Feldberg *et al* [23] have shown that for the perfectly ordered orthorhombic lattice at zero Kelvin the band gap of $ZnSnN_2$ is 2.09 eV, while the

calculated band gap of the disordered monoclinic one is 1.12 eV. T. D. Veal *et al* [26] experimentally confirmed this behavior by growing ZnSnN₂ with different parameters by MBE with a good control of the cation ordering in the film. They have obtained a band gap varying in the range 1.33 - 2.38 eV which is an excellent agreement with the DFT results obtained by N. Feldberg *et al* [23]. The shift of the band gap between the calculated and the experimental data could be explained and interpreted as a Burstein–Moss shift due to high carrier concentration in the film (Figure 1.14).

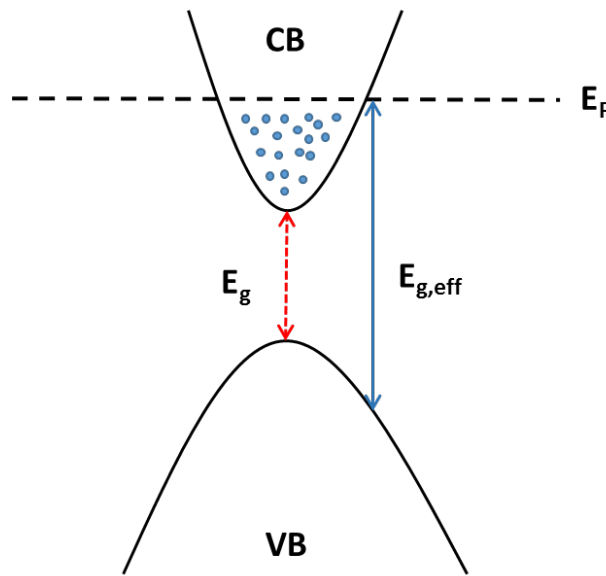


Figure 1.14 Burstein-Moss effect.

L. Lahourcade *et al.* [22] by using DFT method with an hybrid functional HSE (Heyd-Scuseria-Ernzerhof) at zero Kelvin have calculated a direct band gap of 1.42 eV for an orthorhombic structure in the most stable space group Pna2₁. Experimentally, by using spectroscopic ellipsometry, they obtained an optical band gap value near 2.0 eV. Here again, the difference with theoretical results can be attributed to the Burstein-Moss effect due to the high electron carrier concentrations measured by Hall effect. In the table 2 are summarized some data band gap values extracted from previous works of ZnSnN₂.

Table 2. Band gap results of ZnSnN₂ in the previous works

Band gap	Calculation method	Experiment method	Structure	Reference
2.02 eV	QSGW	-	Orthorhombic	[10]
2.0 eV	DFT	-	Orthorhombic	[21]
2.1 eV		Transmittance	Monoclinic	
2.09 eV	DFT	-	Orthorhombic	[23]
1.12 eV	DFT	-	Monoclinic	
2.12-2.38 eV		Transmittance	Orthorhombic	
1.7 eV		Photoluminescence	Orthorhombic	[14]
1.42 eV	DFT hybrid functional	-	Orthorhombic	[22]
2.0 eV		spectroscopic ellipsometry	Orthorhombic	
1.8 eV	QSGW	-	Orthorhombic	[35]
1.9 eV		spectroscopic ellipsometry	Orthorhombic	[24]
1.0 eV		UV-Vis-NIR spectroscopy	Wurtzite	[28]
1.81 eV	QSGW	-	Orthorhombic	[36]
1.4 eV		Transmittance	Ortho/wurtzite	[31]
1.64 eV		-	Wurtzite	[27]
1.75 eV	DFT	-	Orthorhombic	[37]
2.62 eV	PBE0	-	Orthorhombic	[27]

As well, Hall effect measurements has been used for ZnSnN₂ to measure the electron carrier concentrations and the electron mobility. As already mentioned, the Burstein-Moss effect may appear in ZnSnN₂ thin films due to the highest electron carrier concentrations. The values of electron carrier concentrations given in literature vary over a wide range.

The first report of the electron concentration measurements in ZnSnN₂ is given by Lahourcade *et al.* [22] for ZnSnN₂ grown by RF sputtering. They obtained an electron concentration in the $5 \times 10^{19} - 10^{21} \text{ cm}^{-3}$ range. In this work, they mentioned the Burstein-Moss effect due to this large electron concentration. They were also expecting to have a high electron mobility. However, the electron mobility was about $10 \text{ cm}^2 \text{ V}^{-1} \text{ s}^{-1}$, this low mobility has been attributed to the small grain size, which is usual for the materials grown by sputtering.

Other work by Feldberg *et al.* [23] have measured the mobility and the electron concentration of ZnSnN₂. They have been grown the films by molecular beam epitaxy. They obtained a measured mobility about $10 \text{ cm}^2 \text{ V}^{-1} \text{ s}^{-1}$ and the electron concentration is in the

3.0×10^{20} and $1.1 \times 10^{21} \text{ cm}^{-3}$ range. They also mentioned to Burstein-Moss shift phenomenon in the material.

In other cases, ZnSnN_2 have been grown by using DC sputtering by Deng *et al.* [24]. The authors measured the mobility and the electron concentration after annealing the film in a N_2 atmosphere at 300 and 400 °C. They obtained an electron concentration reduction from 1.0×10^{18} to $2.3 \times 10^{17} \text{ cm}^{-3}$ and a mobility decrease from 3.98 to $1.86 \text{ cm}^2 \text{ V}^{-1} \text{ s}^{-1}$ as the annealing temperature increases. As well, Qin *et al.* [27] have grown ZnSnN_2 by DC-sputtering and they measured the electrical propriety after annealing at 200, 300 and 350 °C. They obtained mobilities between 0.37- $2.07 \text{ cm}^2 \text{ V}^{-1} \text{ s}^{-1}$ and electron concentrations between 2.77×10^{17} and $6.78 \times 10^{17} \text{ cm}^{-3}$.

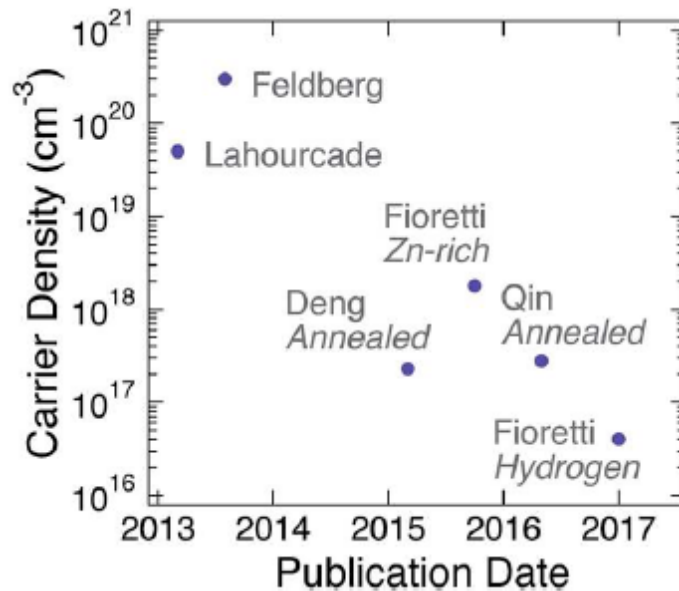


Figure 1.15 Evolution of the carrier densities with years [38].

Finally, Fioretti *et al.* [28] have grown ZnSnN_2 by using RF-sputtering. They measured the mobility and the electronic concentration as a function of the stoichiometry. Mobilities between $1.1 - 8.3 \text{ cm}^2 \text{ V}^{-1} \text{ s}^{-1}$ and carrier densities between $2 \times 10^{18} - 2 \times 10^{20} \text{ cm}^{-3}$ were obtained and the lowest carrier concentration was reached with the off-stoichiometry sample with $0.70 = \text{Zn}/(\text{Zn}+\text{Sn})$. In 2017, Fioretti *et al.* [39] have achieved the lowest value of the carrier concentration for zinc rich ZnSnN_2 thin film by growing this material in forming gas H_2/N_2 and then annealed in atmosphere of nitrogen for 6 h at 300 °C. With this method, they obtained a value $4 \times 10^{16} \text{ cm}^{-3}$ which is the lowest described the literature for ZnSnN_2 ever. On the other

hand, they remarked that the electron mobility decreases from 5-8 to less than $1 \text{ cm}^2 \text{ V}^{-1} \text{ s}^{-1}$ with annealing. They thought the decrease in mobility might be related to an increase in the ionized impurity scattering due to an increase in activated acceptors.

Few groups succeed to growth ZnSnN_2 . As we mention before Feldberg *et al.* [21] was the first growth of ZnSnN_2 where they grow this compound by using plasma-assisted molecular beam epitaxy. Lahourcade *et al.* [22] have grown ZnSnN_2 by RF sputtering. A few years later Veal *et al.* [26] have also grown ZnSnN_2 by using MBE. Quayle *et al.* [14] synthesised this compound by using plasma-assisted vapor liquid solid technique. By using DC sputtering Dang *et al.* [24] have grown ZnSnN_2 thin film. Fioretti *et al.* [28] in 2015 achieved to synthesis ZnSnN_2 by using RF-sputtering. Kawamura *et al.* [31] have synthesised this compound in bulk form via a high-pressure-metathesis reaction. Finally, Kuo *et al.* [24] have succeed to grow this compound in 2017 by using combinatorial approach.

1.3 Conclusion

This first chapter was a bibliographic introduction to the topic of the thesis work. We presented the issues of Earth abundant materials and of scarcity of some elements. Then, we turned to the issue of the energy need and more especially the question of the production of energy, the sun being a real opportunity as it is a free source of energy coming on Earth. The photovoltaic technologies are under development but the different approaches suffer from material or technological problems to be overcome if we want to produce electricity by using a green technology, that is to say with cheap mass production possibilities and without scarce materials.

Then, we described the new material we would like to study: ZnSnN_2 . We showed the main advantages for photovoltaic objectives but we also stressed that a lot of work remains to be done for a good understanding of the material properties and for a good control of the growth process. More especially, we underlined that the crystallographic structure remains not well known in literature.

The aim of this work is then to bring new insight about the growth and the physical of ZnSnN_2 films grown by PVD. It is a topic with a lot development to be done but that may be studied at Institut Jean Lamour as a lot of dedicated facilities are present more especially around material analysis. These facilities will give a chance to bring new element that maybe able answer some unsolved questions during this work.

References

- [1] « Rare Earth Elements—Critical Resources for High Technology | USGS Fact Sheet 087-02 ». [En ligne]. Disponible sur: <https://pubs.usgs.gov/fs/2002/fs087-02/>. [Consulté le: 05-avr-2018].
- [2] « Key World Energy Trends 2016,» tech. rep., International Energy Agency (IEA), 2016 ». .
- [3] « Photovoltaics-Report.pdf ». .
- [4] E. Becquerel, « Mémoire sur les effets électriques produits sous l'influence des rayons solaires », in *Sci. Paris*, vol. 9 (1839) 561, .
- [5] « efficiency-chart.png (1200×665) ». [En ligne]. Disponible sur: <https://www.nrel.gov/pv/assets/images/efficiency-chart.png>. [Consulté le: 12-avr-2018].
- [6] F. Dimroth *et al.*, « Four-junction wafer bonded concentrator solar cells », 2015, p. 1- 1.
- [7] F. Karg, « High Efficiency CIGS Solar Modules », *Energy Procedia*, vol. 15, p. 275- 282, janv. 2012.
- [8] S.-H. Turren-Cruz, A. Hagfeldt, et M. Saliba, « Methylammonium-free, high-performance and stable perovskite solar cells on a planar architecture », *Science*, p. eaat3583, oct. 2018.
- [9] T. R. Paudel et W. R. L. Lambrecht, « First-principles study of phonons and related ground-state properties and spectra in Zn-IV-N₂ compounds », *Phys. Rev. B*, vol. 78, n° 11, p. 115204, sept. 2008.
- [10] A. Punya, W. R. L. Lambrecht, et M. van Schilfgaarde, « Quasiparticle band structure of Zn-IV-N₂ compounds », *Phys. Rev. B*, vol. 84, n° 16, p. 165204, oct. 2011.
- [11] M. Razeghi et M. Henini, « Chapter 1 - Introduction », in *Optoelectronic Devices: III Nitrides*, Oxford: Elsevier, 2005, p. 1- 8.
- [12] M. Razeghi, « Short-wavelength solar-blind detectors-status, prospects, and markets », *Proc. IEEE*, vol. 90, n° 6, p. 1006- 1014, juin 2002.
- [13] G. F. Yang *et al.*, « InGa_N/Ga_N multiple quantum wells on selectively grown Ga_N microfacets and the applications for phosphor-free white light-emitting diodes », *Rev. Phys.*, vol. 1, p. 101- 119, nov. 2016.
- [14] P. C. Quayle, K. He, J. Shan, et K. Kash, « Synthesis, lattice structure, and band gap of ZnSnN₂ », *MRS Commun.*, vol. 3, n° 03, p. 135–138, 2013.

- [15] M. Maunaye et J. Lang, « Preparation et propriétés de ZnGeN₂ », *Mater. Res. Bull.*, vol. 5, n° 9, p. 793- 796, sept. 1970.
- [16] T. Endo, Y. Sato, H. Takizawa, et M. Shimada, « High-pressure synthesis of new compounds, ZnSiN₂ and ZnGeN₂ with distorted wurtzite structure », *J. Mater. Sci. Lett.*, vol. 11, n° 7, p. 424- 426, janv. 1992.
- [17] T. Cloitre, A. Sere, et R. L. Aulombard, « Epitaxial growth of ZnSiN₂ single-crystalline films on sapphire substrates », *Superlattices Microstruct.*, vol. 4- 6, n° 36, p. 377- 383, 2004.
- [18] K. Du, C. Bekele, C. C. Hayman, J. C. Angus, P. Piruz, et K. Kash, « Synthesis and characterization of ZnGeN₂ grown from elemental Zn and Ge sources », *J. Cryst. Growth*, vol. 310, n° 6, p. 1057- 1061, mars 2008.
- [19] « Web of Science Search Box - Clarivate Analytics ». [En ligne]. Disponible sur: <http://wokinfo.com/webtools/searchbox/>. [Consulté le: 11-mars-2018].
- [20] A. M. Shing, N. C. Coronel, N. S. Lewis, et H. A. Atwater, « Semiconducting ZnSn_xGe_{1-x}N₂ alloys prepared by reactive radio-frequency sputtering », *Appl Mater.*, vol. 3, n° 7, p. 076104, juill. 2015.
- [21] N. Feldberg *et al.*, « ZnSnN₂: A new earth-abundant element semiconductor for solar cells », in *2012 38th IEEE Photovoltaic Specialists Conference (PVSC)*, 2012, p. 002524- 002527.
- [22] L. Lahourcade, N. C. Coronel, K. T. Delaney, S. K. Shukla, N. A. Spaldin, et H. A. Atwater, « Structural and Optoelectronic Characterization of RF Sputtered ZnSnN₂ », *Adv. Mater.*, vol. 25, n° 18, p. 2562- 2566, mai 2013.
- [23] N. Feldberg *et al.*, « Growth, disorder, and physical properties of ZnSnN₂ », *Appl. Phys. Lett.*, vol. 103, n° 4, p. 042109, juill. 2013.
- [24] F. Deng *et al.*, « Determination of the basic optical parameters of ZnSnN₂ », *Opt. Lett.*, vol. 40, n° 7, p. 1282- 1285, avr. 2015.
- [25] A. N. Fioretti *et al.*, « Combinatorial insights into doping control and transport properties of zinc tin nitride », *J. Mater. Chem. C*, vol. 3, n° 42, p. 11017- 11028, oct. 2015.
- [26] T. D. Veal *et al.*, « Band Gap Dependence on Cation Disorder in ZnSnN₂ Solar Absorber », *Adv. Energy Mater.*, vol. 5, n° 24, p. n/a-n/a, déc. 2015.
- [27] R. Qin *et al.*, « Semiconducting ZnSnN₂ thin films for Si/ZnSnN₂ p-n junctions », *Appl. Phys. Lett.*, vol. 108, n° 14, p. 142104, avr. 2016.
- [28] A. N. Fioretti *et al.*, « Combinatorial insights into doping control and transport properties of zinc tin nitride », *J. Mater. Chem. C*, vol. 3, n° 42, p. 11017- 11028, oct. 2015.

- [29] A. N. Fioretti, E. S. Toberer, A. Zakutayev, et A. C. Tamboli, « Effects of low temperature annealing on the transport properties of zinc tin nitride », in *2015 IEEE 42nd Photovoltaic Specialist Conference (PVSC)*, 2015, p. 1- 5.
- [30] N. Senabulya *et al.*, « Stabilization of orthorhombic phase in single-crystal ZnSnN₂ films », *AIP Adv.*, vol. 6, n° 7, p. 075019, juill. 2016.
- [31] F. Kawamura, N. Yamada, M. Imai, et T. Taniguchi, « Synthesis of ZnSnN₂ crystals via a high-pressure metathesis reaction », *Cryst. Res. Technol.*, vol. 51, n° 3, p. 220- 224, mars 2016.
- [32] R. A. Makin *et al.*, « Growth of ordered and disordered ZnSnN₂ », *J. Vac. Sci. Technol. B*, vol. 35, n° 2, p. 02B116, mars 2017.
- [33] D. Q. Fang, X. Chen, P. F. Gao, Y. Zhang, et S. L. Zhang, « Mono- and Bilayer ZnSnN₂ Sheets for Visible-Light Photocatalysis: First-Principles Predictions », *J. Phys. Chem. C*, vol. 121, n° 46, p. 26063- 26068, nov. 2017.
- [34] X. Cao, F. Kawamura, Y. Ninomiya, T. Taniguchi, et N. Yamada, « Conduction-band effective mass and bandgap of ZnSnN₂ earth-abundant solar absorber », *Sci. Rep.*, vol. 7, n° 1, p. 14987, nov. 2017.
- [35] A. Punya et W. R. L. Lambrecht, « Band offsets between ZnGeN₂, GaN, ZnO, and ZnSnN₂ and their potential impact for solar cells », *Phys. Rev. B*, vol. 88, n° 7, p. 075302, août 2013.
- [36] P. C. Quayle *et al.*, « Charge-neutral disorder and polytypes in heterovalent wurtzite-based ternary semiconductors: The importance of the octet rule », *Phys. Rev. B*, vol. 91, n° 20, p. 205207, mai 2015.
- [37] T. Wang, C. Ni, et A. Janotti, « Band alignment and p-type doping of ZnSnN₂ », *Phys. Rev. B*, vol. 95, n° 20, p. 205205, mai 2017.
- [38] A. D. Martinez, A. N. Fioretti, E. S. Toberer, et A. C. Tamboli, « Synthesis, structure, and optoelectronic properties of II–IV–V₂ materials », *J. Mater. Chem. A*, vol. 5, n° 23, p. 11418- 11435, juin 2017.
- [39] A. N. Fioretti *et al.*, « Effects of Hydrogen on Acceptor Activation in Ternary Nitride Semiconductors », *Adv. Electron. Mater.*, vol. 3, n° 3, p. n/a-n/a, mars 2017.

Chapter 2. Synthesis of zinc tin nitride thin films and characterization methods

	31
2.1 Introduction.....	31
2.2 Zinc tin nitride thin film growth	31
2.3 Structure zone diagram (SZD)	33
2.4 Elaboration setup.....	34
2.5 X-ray diffraction (XRD).....	35
2.6 X-ray energy dispersive spectroscopy (EDS) and scanning electron microscopy (SEM)	37
2.7 Conversion electron Mossbauer spectroscopy	38
2.8 Transmission Electron Microscopy (TEM).....	40
2.9 Four points probe method.....	41
2.10 Hall effect measurements	42
2.11 UV-visible spectroscopy.....	43
2.12 Ellipsometry.....	46
2.13 X-ray photoelectron spectroscopy (XPS).....	47
2.14 Conclusion	48
References.....	49

Chapter 2. Synthesis of zinc tin nitride thin films and characterization methods

2.1 Introduction

In this chapter, we describe the main techniques used during this work. The ZnSnN₂ thin films have been grown by reactive magnetron co-sputtering. The structure of the films has been studied by X-ray diffraction and their microstructure has been studied by transmission electron microscopy (TEM) and scanning electron microscopy (SEM). The oxidation states for the tin element have been studied using conversion electron Mossbauer spectroscopy and X-ray photoemission spectroscopy. The optical properties have been studied by UV-visible and by ellipsometry spectroscopies. The electrical properties have been determined using the four-point probe method and Hall effect measurements.

2.2 Zinc tin nitride thin film growth

Among the various physical vapor deposition processes, the reactive magnetron sputtering one can be used to grow oxides, nitrides, carbides, ... using a metallic target and a mixture of inert (usually Ar) and reactive (oxygen, nitrogen, methane, ...) gases [1]–[3]. In this work, zinc tin nitride thin films have been elaborated by reactive magnetron co-sputtering, the use of two targets is very powerful to control the film stoichiometry compared to the use of an alloyed target. In general, magnetron sputtering process can be described as the interaction between a target and ions produced in a cold plasma. Figure 2.1 shows a schematic view of the magnetron sputtering process. The sputtered atoms are transferred into the gas phase and condensate at the substrate surface to form the film. In our work, nitrogen (N₂) was used as a reactive gas to grow ZnSnN₂ on silicon or glass substrates.

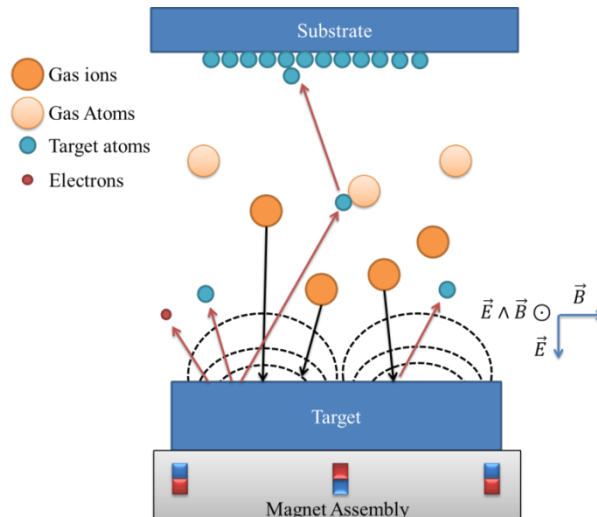


Figure 2.1 Schematic of magnetron sputtering deposition.

The sputtering process is based on the use of a metallic target that acts as the source for the element constituting the growing film. A plasma is created close to the target by applying either a radiofrequency bias or a DC one. The ions (Ar^+ , N_2^+) formed into the plasma are accelerated due to this voltage and bombard the target surface. After momentum transfer to the target atoms, some of them can be sputtered depending on the sputtering yield of the considered element. Since the 70's or the 80's, the use of concentric magnets on the target back side allows to increase the deposition rate of the films due to the so-called magnetron effect. Magnetron sputtering allows the deposition of thin films at low total pressure, i.e. few tenths of Pa, that present higher density than films previously deposited using the diode sputtering process. In the magnetron sputtering system the target can be considered as the cathode and the substrate as the anode. There are several important parameters, which have great effects on film properties in reactive magnetron sputtering processes:

- The reactive gas partial pressure,
- The total pressure,
- The electric parameters applied to the target,
- The substrate temperature,
- The distance between the target and the substrates.

These parameters are able to change the physical and chemical properties of the films.

2.3 Structure zone diagram (SZD)

A structure zone diagram (SZD) is a helpful tool to describe the expected microstructure of the films as a function of the deposition parameters: pressure, temperature, energy... In 1974, Thornton [4] applied the structure zone model for the description of thin film morphologies obtained with sputtering process, Anders [5] improved this diagram by taking into account the energy for the films deposited by HIPIMS (fig. 2.2).

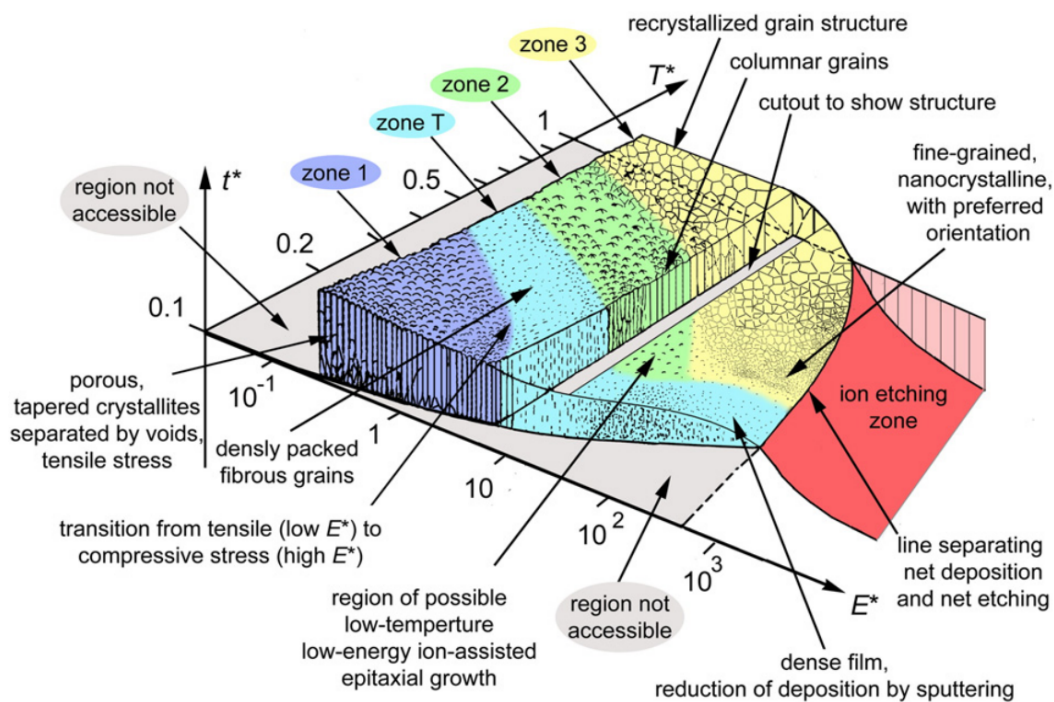


Figure 2.2 Structure zone diagram by A. Anders [5], where E^* is the normalized kinetic energy, T^* is the generalized temperature and t^* is represents the net thickness of the film.

Magnetron sputtering is based on the exchange of kinetic energy between the ions and the metallic target. One of the advantage of sputtering is that it could lead to metastable phases by changing this kinetic energy or, in general, by changing the thermodynamic condition (pressure, temperature, mean free path), as well as this parameter can change the microstructure as shown in (fig.2.2). The table 2.1 describes each zone.

Table 2.1 Brief description of each zone diagram (SZD)

Zone 1	Columns separated and porous morphology
Zone T	Dense array of fibrous grains morphology
Zone 2	Dense columnar grains morphology
Zone 3	Dense morphology with an equiaxed structure

2.4 Elaboration setup

Zinc tin nitride thin films were elaborated by using two metallic targets of zinc and tin. The diameter of the targets was 50 mm and their thickness was 3 mm. The experimental sputtering device was a 30 L sputtering chamber equipped with a rotating substrate-holder parallel to the target. The fig. 2.3 shows a schematic view of the deposition chamber. A base vacuum of approx. 10^{-4} Pa was ensured by a primary and a secondary pumps. Although we have tested the use of a reactive Ar- N_2 mixture to deposit zinc tin nitride films, most of the $ZnSnN_2$ films presented in this manuscript were grown using a pure nitrogen as gas phase. The flow rates were controlled using mass flow controllers. The nitrogen flow rate in this work was varied between 30 standard cubic centimeters per minute (sccm) and 90 sccm. In addition, the total pressure was controlled using a throttle valve.

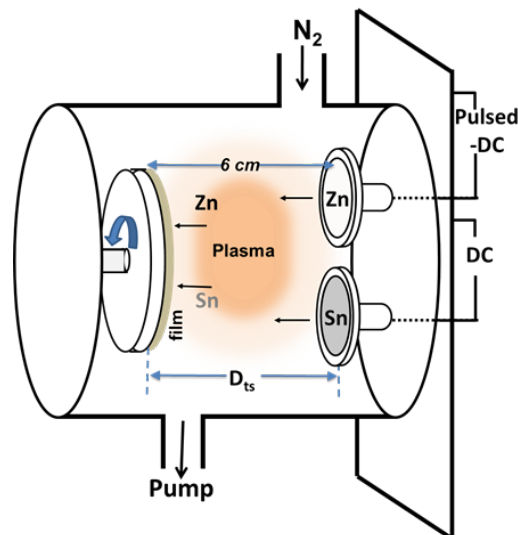


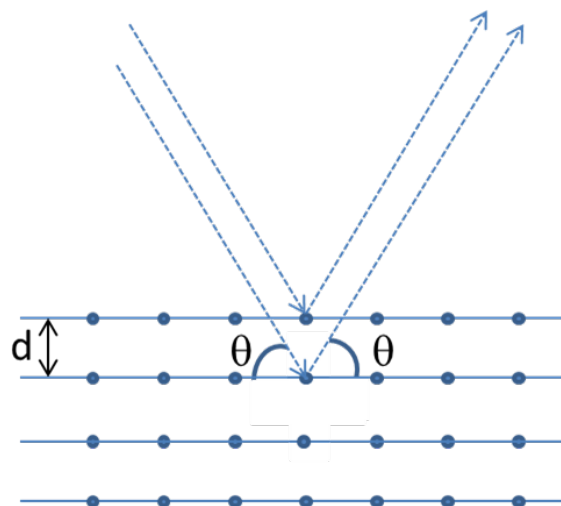
Figure 2.3 Schematic view of the reactive sputtering chamber used for the growth of zinc tin nitride thin films.

The distance between the substrates (glass or silicon) and the targets was 60 mm. Thin films were deposited at different total pressures from 0.5 to 3 Pa. A pulsed-DC supply was used to sputter the zinc target, the frequency of 100 kHz and 2 μ s off time were fixed, while the tin target was sputter using a DC supply. During the deposition, no intentional heating was applied to the substrates and the substrate temperature was close to 50 °C.

2.5 X-ray diffraction (XRD)

The X-ray diffraction is one of the most important methods to characterize the structure of thin films. Information of crystalline materials correspond to the phase nature, the lattice constant, their preferred orientation or texture. This method can also be used to get information on the grain size (apparent coherence length), stress, ... This method which is widely used in the material science community is of primary importance to get information about the nature of as-deposited thin films.

X-rays are electromagnetic waves with wavelength corresponding to the distances between the atoms constituting the analyzed materials. When propagating through a crystal, the X-ray radiations interact with ordered atoms (lattice) and are diffracted due to Bragg law (fig.2.4).



$$2d_{hkl} \sin \theta = n\lambda \quad (2.1)$$

Figure 2.4 Schematic representation of the Bragg diffraction law and Bragg equation.

Here, d is the distance between diffracting planes, the indices h , k , and l are called Miller indices that represent the specific crystallographic planes. In the equation, θ is the diffraction angle, λ is the wavelength and n is a positive integer.

In X-ray diffraction method, it is possible to obtain different information about the material depending on the geometrical configuration used. In this work, the measurements were done using two diffractometers. The first one corresponds to Brucker D8 Advance with Cu $K_{\alpha 1}$ wavelength ($\lambda=0.15406$ nm) in Bragg-Brentano geometry configuration (fig. 2.5). In this geometry, the sample is fixed and the X-ray source and the detector are rotated around the sample with an angle θ and 2θ respectively.

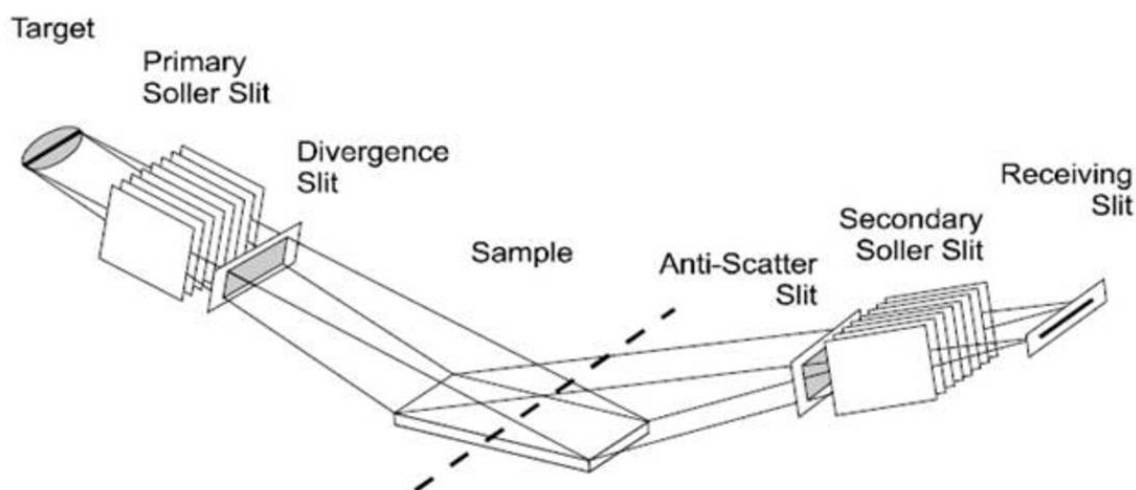


Figure 2.5 Bragg-Brentano geometry.

In the Bragg-Brentano ($\theta/2\theta$) configuration, due to the Bragg diffraction law $2d\sin\theta = n\lambda$, only crystallographic planes in condition of diffraction and parallel to the sample surface are probed. The detector measures the intensity of the diffracted beam as a function of angle, and we obtain a diffractogram (the evolution of the intensity (number of counts) as a function of angle). JCPDS database and EVA software provided by Brucker were used for the structure determination.

2.6 X-ray energy dispersive spectroscopy (EDS) and scanning electron microscopy (SEM)

Energy dispersive spectroscopy of X-rays (EDS) is a method for chemical measurements that is usually encountered on scanning electron microscopy (SEM). However, such method is also present on a transmission electronic microscope. EDS method allows qualitative and semi-quantitative chemical analysis. In SEM (fig. 2.6) an electron gun is the source of the electron beam that impacts the surface sample generating different types of interactions. Secondary electron emission intensity is related with the surface morphology and this information is used to produce images.

The chemical composition of as-deposited ZnSnN_2 thin films has been estimated using the EDS method. Since we do not use calibrated samples and since the EDS method is not accurate to estimate the nitrogen concentration, only the atomic ratio Zn/Sn was determined using EDS. Our EDS equipment was coupled with a scanning electron microscope (SEM): Philips XL30-S. This analysis technique is based on the interaction between the atoms of the film and an accelerated electron beam scanning the surface. Different types of interactions can occur, and lead to different material responses (Fig. 2.6) :

- Emission of secondary electrons
- Emission of backscattered electrons
- X-ray emission

After acceleration of the incident electrons, their interaction with the atoms of the film leads a transfer of energy, slowing down the incident electrons and ejecting an electron from an atom of the film when the incident energy is sufficient. This mechanism leads to the emission of an electron, called secondary electron. Its energy depends largely on the angle between the incident beam and the surface. As a result, the secondary electrons, if they are collected during the sweeping the sample, will create characteristic images of the topography of the surface (observation in SE mode: secondary electrons). Following the beam bombardment, some electrons can interact almost elastically with the elements of the film. Then, they are re-emitted in a direction similar to the direction of incidence, but with different energy depending on the element involved. These "backscattered" electrons therefore largely depend on the weight of

the elements, and allow to create images with contrasts between phases rich in heavy elements and those containing lighter elements (observation in BSE mode: back scattered electrons)

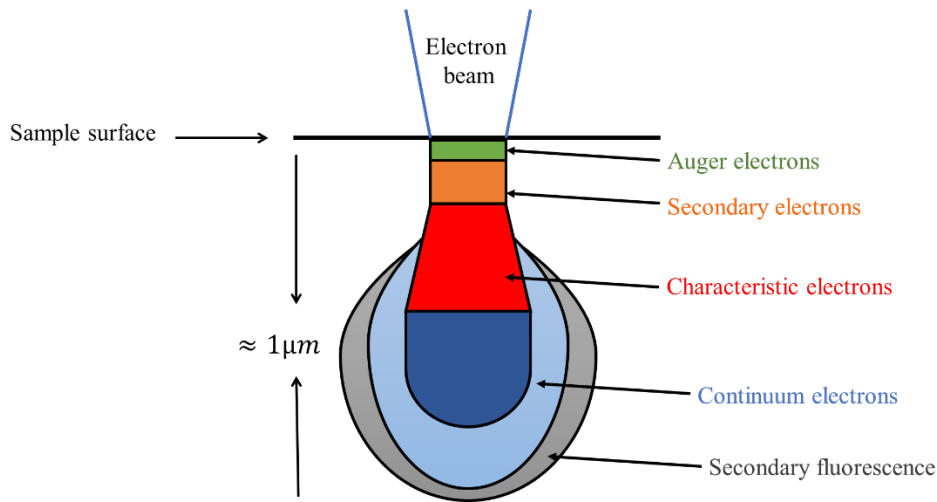


Figure 2.6 Representation of electron interaction with a sample during SEM characterization.

However, in EDS, it is necessary to have an electron beam with an energy high enough to excite inner core electrons from a specific element. The ejection of an electron leaves an empty level. Afterwards, a relaxation process occurs and electrons from upper levels fill the empty level, generating X-ray emission lines corresponding to specific transitions between electronic levels with a cross section depending on the electron incident energy. Each element leads to a unique emission spectrum related with K, L, M or N electronic levels.

In this work related to ZnSnN_2 films, EDS was used to evaluate the atomic ratio ($\frac{\text{Zn}}{\text{Zn}+\text{Sn}}$) between the Zn and Sn atomic concentrations by neglecting contributions from N and Si (substrate) elements.

2.7 Conversion electron Mössbauer spectroscopy

Mössbauer spectroscopy is based on the use of nuclear radiation for chemical characterizations. This spectroscopic method brings information about the chemical environment of the atoms which have a radioactive isotope active in Mössbauer, mainly iron and tin. Mossbauer effect is the recoilless emission and the recoilless resonant absorption of γ photons by the nucleus [6], [7].

The nuclear energy levels of the nucleus depend of the electric and magnetic fields created by its environment (fig 2.7). These so-called hyperfine interactions are of the order of 10^{-7} to 10^{-8} eV and are observable by Mössbauer spectrometry and describe thanks to the following hyperfine parameters:

- The isomeric displacement or chemical shift (δ in mm / s) which reflects the oxidation state of the atom, its nuclear spin state, its coordination, its chemical bond and the nature of the surrounding ligands
- The quadrupole splitting (Δ in mm / s), which reflects the asymmetry of the surrounding charges
- The hyperfine field (B_{hyp} in T) that results from the interaction of the magnetic moment of the nucleus with its magnetic environment

Due to the nuclear hyperfine interaction in Mössbauer spectroscopy appears an isomer shift, the magnetic dipole interaction, and the electric quadrupole interaction (fig. 2.8).

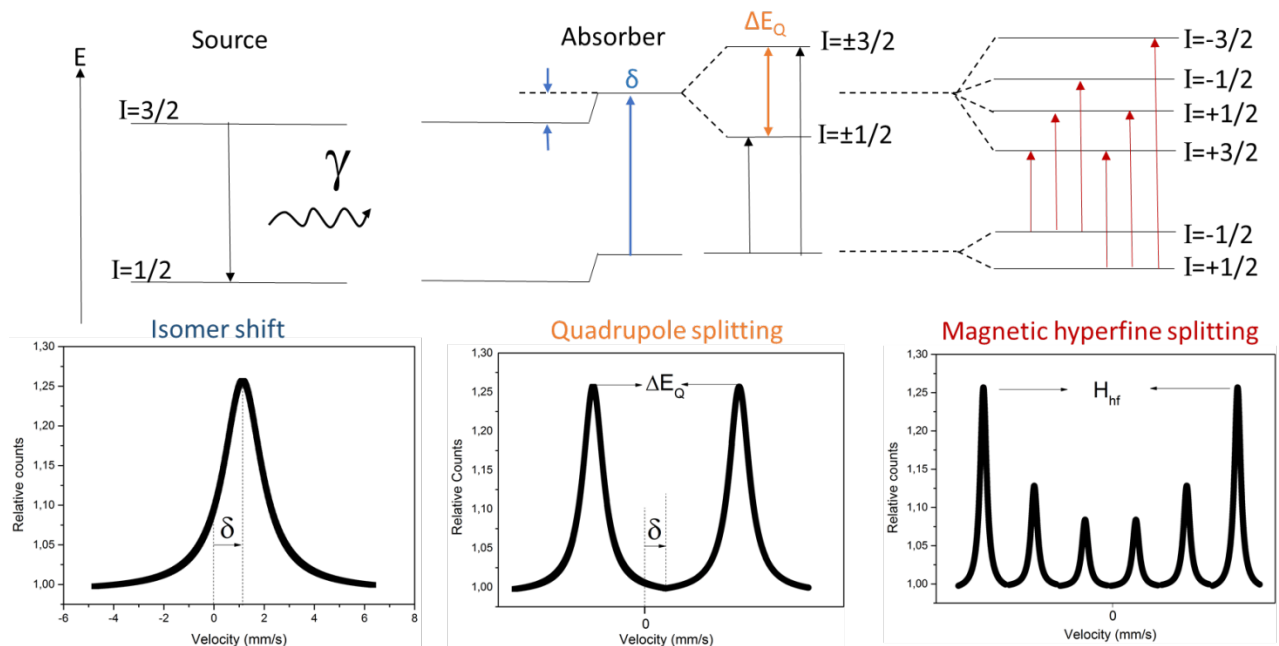


Figure 2.7 Mössbauer shift and splitting of nuclear spin 3/2 and 1/2 by the hyperfine interaction and expected Mössbauer spectra. Where δ shift is the sum of isomer shift and Doppler shift, ΔE_Q are the Electric quadrupole splitting, and H_{hf} are the magnetic hyperfine splitting that is a nuclear Zeeman splitting.

In this work, ^{119}Sn conversion electron Mössbauer spectrometry (CEMS) spectra were recorded by a conventional Mössbauer spectrometer (Wissel) with a flowing gas (96% He, 4% CH_4) proportional counter (Rikon-5) at room temperature. The velocity scale was calibrated with a $^{57}\text{CoRh}$ source and a metallic iron foil. The evaluation of Mössbauer spectra was performed by least square fitting of lines using the Winnormos (Wissel) program. The error on all of the ^{119}Sn Mössbauer spectra was $\pm 0.1\text{mm s}^{-1}$.

2.8 Transmission electron microscopy (TEM).

Transmission electron microscopy is the most powerful technique to study the microstructure of thin films. The TEM setup can build a 2D image by using a beam of accelerated electrons passing through an ultra-thin sample (less than 100 nm thick) and interacting with it. Different interactions between the incident electron beam and the sample can be observed (fig. 2.8).

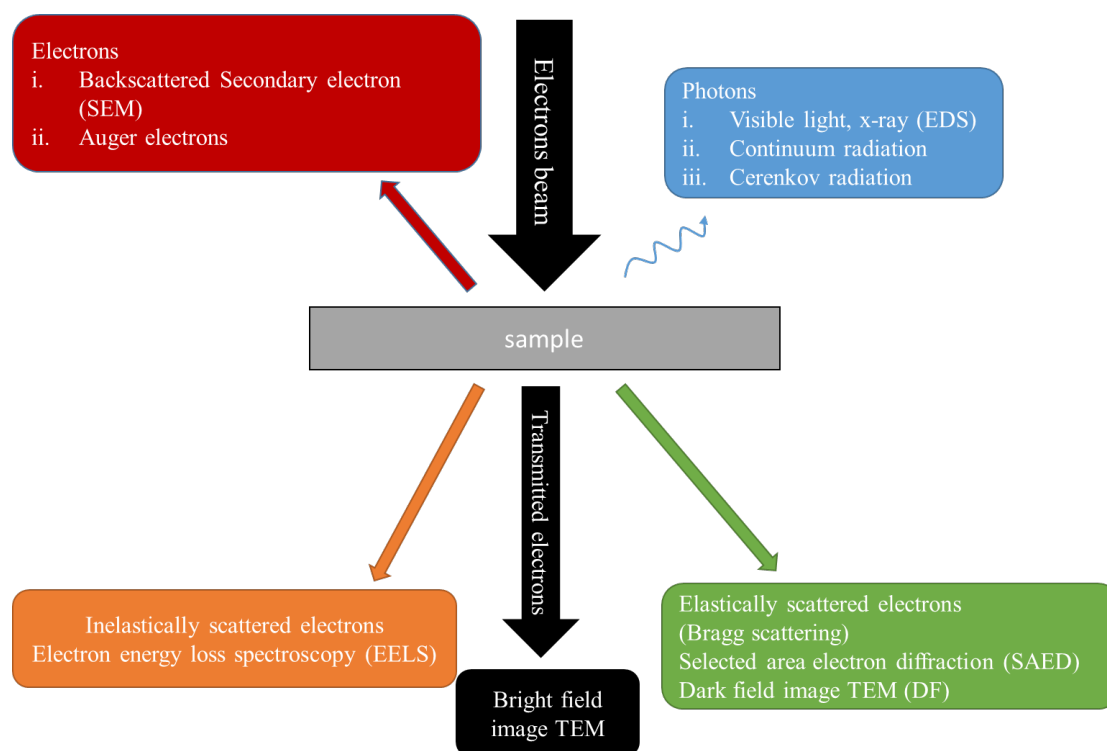


Figure 2.8 Schematic representation of interactions and signals in TEM.

In this work, TEM characterization for the microstructure was performed by a JEOL - ARM 200F Cold FEG TEM/STEM (point resolution 0.19 nm in TEM mode and 0.078 nm in STEM mode) fitted with a GIF Quantum ER. The cross section of the sample was prepared by using a Focused Ion Beam (FIB) apparatus (fig 2.9). This scanning electron microscope with focused ion beam (Helios Nanolab 600i) allows the machining of very thin slides taken from the samples. The MEB-FIB is equipped with two guns: an electron gun and a gallium ion gun (Ga^+). The electron source is used to image the surface of the sample according to the same principle as a conventional scanning electron microscope. The second gun emits a beam of Ga^+ ions that tear the atoms of the sample for thinning.

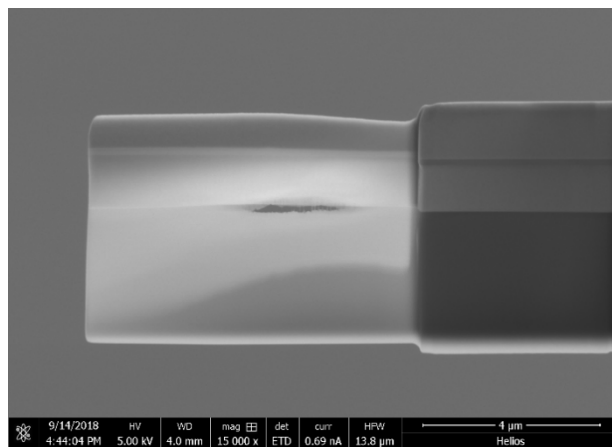


Figure 2.9 ZnSnN₂ lamella elaborated by FIB for TEM measurements.

2.9 Four-point probe method

The four-point probe method was used to determine the electrical resistivity of zinc tin nitride thin films. It is a simple device for measuring the resistivity of semiconductor and metallic samples. The principle is based on the electric contact between the surface of the sample and four metallic probes. By passing a current through two outer probes and measuring the voltage through the inner probes the sheet resistance can be measured (fig. 2.10)

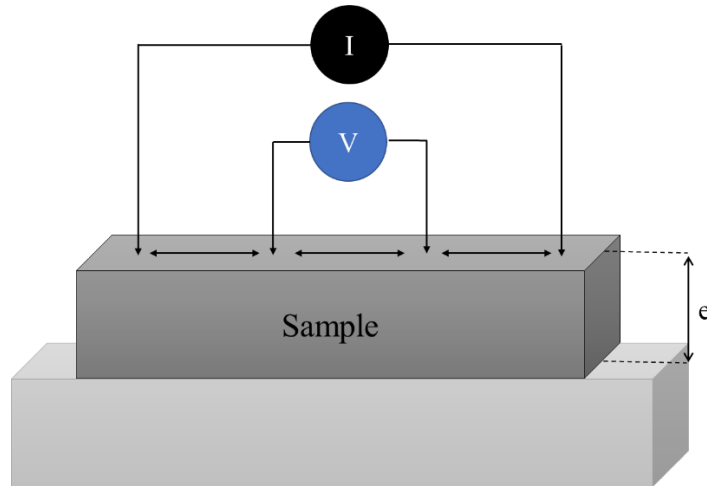


Figure 2.7 Schematic of the four-point probe method for resistivity measurement.

For a thin film deposited on an insulating substrate, the measurement gives access to the ratio $\frac{|\Delta V|}{I}$ related to the resistivity (ρ in $\Omega\cdot\text{cm}$) of materials according to the equation:

$$\rho = \frac{\pi}{\ln 2} e \frac{V}{I} \quad (2.2)$$

Where e is the thickness of the film, V is the voltage measured between the two inner probes and I is the current applied between the two outer probes.

2.10 Hall effect measurements

Hall effect measurements in semiconducting materials can be used to determine accurately conductive type (p or n type), carrier density, electrical resistivity, and the mobility of carriers.

When an electrical current passes through a semiconductor along the x (longitudinal) direction in the presence of a perpendicular magnetic field B along z direction, this induces an electric field E_y along the transverse y direction. The schematic geometry is shown in (fig. 2.11), where the charge accumulation is due to the Lorentz force. The related transverse voltage is called the Hall voltage (V_H), as shown in equation:

$$V_H = -\frac{I \cdot B}{n \cdot t \cdot e} \quad (2.3)$$

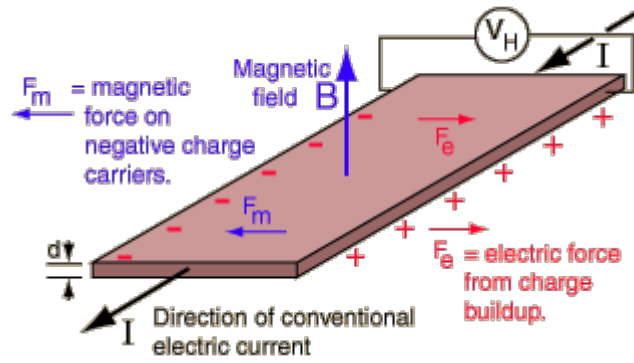


Figure 2.8 Scheme of the Hall effect measurement.

Where I is the current across the plate length B in the magnetic field, t is the thickness of the plate, e is the elementary charge and n is the charge carrier density of the carrier electrons. In this thesis, the carrier density and the mobility were deduced from Hall measurements in the van der Pauw geometry (Ecopia, HMS-5000).

2.11 UV-visible spectroscopy

To determine the optical properties of the films, different spectroscopy techniques have been used. UV-visible spectroscopy allows the determination of the optical band gap. Soda-lime glass substrate was used for its good transparency (transmittance $\approx 90\%$) in the visible and in the near infrared range as shown in (fig.2.12).

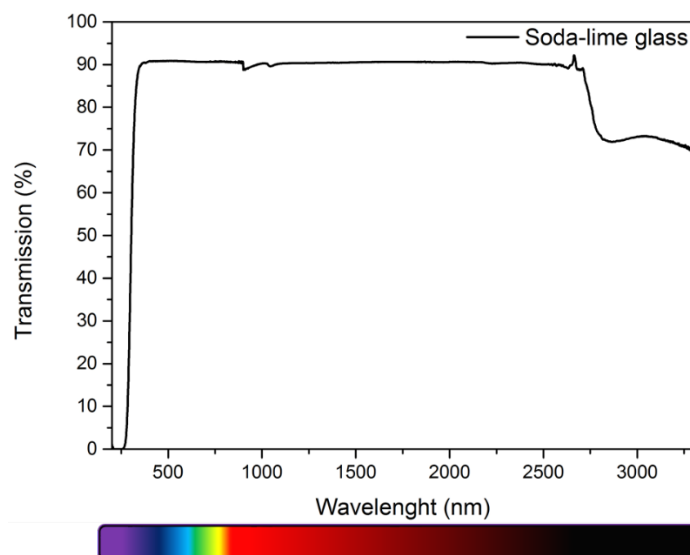


Figure 2.9 Transmission spectrum of the glass substrate.

A Varian Cary 5000 UV-Vis-NIR apparatus was used to determine the optical transmittance measurement. This apparatus works with a double beam and the wavelength can be varied in the range of 200 to 3300 nm. A schematic view of the spectrophotometer is represented in fig. 2.13. A UV-visible light beam is sent to a monochromator and passing with different mirrors. Then, the beam passes through a beam splitter to split the original beam in two beams. One beam passes through a reference compartment while the other is directed to the sample compartment. The two beams are then recovered and are focused onto the detector.

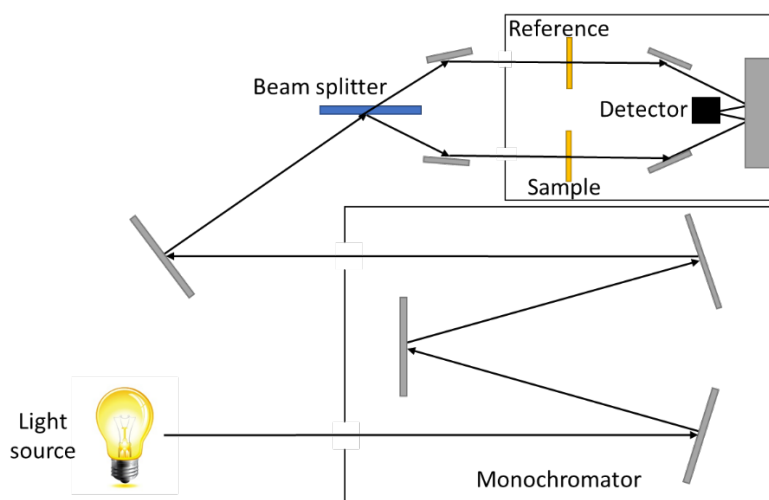


Figure 2.10 Scheme of a double beam absorption spectrometer.

To determine the optical bandgap, the Tauc plot method was used. Optical absorption appears by transition of electrons and holes between electronic states due to the excitation of photons. Each material has an absorption coefficient α corresponding the amount of radiation absorbed by a material at a specific wavelength. We can obtain α from the Beer-Lambert law, which can be written as:

$$T = \frac{I}{I_0} = e^{-\alpha l} \quad (2.4)$$

Where I_0 is the initial intensity of the light and I the intensity of the light after passing through a layer with thickness l . T_{film} is the transmittance of the material, and then it is possible to calculated α from the equation:

$$\alpha = \frac{1}{l} \ln \frac{1}{T_{film}} \quad (2.5)$$

The absorption coefficient in semiconductors is related to the optical band gap (E_g) from the following equation

$$(h\nu\alpha) = B(h\nu - E_g)^n \quad (2.6)$$

Where the value of the exponent n denotes the nature of the transition. In the case of ZnSnN₂, $n = \frac{1}{2}$ as for semiconductors with direct allowed transition[8]–[12]. In addition, B is a constant called the bad tailing parameter. By plotting of $(\alpha h\nu)^2$ versus the photon energy ($h\nu$) gives a straight line in a certain region. The extrapolation of this straight line intercepts the x -axis to give the value of the optical energy gap (E_g).

In semiconductor materials with low crystallinity or in amorphous phases appear the so-called Urbach tail (Urbach energy E_U) [13] because these materials have localized states which extended in optical band gap. Urbach tail manifests as an exponential part along the absorption coefficient curve and near the optical band edge. The absorption coefficient at the photon energy below the optical gap depends exponentially on the photon energy, which is given by the following equation:

$$\alpha = \alpha_0 e^{\left(\frac{h\nu}{E_U}\right)} \quad (2.7)$$

Where E_U is called Urbach energy and α_0 is a constant. By taking the logarithm of the last equation, it is will be written as:

$$\ln \alpha = \ln \alpha_0 + \frac{h\nu}{E_U} \quad (2.8)$$

Urbach energy E_U can be obtained from the slope of the straight line of plotting $\ln \alpha$ (y-axis) versus the photon energy ($h\nu$).

2.12 Ellipsometry

Ellipsometry spectroscopy gives information about the optical properties of the materials. However, it is an indirect method that consists of the acquisition of raw data, the proposition of a model, the fitting of the data and finally the extraction of the optical parameters.

When a polarized beam is reflected on a sample, there is a change in the polarization that can be followed by the changes in the parallel and perpendicular components of the electric field of the incident radiation after the interaction with the sample (fig. 2.14). Where the change in the polarization (P) is given by the equation:

$$P = \tan(\Psi)e^{i\Delta} \quad (2.9)$$

Where Ψ is the amplitude ratio and Δ is the phase shift. From the analysis of the change of polarization of beam, ellipsometry can investigate the complex refractive index or dielectric function tensor, which gives access to fundamental physical parameters.

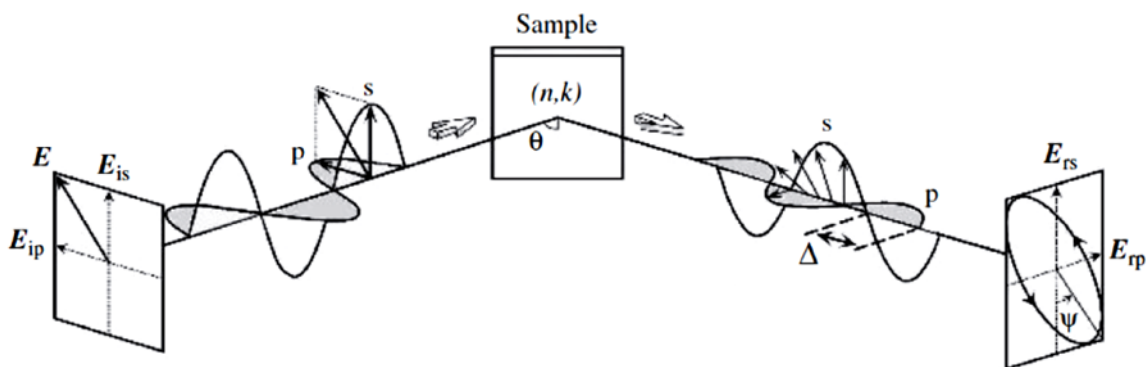


Figure 2.11 Schematic of the experimental configuration used for ellipsometry measurements [14].

In this work, the optical characterization was performed by *ex-situ* spectroscopic ellipsometry (SE) using a Horiba-Jobin Yvon UVISSEL instrument in the spectral range 0.6-6.5 eV (2067-191 nm) at an angle of incidence of 70°. Ellipsometry measurements are performed using a M2000 rotating compensator ellipsometer from Woollam with the films deposited on silicon substrates.

2.13 X-ray photoelectron spectroscopy (XPS)

X-ray photoelectron spectroscopy (XPS) is a technique used for surface analysis to obtain chemical information as elemental composition, chemical state and electronic state of the sample. When X-ray incident photons with energy ($h\nu$) come to eject electrons from an atom, the ejected electrons are emitted with a kinetic energy (E_k). The kinetic energy E_k depends on the energy of the incident photons and is not an intrinsic property of the atom. However, it is possible to relate E_k with the electron binding energy (E_b) (fig. 2.15).

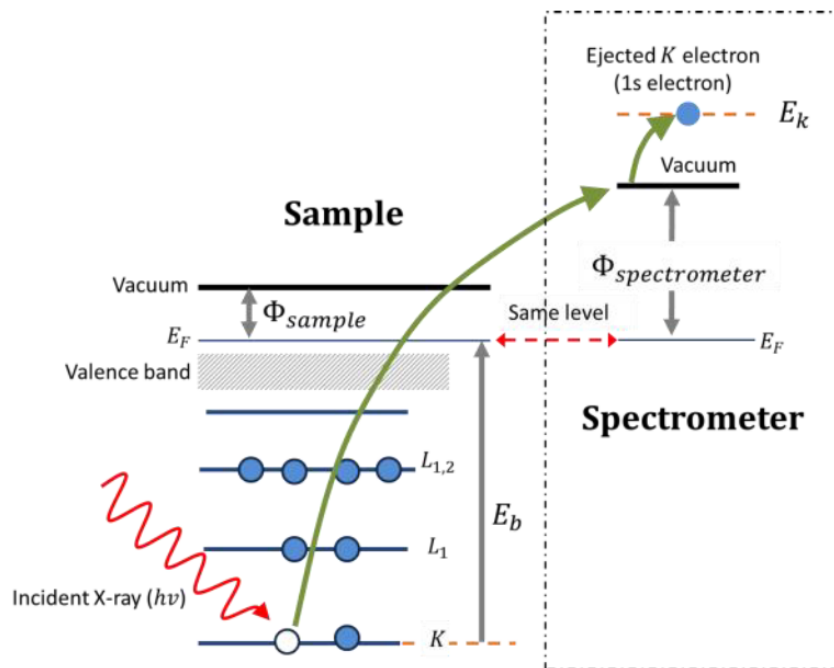


Figure 2.12 Representation of the mechanism of photoelectron emission by a photon with energy $h\nu$ in X-ray photoelectron spectroscopy (XPS) [15].

The electron binding energy gives information about the identity of different atoms as well the specific energy level. E_b is related with the photon incident energy ($h\nu$), E_k and the work function (ϕ_s) of the spectrometer as shown in equation:

$$E_b = h\nu + E_k - \phi_s \quad (2.10)$$

The X-ray photons interact with the material and can eject an electron from atom (A) core levels, producing an ionization process ($A + h\nu \rightarrow A^+ + e^-$). The ejected, and detected, photoelectrons originate from the surface down to a depth of 2-3 nm, making this method surface-sensitive.

In this work, XPS analysis have been performed to recorded N 1s, Sn 3d and Zn 2p and core level spectra, on a K-Alpha Thermo Scientific spectrometer using Al $K\alpha$ radiation (1486.68 eV) with a spot size of 250 μm . Before analysis, the sample surface is cleaned using a mild Ar^+ etching, allowing the removing of the main contaminants. Survey spectra were acquired at a pass energy of 200 eV and high-resolution spectra at 50 eV. The scan number was adjusted (between 10 and 25 scans) to the specific element to get similar signal-to-noise ratios. A flood gun was used for charge compensation and spectra were calibrated by fixing the C 1s main peak at 284.8 eV. Peak-fitting was performed with the Advantage© software (Thermo).

2.14 Conclusion

In this chapter, we have detailed the experimental tool used for the growth of zinc tin nitride thin films synthesized by reactive magnetron co-sputtering. In addition, we have presented the characterizations method that we have used in this work. These methods will be used in next chapters to investigate in details the properties of zinc tin nitride thin film.

References

- [1] W. D. Sproul, D. J. Christie, et D. C. Carter, « Control of reactive sputtering processes », *Thin Solid Films*, vol. 491, n° 1, p. 1- 17, nov. 2005.
- [2] S. Berg et T. Nyberg, « Fundamental understanding and modeling of reactive sputtering processes », *Thin Solid Films*, vol. 476, n° 2, p. 215- 230, avr. 2005.
- [3] I. Safi, « Recent aspects concerning DC reactive magnetron sputtering of thin films: a review », *Surf. Coat. Technol.*, vol. 127, n° 2, p. 203- 218, mai 2000.
- [4] Thornton, J. A., « Magnetron Sputtering: Basic Physics and Application to Cylindrical Magnetrons. », *J Vac Sci Technol*, p. 15, 171–177, 1978.
- [5] A. Anders, « A structure zone diagram including plasma-based deposition and ion etching », *Thin Solid Films*, vol. 518, n° 15, p. 4087- 4090, mai 2010.
- [6] S. Nasu, « General Introduction to Mossbauer Spectroscopy », in *Mossbauer Spectroscopy: Tutorial Book*, Y. Yoshida et G. Langouche, Éd. Berlin, Heidelberg: Springer Berlin Heidelberg, 2013, p. 1- 22.
- [7] Y. Yoshida et G. Langouche, Éd., *Mossbauer Spectroscopy: Tutorial Book*. Berlin Heidelberg: Springer-Verlag, 2013.
- [8] J. Tauc, R. Grigorovici, et A. Vancu, « Optical Properties and Electronic Structure of Amorphous Germanium », *Phys. Status Solidi B*, vol. 15, n° 2, p. 627- 637, janv. 1966.
- [9] D. B. Buchholz, J. Liu, T. J. Marks, M. Zhang, et R. P. H. Chang, « Control and Characterization of the Structural, Electrical, and Optical Properties of Amorphous Zinc–Indium–Tin Oxide Thin Films », *ACS Appl. Mater. Interfaces*, vol. 1, n° 10, p. 2147- 2153, oct. 2009.
- [10] Z. Wang, U. Helmersson, et P.-O. Käll, « Optical properties of anatase TiO₂ thin films prepared by aqueous sol–gel process at low temperature », *Thin Solid Films*, vol. 405, n° 1, p. 50- 54, févr. 2002.
- [11] C. Charitidis, P. Patsalas, et S. Logothetidis, « Optical and mechanical performance of nanostructured cerium oxides for applications in optical devices », *J. Phys. Conf. Ser.*, vol. 10, n° 1, p. 226, 2005.
- [12] N. Pliatsikas, A. Siozios, S. Kassavetis, G. Vourlias, et P. Patsalas, « Optical properties of nanostructured Al-rich Al_{1-x}Ti_xN films », *Surf. Coat. Technol.*, vol. 257, p. 63- 69, oct. 2014.

- [13] F. Urbach, « The Long-Wavelength Edge of Photographic Sensitivity and of the Electronic Absorption of Solids », *Phys. Rev.*, vol. 92, n° 5, p. 1324- 1324, déc. 1953.
- [14] H. Fujiwara, *Spectroscopic Ellipsometry: Principles and Applications*. .
- [15] J. F. Watts et J. Wolstenholme, « An Introduction to Surface Analysis by XPS and AES », *Wiley.com*. [En ligne]. Disponible sur: <https://www.wiley.com/en-us/An+Introduction+to+Surface+Analysis+by+XPS+and+AES-p-9780470847138>.

Chapter 3. ZnSnN₂ Thin Films: Synthesis and characterization.....	53
3.1 First attempt to grow zinc tin nitride thin films by PVD	53
3.1.1 Growth of ZnSnN ₂ by controlling the discharge current	53
3.1.2 Growth of ZnSnN ₂ by fixing the discharge voltage.....	55
3.1.3 Growth of ZnSnN ₂ by controlling the discharge voltage in a pure nitrogen plasma.	57
3.1.4 Effect of the substrate nature	60
3.2 Crystalline ZnSnN₂ thin films structure, microstructure, physical and chemical properties.....	61
3.2.1 Introduction.....	61
3.2.2 Chemical composition	62
3.2.3 Structure of ZnSnN ₂ films	62
3.2.4 Microstructure and morphology of ZnSnN ₂ thin films.....	64
3.2.5 X-ray photoelectron spectroscopy analysis of ZnSnN ₂ thin films.....	68
3.2.6 Mossbauer spectrometry of ZnSnN ₂ thin films.....	70
3.2.7 Electrical and optical properties of ZnSnN ₂	71
3.3 Effect of base pressure before the film growth	76
3.4 Conclusion	82
Reference	84

Chapter 3. ZnSnN₂ Thin Films: Synthesis and characterization

This chapter is divided in three main parts. In a first part, we investigate the growth parameters to deposit in reproducible way ZnSnN₂ thin films by magnetron co-sputtering and we investigate the effect of substrate nature. The second part of this chapter is focused on the structure, the microstructure and the physico-chemical properties of ZnSnN₂ thin film grown via DC magnetron co-sputtering. A special attention is dedicated to the chemical environment of metallic atoms that has been probed by X-ray photoelectron spectroscopy and Mössbauer spectrometry. Electrical and optical properties of our films are also described. Finally, we detail in the third section a study on the effect of the base pressure before the deposition run on the structure, the microstructure and the physico-chemical properties of ZnSnN₂ thin films.

3.1 First attempt to grow zinc tin nitride thin films by PVD

The deposition runs were performed at room temperature in a chamber equipped with two magnetron cathodes. A schematic view of the deposition reactor has been presented in the previous chapter (Figure 2.3). ZnSnN₂ films were grown on glass and silicon (intrinsic, oriented (100), thickness 500-550 μm) substrates by DC or pulsed DC sputtering of metallic tin and zinc targets. The targets were placed off-axis relatively to the substrate holder axis and the rotation enables a good lateral homogeneity in thickness. Prior to the deposition, the substrate surfaces were cleaned using a radiofrequency bias (-200 V, 2 minutes).

At the beginning of each series of deposition runs, the first one was dedicated to coat the chamber walls by a layer of ZnSnN₂. This first layer acts as a passivate film and we have observed that this procedure allows to ensure the elaboration of reproducible zinc tin nitride thin films. To limit the oxygen contamination of the films, the base pressure was systematically lower than 10⁻⁴ Pa.

3.1.1 Growth of ZnSnN₂ by controlling the discharge current

At the beginning of this work, the deposition of ZnSnN₂ thin films has been tested by using gas mixture of Ar and N₂. The argon flow rate has been fixed to 30 sccm and the nitrogen one was varied in the 4-30 sccm range for the 1st and 2nd series of growth (see tables 3.1 and 3.2). The total pressure during growth (or the working pressure) was varied between 0.4 and

2.0 Pa. Since our research group usually controls the target sputtering by fixing the current applied to the target, we have started this series of sample within these conditions. The discharge current was varied between 0.02 and 0.1 A and between 0.1 and 0.15 A for the zinc and tin targets, respectively. The table 3.1 summarizes the experimental parameters of the first four samples representative of zinc tin-based films.

Table 3.1 : First series of experimental parameters for zinc and tin-based thin film elaboration.

Sample	Flow rate (sccm)		Current (A)		Chemical composition (%)		Thickness (μm)	Total pressure (Pa)
	Ar	N ₂	Zn	Sn	Zn	Sn		
ZSN-2	30	4	0.1	0.1	97.7	2.3	5.5	0.43
ZSN-3	30	8	0.1	0.1	98.9	1.1	5.08	0.44
ZSN-4	30	8	0.05	0.1	95.1	4.9	1.66	0.69
ZSN-5	30	30	0.05	0.1	90.6	9.4	0.72	0.67

The EDS measurement results presented in table 3.1 clearly show zinc-rich films. Furthermore, the decrease of the films thickness with the nitrogen flow rate increase suggests that the samples ZSN-2 and ZSN-3 should be metallic materials deposited in the elemental sputtering mode (ESM). The X-ray diffractograms for this series of samples (figure 3.1) show that with a flow rate of N₂ from 4 sccm to 8 sccm, the films correspond to metallic zinc. For a flow rate of N₂ 30 sccm the peaks of metallic zinc disappear and the film is X-ray amorphous.

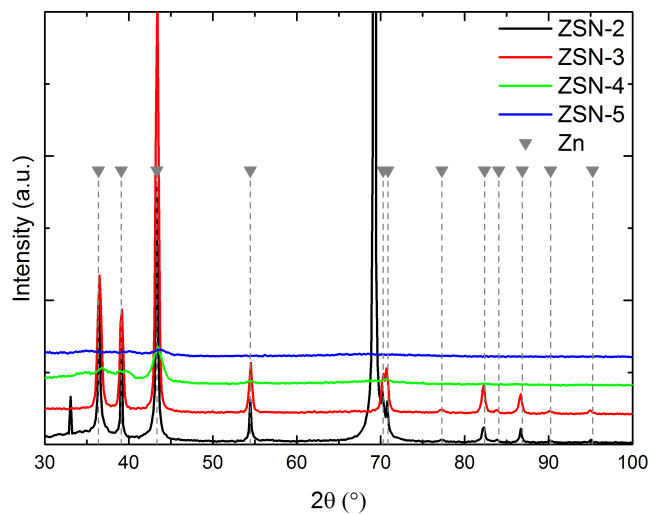


Figure 3.1 X-ray diffractograms of the first series of samples deposited using the parameters listed in table 3.1.

However, the stoichiometry of the films was far from the expected one. By decreasing the discharge current on the zinc target and increasing the tin target one, the expected stoichiometry was obtained for the sample ZSN-9 (table (3.2)). In this work, the reproducibility was one of the main issue we had to face-off for $ZnSnN_2$ elaboration by controlling the discharge current. As shown in the table 3.2 the thickness and the composition were difficult to control. Thus, we have decided to change our process, i.e. the way to control the sputtering of the targets.

Table3.2 : Experimental parameters of the second series of ZSN thin films.

Sample	Flow rate (sccm)		Current (A)		Chemical composition (at. %)		Thickness (μm)	Total pressure (Pa)
	Ar	N ₂	Zn	Sn	Zn	Sn		
ZSN-6	30	30	0.025	0.1	90.42	9.58	0.38	0.68
ZSN-7	30	30	0.015	0.1	64.73	35.27	0.31	0.67
ZSN-8	30	30	0.02	0.1	64.63	35.37	0.18	0.79
ZSN-9	30	30	0.02	0.12	49.99	50.01	0.9	0.80
ZSN-10	30	30	0.02	0.15	26.4	73.6	1.2	0.71
ZSN-11	30	30	0.02	0.1	84.93	15.07	0.04	2.08

3.1.2 Growth of $ZnSnN_2$ by fixing the discharge voltage

Since the control of the target current was not powerful to control the film growth, we have tried to fix the target voltage. Within this method, the energy of the argon ions bombarding the targets was controlled. Compared to the previous method, we were expecting to avoid the heating of the target inducing a possible target evaporation. Indeed, such a behavior may explain the non-reproducibility of the films. Table 3.3 reports the growth parameters used. In this series, the flow rate was fixed at 30 sccm for both Ar and N₂ gases. The discharge voltage was arbitrary fixed to -200 V for the zinc target. Thus, the way to control the film stoichiometry was to vary the voltage applied to the tin target.

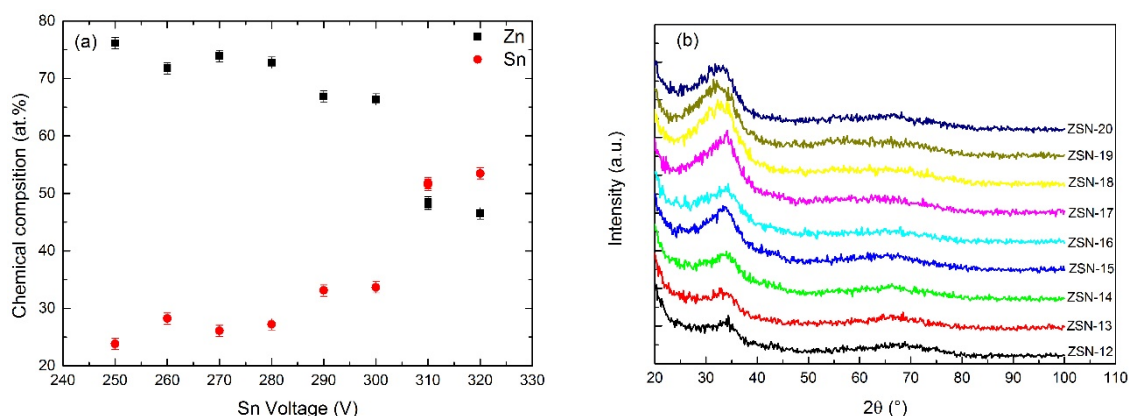


Figure 3.2 (a) Evolution of the chemical composition of ZSN films as a function of the discharge voltage applied to the tin target, (b) XRD of $ZnSnN_2$ with different parameters of elaboration (table 3.3).

As expected, the chemical composition of the films can be controlled by the tin target voltage. When the tin target voltage was fixed to -310 V, the metallic chemical composition was very close to that expected for $ZnSnN_2$. Furthermore, by comparing the samples ZSN-18 and ZSN-20 we show that the reproducibility seems to be reached. Unfortunately, obtaining a stoichiometric film of $ZnSnN_2$ with these parameters of elaboration was not enough to get a crystallized material. Whatever the crystallization level, all the films were X-ray amorphous (figure 3.2 (b)).

Table 3.3 : Experimental parameters for the third series of films.

Sample	Flow rate (sccm)		Voltage (V)		Chemical composition (at. %)		Thickness (μm)	Total pressure (Pa)
	Ar	N_2	Zn	Sn	Zn	Sn		
ZSN-12	30	30	-200	250	76.16	23.83	0.6	1.5
ZSN-13	30	30	-200	-260	71.77	28.25	0.65	1.5
ZSN-14	30	30	-200	-270	73.9	26.1	0.85	1.5
ZSN-15	30	30	-200	-280	72.75	27.23	1.0	1.5
ZSN-16	30	30	-200	-290	66.85	33.14	1.0	1.5
ZSN-17	30	30	-200	-300	66.36	33.64	1.0	1.5
ZSN-18	30	30	-200	-310	48.47	51.53	0.8	1.5
ZSN-19	30	30	-200	-320	46.53	53.47	1.0	1.5
ZSN-20	30	30	-200	-310	48.19	51.81	0.8	1.5

3.1.3 Growth of ZnSnN₂ by controlling the discharge voltage in a pure nitrogen plasma.

In this part, the ZnSnN₂ thin films were grown under pure nitrogen atmosphere, i.e. without the use of Ar. The reason why we decide to use pure plasma of nitrogen was to try to force the formation of the nitride phase and then to overcome the low reactivity of Zn and Sn atoms with nitrogen. This method of elaboration has been used successfully for the growth of nitride thin films. S. Bouhtiyya *et al.* [1] have grown ruthenium nitride thin films by sputtering. For ZnSnN₂, F. Deng *et al.* [2] have prepared ZnSnN₂ thin films by DC magnetron sputtering. Pure nitrogen has been used as sputtering gas. Moreover, other binary phases of zinc nitride and tin nitride have also been grown by sputtering in literature. M. Futsuhara *et al.* [3] showed that pure Zn₃N₂ thin films require the use of a N₂ concentration over 20% in the Ar/N₂ gas mixture. S. Choi *et al.* [4] have grown an amorphous tin nitride thin films by RF sputtering. They have shown that a N₂ concentration higher than 30% in the Ar/N₂ mixture is required.

Figure 3.3 shows the X-ray diffractograms of ZnSnN₂ thin films grown using a pure nitrogen atmosphere with different conditions listed in table 3.4. The ZnSnN₂ samples (labeled from 21 to 25) were grown to control the atomic ratio between the zinc and tin elements in the films. As well, the discharge voltage was fixed for zinc target at 200 V and the discharge voltage was varied for tin target between -310 and -340 V. The total pressure was fixed to 1.5 Pa. The diffractograms for ZnSnN₂ (21-25) are shown in figure 3.4. Most of the films are X-ray amorphous. However, crystallized films are evidenced for ZSN-30 to ZSN-32.

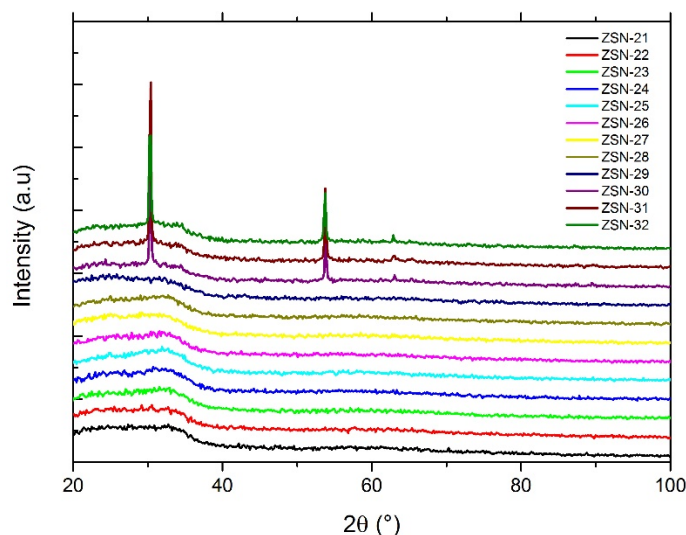


Figure 3.3 XRD of ZnSnN_2 films deposited in pure nitrogen with different parameters of elaboration (table 3.4).

For the samples labeled 26, 27 and 28, our approach was to fix the discharge voltage applied to the targets and to modify the flow rate of the N_2 . The N_2 flow rate values were 30, 60 and 90 sccm. The total pressure of elaboration was fixed to 1.0 Pa. Once again, the obtained films were X-ray amorphous (figure3.3). The increase of the nitrogen flow rate induces an increase of the Sn content (figure3.4). For these experiments, the total pressure was maintained constant by increasing the pumping speed, i.e. closing the throttle valve, while the nitrogen flow rate was increased. Thus, the hysteresis of the sputtering process is expected to be shifted towards low reactive gas flow rates. Since the tin target is less reactive with nitrogen than the zinc one, the hysteresis shift may be more pronounced for the zinc target, inducing a decrease of the film zinc content (i.e., an increase of the tin concentration).

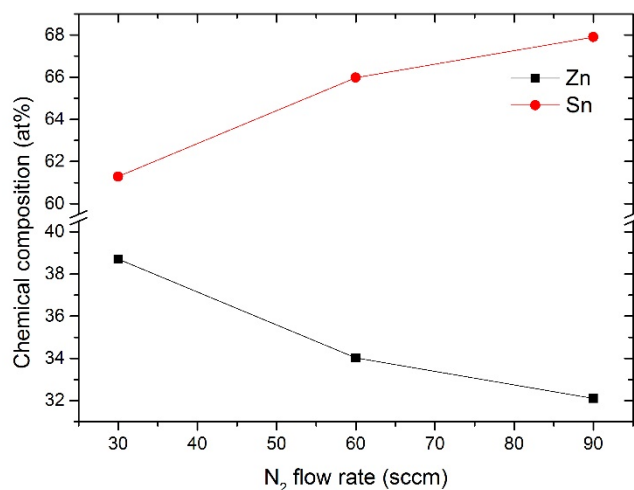


Figure 3.4 Evolution of the zinc and tin content as a function of the flow rate of N_2 .

All the samples obtained until now are X-ray amorphous. In the ZnSnN₂ series labeled from 30 to 32, the total pressure of elaboration was fixed to 1.0 Pa and the discharge voltage was fixed at -230 V for the zinc target. For the tin target, the discharge voltage was varied between -340 and -350 V to increase the atomic ratio of tin element in the films. Within these conditions, the as-deposited thin films are crystallized (figure3.3). Since only two diffraction peaks are evidenced, we can conclude that the ZSN films exhibit a strong preferred orientation. Because of the increase of the zinc target voltage from -200 V to -230 V the kinetic energy of the sputtered atoms may be high enough to ensure a high mobility at the growing film surface and induces the crystallization of the zinc tin nitride phase. For the samples 30 to 32, a crystalline structure is obtained even when the film composition is far from the ZnSnN₂ one. This result suggests that the zinc tin nitride phase exhibit a large domain of non-stoichiometry. Since the chemical composition has been estimated using the EDS method, we are not able to provide an estimation of the nitrogen content. The same is true for the oxygen contamination. Nevertheless, the results obtained in this series of deposition runs clearly evidence that crystalline zinc tin nitride films can be obtained when the tin and zinc targets are sputtered in pure nitrogen atmosphere by fixing the target voltage.

Table3.4 Experimental parameters for the fourth series of ZnSnN₂ thin films.

sample	Flow rate (sccm)		Voltage (V)		Composition (at. %)		Total pressure (Pa)
	Ar	N ₂	Zn	Sn	Zn	Sn	
ZSN-21	0	30	-200	-310	69.46	30.54	1.5
ZSN-22	0	30	-200	-320	57.05	42.94	1.5
ZSN-23	0	30	-200	-330	52.57	47.42	1.5
ZSN-24	0	30	-200	-340	47.52	52.47	1.5
ZSN-25	0	30	-200	-340	45.48	54.51	1.5
ZSN-26	0	60	-200	-340	34.02	65.98	1.0
ZSN-27	0	30	-200	-340	38.71	61.29	1.0
ZSN-28	0	90	-200	-340	32.1	67.9	1.0
ZSN-29	0	30	-220	-340	57.4	42.6	0.7
ZSN-30	0	30	-230	-340	61.67	38.20	1.0
ZSN-31	0	30	-230	-340	62.77	37.23	1.0
ZSN-32	0	30	-230	-350	56.75	43.24	1.0

Finally, by using a reactive co-sputtering process, we succeed to obtain crystalline ZnSnN₂ thin films. The films have been deposited at room temperature on glass and silicon substrates. After an optimization step of the voltage applied to the targets, the zinc tin nitride films exhibit a strong preferred orientation. In the next section, we will focus our work on the structure, microstructure, physical and chemical properties of the crystalline ZnSnN₂ thin films.

3.1.4 Effect of the substrate nature

ZnSnN₂ thin films have been grown on 6 type of substrates with different natures. The influence of the substrate nature on the growth orientation of ZnSnN₂ thin film has been studied. The X-ray diffractograms (figure. 3.5) show that these substrates have no effect on growth orientation and phase structure of ZnSnN₂ thin films. This important result suggest that ZnSnN₂ films would not grow epitaxially on these substrates. Since the substrate nature has no effect on the structure of the as-deposited films, we can use different substrates to characterize our films. In this study we used glass substrates for optical measurements and XRD analyses while silicon substrates were used for TEM, SEM and Mössbauer analyses.

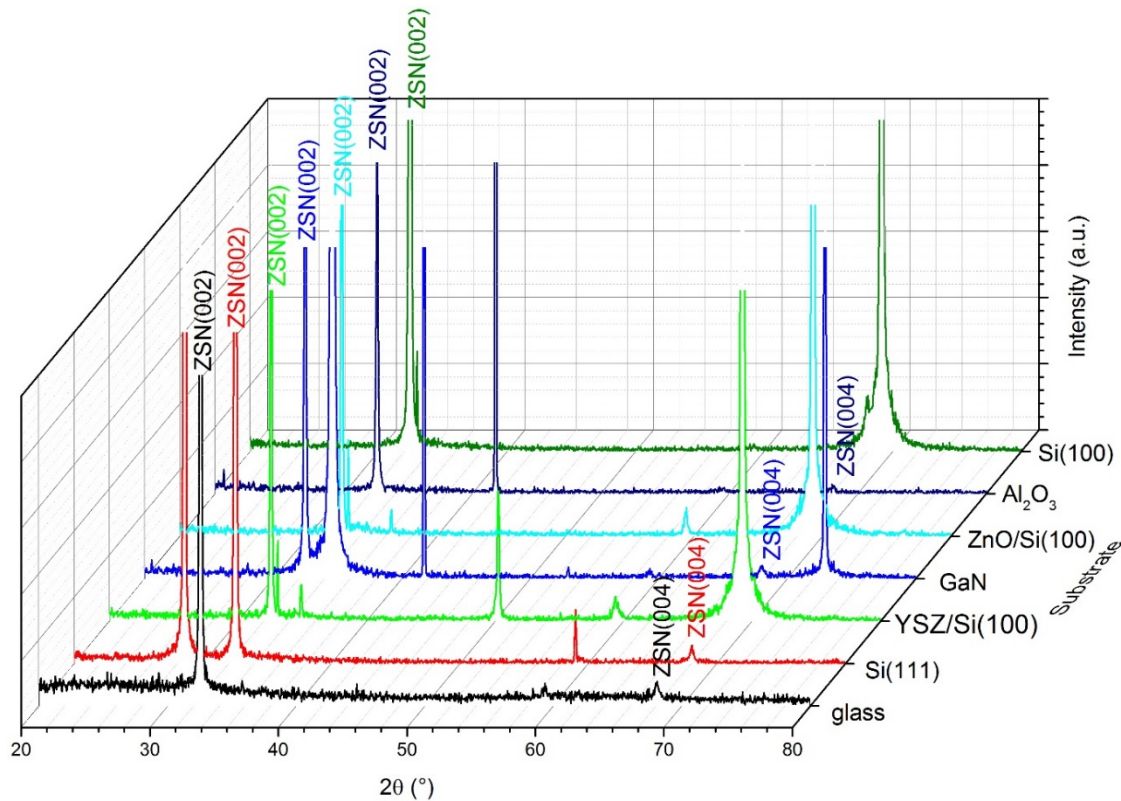


Figure 3.5 X-ray diffractograms of zinc tin nitride thin film with different substrate of growth. The indexations correspond to the hexagonal structure type ($P6_3mc$).

3.2 Crystalline $ZnSnN_2$ thin films structure, microstructure, physical and chemical properties

3.2.1 Introduction

In this section, we characterize crystalline $ZnSnN_2$ thin films grown by reactive magnetron co-sputtering. The $ZnSnN_2$ thin films have been grown at room temperature by using two metallic targets (Zn and Sn) in a pure nitrogen atmosphere. During the growth process the total pressure was kept constant at 1 Pa using a throttle valve and a nitrogen flow rate of 60 sccm. To obtain highly reproducible films, the targets were sputtered by fixing the voltage at -250 V for Zn and -460 V for Sn. These values are slightly different to those reported in the previous section due to the use of new target backing plates. The growth rate for $ZnSnN_2$ was approximately $1.0 \mu\text{m/h}$ and the samples were grown on glass and silicon substrates ($2 \times 2 \text{ cm}^2$). The deposition procedure used for the $ZnSnN_2$ film growth is highly reproducible. A series of 10 deposition run has been performed and all the deposited films exhibit the same structure, the same composition and the same optical properties.

3.2.2 Chemical composition

ZnSnN₂ thin films has been grown in pure nitrogen atmosphere by controlling the target voltage. The film composition has been investigated by EDS (see figure 3.6). Since this method is not accurate to determine the concentration of light elements (nitrogen and oxygen), only the atomic ratio Zn / Sn has been measured. Within the deposition conditions used for this study, this ratio is approximately 1.22. To have more details about the films composition, electron probe microanalysis has been also used.

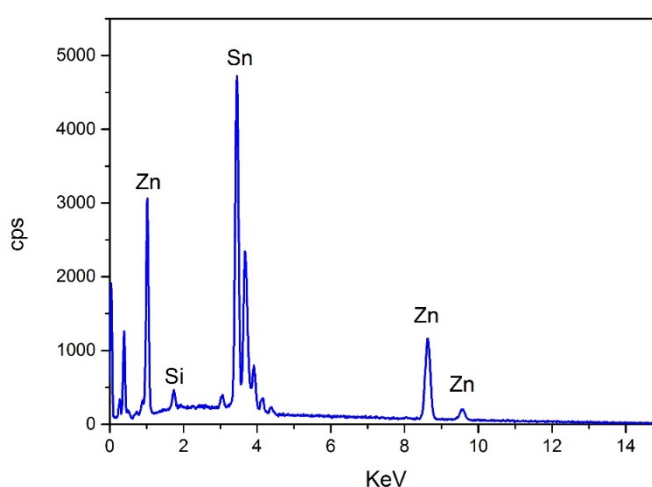


Figure 3.6 EDS spectrum of a ZnSnN₂ film deposited on silicon substrate.

Using this method, (electron probe microanalysis) the following atomic contents have been measured: 25.1% for Zn, 22.1% for Sn, 49.5% for N and 3.3% for O. From these values, the atomic ratio Zn / Sn is 1.14, i.e. very close to that estimated with EDS. Furthermore, the atomic ratio N / (Zn + Sn) is 1.05. Thus, neglecting the oxygen content, the chemical composition of the zinc tin nitride thin film deposited on silicon substrate that can be expressed as Zn_{1.01}Sn_{0.88}N₂, indicating a possible tin understoichiometry (or a zinc and a nitrogen overstoichiometry).

3.2.3 Structure of ZnSnN₂ films

Figure 3.5 shows the X-ray diffractogram of ZnSnN₂ thin films. This film deposited at room temperature on glass substrate is highly crystallized. In the literature Lahourcade *et al.*

also obtained highly ZnSnN_2 crystallized films using RF sputtering on sapphire or GaN substrates at a deposition temperature of 250 °C (figure 3.6(a)) [5]. Another group such as Qin *et al.* obtained poorly crystallized ZnSnN_2 films on quartz and p-Si substrates using room temperature DC reactive sputtering of an alloyed Zn/Sn target (figure 3.6(b)) [6]. Compared to the results reported in literature, reactive co-sputtering at room temperature is a suitable method for depositing highly crystallized ZnSnN_2 films on unmatched substrates (glass and silicon).

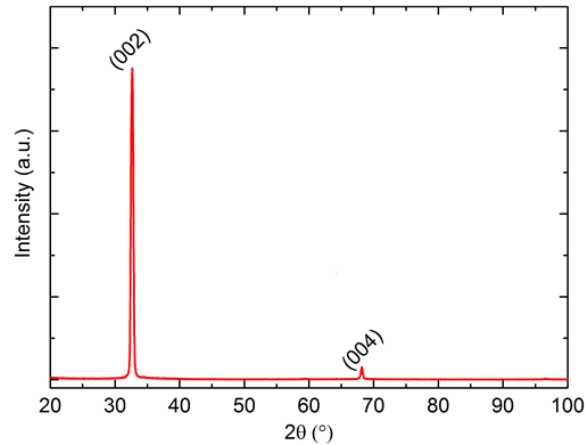


Figure 3.7 X-ray diffractogram of a 1.6 μm thick film deposited on glass substrate. The two indexations correspond to the orthorhombic structure type ($Pna2_1$) with $c = 0.548 \text{ nm}$.

In addition to the high crystallinity level, the diffractogram presented in Figure 3.7 also shows that the ZnSnN_2 film grows with a strong preferred orientation. Since this diffractogram only contains two main peaks (at approx. 32.7 and 68.2°) the precise unit cells cannot be determined. According to the literature data, ZnSnN_2 may crystallize in several structures (as mentioned in chapter 1): orthorhombic $Pna2_1$, orthorhombic $Pmc2_1$, hexagonal $P6_3mc$, or monoclinic. The determination the crystallographic structure is a key point in the study of the ZnSnN_2 . Theoretically, the most stable space group for ZnSnN_2 is predicted to be the orthorhombic $Pna2_1$ one (in comparison to orthorhombic $Pmc2_1$) [5]. According to DFT predictions [7] it corresponds to the fully-cation-ordered ZnSnN_2 , while a fully disordered cation sub-lattice leads to a wurtzite ZnSnN_2 structure. Nevertheless, a debate still exists in literature regarding the ZnSnN_2 structure. A detailed discussion on the film structure is presented in section 4.1.

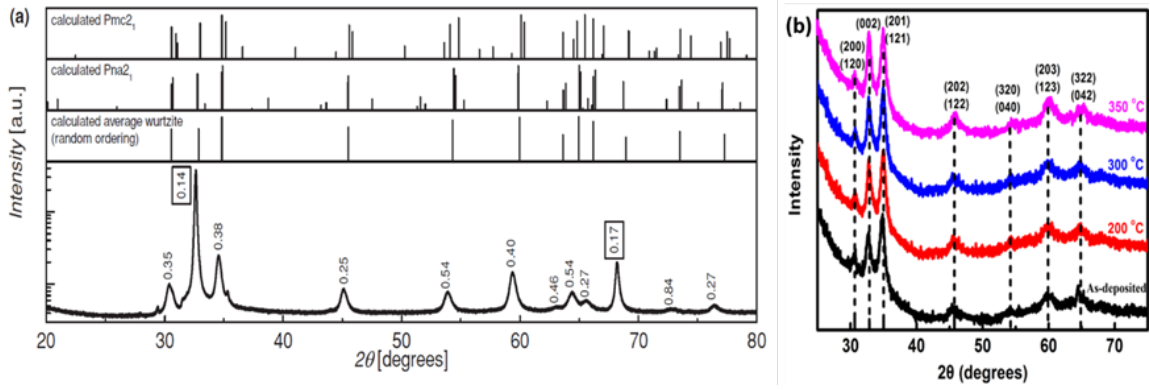


Figure 3.8 (a) X-Ray diffractogram of $ZnSnN_2$ fitted with different structures [5]. (b) X-Ray diffractogram of as deposited and annealed $ZnSnN_2$ films [6].

The phase remains orthorhombic for both ordered and disordered phases with a mixture of the two $Pna2_1$ and $Pmc2_1$ orthorhombic phases for disordered materials [8]. Since the X-ray diffractogram of films deposited in the present study only exhibit two intense diffraction peaks, it is very challenging to determine the film structure from these data. Then, we consider the stable orthorhombic $Pna2_1$ structure to describe the structure of the $ZnSnN_2$ films deposited by reactive sputtering. Nevertheless, further investigations are necessary to clearly determine the structure of the present $ZnSnN_2$ films. Within this hypothesis, the diffraction peaks located at approx. 32.7 and 68.2° have been assigned to the (002) and (004) planes, suggesting that our films exhibit a strong preferred orientation along the [001] direction. From the data presented in Figure 3.6 and excluding an influence of the stress and/or the non-stoichiometry, the c lattice constant has been estimated to 0.5481 nm. This value is very close to that calculated by Lahourcade *et al.* (0.5459 nm) [5] or measured by Quayle *et al.* (0.5462 nm) [9], or Kawamura *et al.* (0.5464 nm) [10]. Using the Scherrer's formula [11] (equation (3.1)), the coherence length has been estimated from the full width at half maximum of the (002) diffraction peak to approximately 20 nm.

$$\tau = \frac{k \cdot \lambda}{\beta \cdot \cos(\theta)} \quad (3.1)$$

Where τ is the grain size, k is a dimensionless shape factor, β is the peak broadening at half-maximum intensity (FWHM) and θ is the Bragg angle.

3.2.4 Microstructure and morphology of $ZnSnN_2$ thin films

The $ZnSnN_2$ film microstructure has been characterized by TEM (Figure 3.9). Bright and dark field images of the film cross section (Figure 3.9(a) and (b), respectively) clearly show

that the film exhibits a columnar microstructure as commonly observed for sputtered nitride coatings [12] or for sputtered ZnSnN_2 films [13]. The width of the columns is ranging between 30 and 60 nm on film top surface. On the other hand, the column width is very low close to the film-substrate interface suggesting a poorly crystallized material during the first stage of growth. The selected area electron diffraction pattern of one column is shown in Figure 3.9(c). This diffraction pattern can be indexed considering a [010] zone axis, confirming the [001] texture evidenced by X-ray diffraction. Since diffraction spots are evidenced in this image, each column can be considered as a single crystal. High resolution image of one column is depicted in Figure 3.9(d). The mean distance between the planes parallel to the film surface is in well agreement with the c lattice constant estimated from X-ray diffraction. As well, the single crystal characteristic has also been by the HTREM. As shown in the inset in figure 3.9(d) a single crystal ZnSnN_2 is clearly evidenced by FFT pattern.

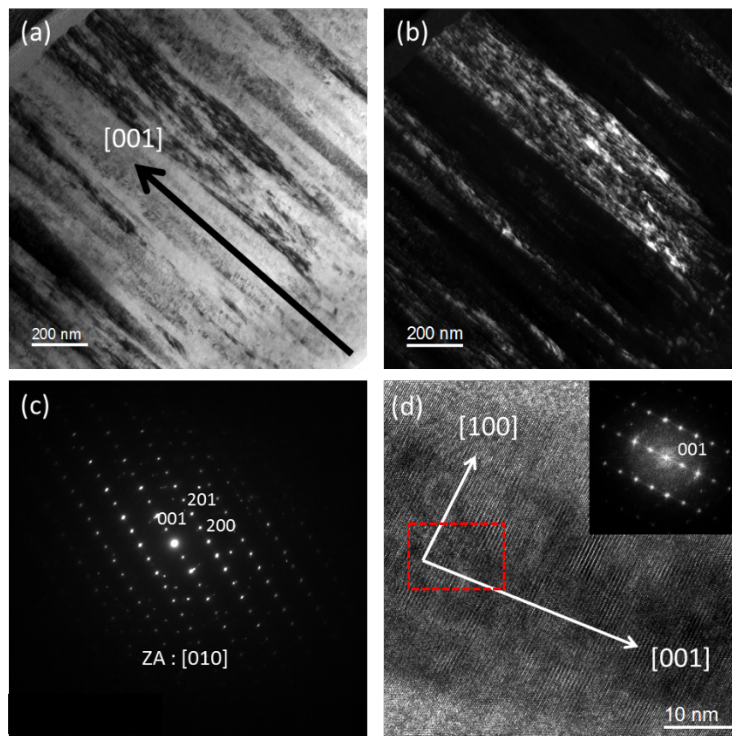


Figure 3.9 TEM characterization of a 1.6 μm thick film deposited on silicon substrate. (a) Bright field image. (b) Dark field image. (c) Selected area electron diffraction of ZnSnN_2 . (d) HRTEM. The inset shows the FFT pattern of the selected ZnSnN_2 grain marked by red box.

As mentioned (section 3.2.2) for the elemental concentration measurement by EPMA, the film contains approx. 3.3 at.% of oxygen. STEM and EDS analyses have been performed on the same thin foil in order to localize the oxygen in the thin film (Figure 3.10 (a) and (b)). Along the analysis line, the zinc and tin concentrations are almost constants. A nitrogen depletion is

evidenced at the column boundaries while the tin and the zinc concentration are constant along the line profile. At these boundaries, the oxygen concentration increases up to 12 at%. These results indicate that the ZnSnN_2 contains two kinds of oxygen atoms. The first one, in the columns, results from the growth of the film due to some oxidation of the sputtered atoms. The second one corresponds to oxygen atoms segregated at the columns boundaries and that may come from the diffusion of molecular oxygen into the film after its synthesis.

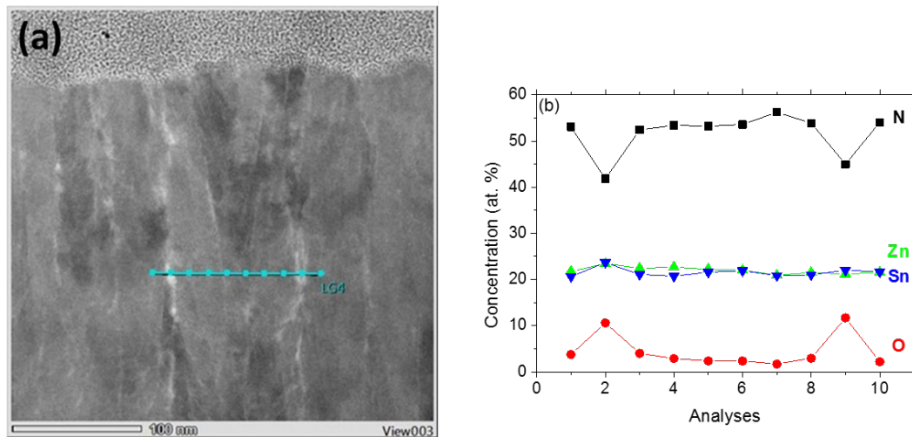


Figure 3.10 (a) STEM image of a ZnSnN_2 thin film, the blue dots on the line indicate the zone of EDS measurements. (b) Chemical composition along the blue line.

To confirm the results presented in figure 3.10, X-ray mapping obtained by STEM and EDS has been done (figure 3.11). Fig 3.11 (a) shown the bright filed image for ZnSnN_2 thin film top view. The figure 3.11 (b), (c), (d) and (e) are showing the distribution of the elements (N, O, Zn and Sn) in the film. As observed on these X-ray images, oxygen is mostly present in the columns boundaries.

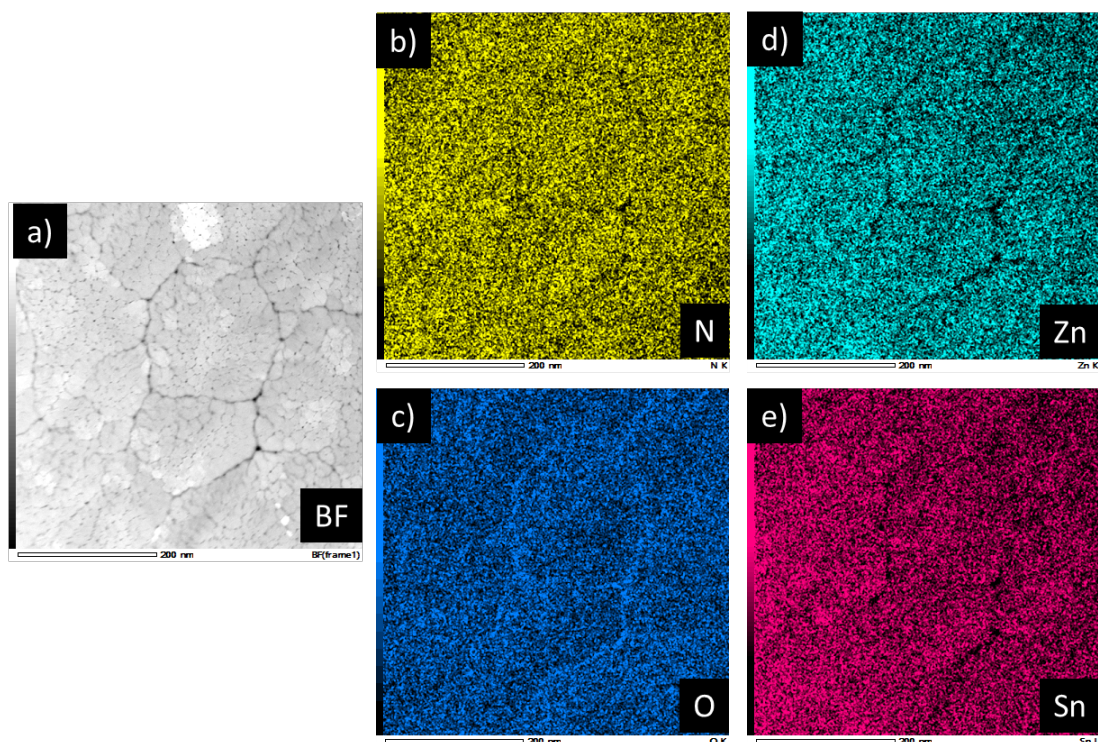


Figure 3.11 X-ray elemental mapping obtained by STEM-EDS for the ZnSnN_2 thin film, (a) bright field image, (b) distribution of nitrogen, (c) distribution of oxygen, (d) distribution of zinc, and (e) distribution of tin.

The film surface morphology has been also characterized by scanning electron microscopy (Figure 3.12(a)). The ZnSnN_2 films exhibit non-faceted grains of few tens of nanometer width. This value is in agreement with that estimated from the TEM cross section (Figure 3.9(a)). To get more quantitative information on the film surface, atomic force microscopy (AFM) analyses have been performed (figure 3.12(b)) using a D3100 AFM equipped with a Nanoscope V electronic from Bruker manufacturer. The images were recorded at ambient conditions (20 °C and 30% RH) and in soft intermittent contact mode (IC-AFM or TappingTM AFM). The surface morphology evidenced by AFM is very similar to that observed by SEM. From the height image, the roughness has been estimated to 1.9 nm.

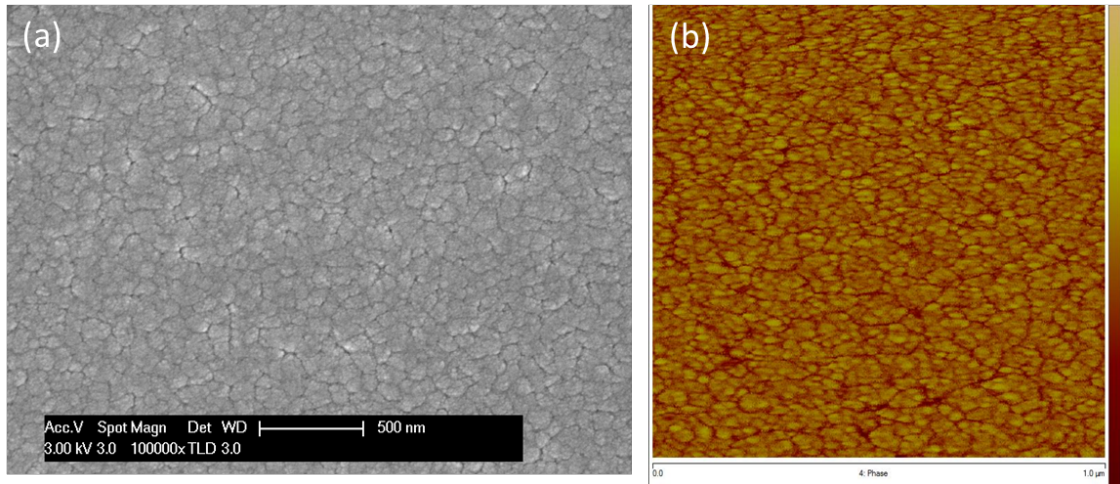


Figure 3.12 surface morphology of a ZnSnN_2 film characterized by SEM. (b) AFM height images of a ZnSnN_2 film, the surface scan is $1 \times 1 \mu\text{m}^2$.

The study of the film structure is not over here in this section. As we mention before (section 3.2.3) it is one of the challenges to determine the ZnSnN_2 film structure. The question is still open for the structure. The results of TEM are compatible with the XRD but both of these techniques have not been judged definitively for the structure of ZnSnN_2 thin film. We will focus to analyse the problem of the structure and try to solve it in the next chapter.

3.2.5 X-ray photoelectron spectroscopy analysis of ZnSnN_2 thin films

XPS analysis has been performed to obtain more information about the chemical environment of atoms in ZnSnN_2 films. Figure 3.13 presents the N 1s core level X-ray photoelectron spectra of a ZnSnN_2 thin film. Two main contributions at 397.9 and 396.0 eV are evidenced. The first one corresponds to organic nitrogen due to the contamination of the film surface that was not removed even after a mild Ar ion etching. Such a mild etching procedure has been used to prevent nitrogen re-sputtering phenomenon during XPS analysis of zinc nitride-based thin films [14].

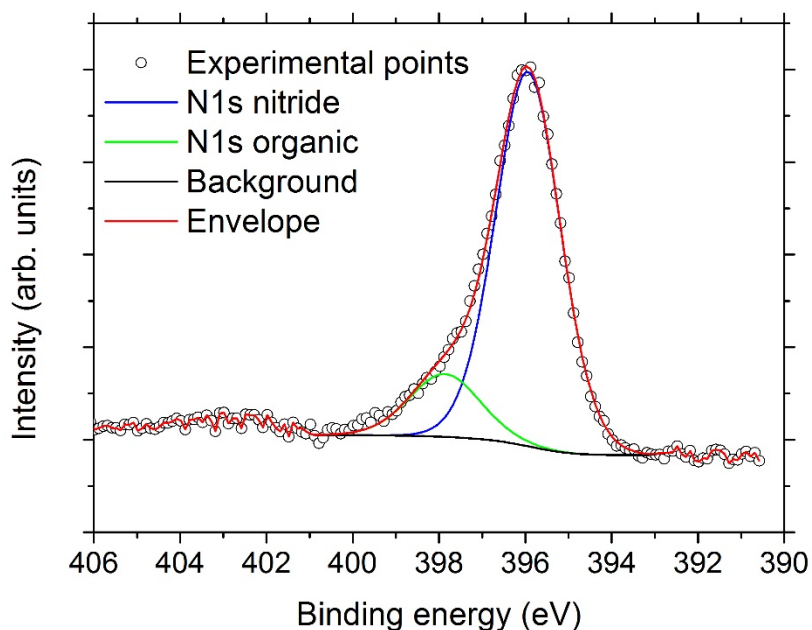


Figure 3.13 High-resolution XPS spectra of N 1s core level.

The second peak at 396.0 eV is related to N–Zn and N–Sn bonds as previously reported by Ye [15]. In the fully ordered zinc tin nitride structure, nitrogen atoms are at the center of a tetrahedron formed by two zinc and two tin atoms. The N 1s XPS peak is then a combination of N–Sn and N–Zn bonds. In a disordered structure, nitrogen atoms are at the center of a tetrahedron formed by four metallic atoms that could be zinc and/or tin. In that case the nitrogen 1s contribution may be a combination of five contributions corresponding to the five different tetrahedra. Thus, the nitrogen spectra should be fitted by five contributions. In the present study, the N 1s XPS peak has been fitted with only one contribution that can be either a combination of N–Sn and N–Zn bonds (ordered structure) or a combination of 5 contributions (disordered structure). In zinc nitride thin films, the N–Zn bonds are evidenced by XPS at 395.8 eV [16] or 396.2 eV [17]. These values are very close to that measured on the present ZnSnN₂ film (396.0 eV). Compared to zinc, tin may present two oxidation states: +II and +IV. Since the oxidation state of tin can be tuned in tin nitride by adjusting the nitrogen content, the N 1s binding energy is dependent on the tin oxidation state in tin nitride. Nitrogen bonded to Sn²⁺ exhibits a XPS component at 397.3 eV, while nitrogen bonded to Sn⁴⁺ exhibits a XPS component at 396.6 eV [18]. Since the N 1s core level does not exhibit a shoulder to high binding energy, N–Sn²⁺ bonds can be excluded in ZnSnN₂, suggesting that the tin atoms bonded with nitrogen have an oxidation state of +IV. XPS spectra of Zn 2p_{3/2} and Sn 3d_{5/2} have a peak position at 1021.0 and 485.6 eV, respectively, in accordance with the results obtained by Ye [15]. Since the chemical shift in zinc-based materials (nitride, oxide and metal) is quite low (approx. 0.3 eV)

[19], the characterization of the XPS Zn 2p_{3/2} core level seems not powerful to characterize the zinc environment in ZnSnN₂ thin films. On the other hand, the chemical shift is more important on the Auger Zn L₃M_{4,5}N_{4,5} peaks. However, these Auger peaks overlap with the Sn 3d core level using Al radiation [14].

3.2.6 Mossbauer spectrometry of ZnSnN₂ thin films

This method is very powerful to obtain information about the chemical environment of tin atoms [20]. Although several groups have already deposited ZnSnN₂ thin films, to the best of our knowledge, no Mossbauer spectrometry characterization of such material has been reported to date in literature. The ¹¹⁹Sn Mossbauer spectra of the ZnSnN₂ recorded at 300 K is depicted in Figure 3.14. A summary of the obtained ¹¹⁹Sn Mossbauer parameters are given in Table 3.5.

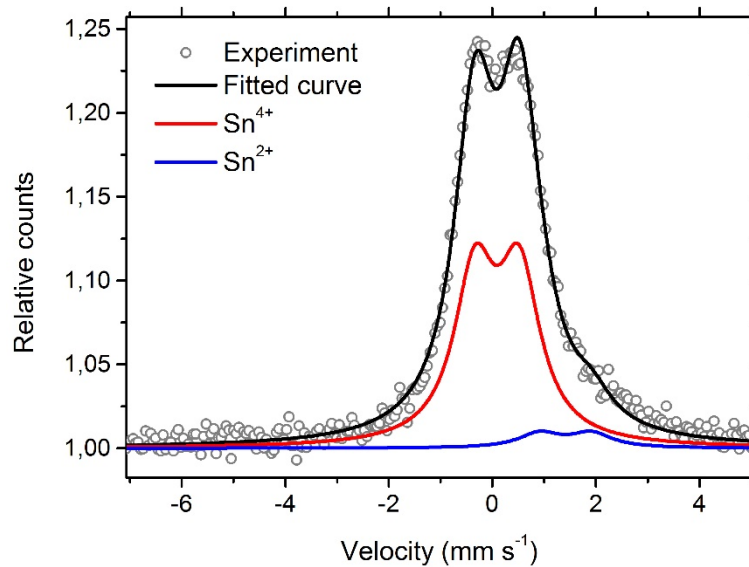


Figure 3.14 Experimental and simulated ¹¹⁹Sn Mossbauer spectra of ZnSnN₂.

The experimental curve is fitted using two contributions. The main one with an isomeric shift (IS) of 1.10 mm/s and a quadrupolar splitting (QS) of 0.86 mm/s is characteristic of Sn⁴⁺ ions in tetrahedral configuration while the second one with IS=2.41 mm/s and QS=1.01 mm/s is related to Sn²⁺ ions. The values of IS and QS measured for Sn⁴⁺ ions on the ZnSnN₂ sample are slightly higher than those reported for tin nitride [21] [22]. The contribution of Sn⁴⁺ ions represents 90% of the Mossbauer signal while the Sn²⁺ one corresponds to 10% (Table 3.5).

Since XPS results show that nitrogen is bonded with Sn⁴⁺ ions and no nitrogen bonded to Sn²⁺ ions, the main Mossbauer contribution may be related to tin ions bounded with nitrogen ones. The Sn²⁺ contribution evidenced by Mossbauer may then be related to tin-based oxides that are observed by STEM at the column boundaries (Figure 3.9).

Table 3.5 Hyperfine parameters of a ZnSnN₂ film (Isomeric Shift and Quadripolar Splitting) and measured ratio of the two components.

Temperature (K)	IS (mm/s)	QS (mm/s)	%
300	1.10	0.86	90
	2.41	1.01	10

3.2.7 Electrical and optical properties of ZnSnN₂

The electrical resistivity of ZnSnN₂ thin film has been measured using the four-point probe method. The value of electrical resistivity at room temperature is $0.229 \pm 0.020 \Omega \text{ cm}$. The electron concentration of ZnSnN₂ thin film determined by Hall effect measurements is $1.0 \times 10^{19} \pm 0.1 \text{ cm}^{-3}$. The electron mobility value was $3.8 \pm 0.3 \text{ cm}^2 \text{ V}^{-1} \text{ s}^{-1}$. The electrical properties of ZnSnN₂ given in literature vary in a wide range. After annealing at 350 °C of DC sputtered films, Qin *et al.* have measured a mobility of $2.07 \text{ cm}^2 \text{ V}^{-1} \text{ s}^{-1}$ and an electron concentration of $6.78 \times 10^{17} \text{ cm}^{-3}$ [6]. The mobility measured by Feldberg *et al.* on films grown by PAMBE is $10 \text{ cm}^2 \text{ V}^{-1} \text{ s}^{-1}$ and the electron concentration is in the $10^{20} - 10^{21} \text{ cm}^{-3}$ range [23]. The electron concentration measured by Lahourcade *et al.* on RF sputtered films is ranging between 5×10^{19} and 10^{21} cm^{-3} [24]. Finally, using a combinatorial approach Fioretti *et al.* obtained mobility in the $1.1\text{--}8.3 \text{ cm}^2 \text{ V}^{-1} \text{ s}^{-1}$ range and carrier density in the $2 \times 10^{18}\text{--}2 \times 10^{20} \text{ cm}^{-3}$ range [13].

The film transmittance in the UV–visible–NIR range is shown in Figure 3.15. Although this film is 1.6 μm thick, it is still transparent in the NIR region (about 25–30%). The film also presents prominent interference fringes caused by the multiple reflections at the three interfaces of the air / ZnSnN₂ / glass substrate sample. The transmittance strongly decreases for wavelengths higher than 1500 nm. The inset on Figure 3.15 corresponds to the Tauc plot to determine the band gap E_g following the general relation [25]:

$$(\alpha E)^r = A(E_g - E) \quad (3.2)$$

Where α is the absorption coefficient determined from the transmittance measurements, E is the photon energy, A is a constant and $r = 2$ or $\frac{1}{2}$ for direct or indirect interband transitions, respectively [25]–[29]. Thus, in a plot of $(\alpha E)^r$ vs. the photon energy, the intersection of the linear extrapolation to the abscissa defines the optical gap E_g ; in the case of different coexisting interband transitions, multiple linear regions might be observed and multiple E_g values, corresponding to each transition, can be identified [30]. Based on the transmittance measurements and using this method, the ZnSnN_2 film exhibits a direct optical band gap of approx. 1.80 ± 0.03 eV.

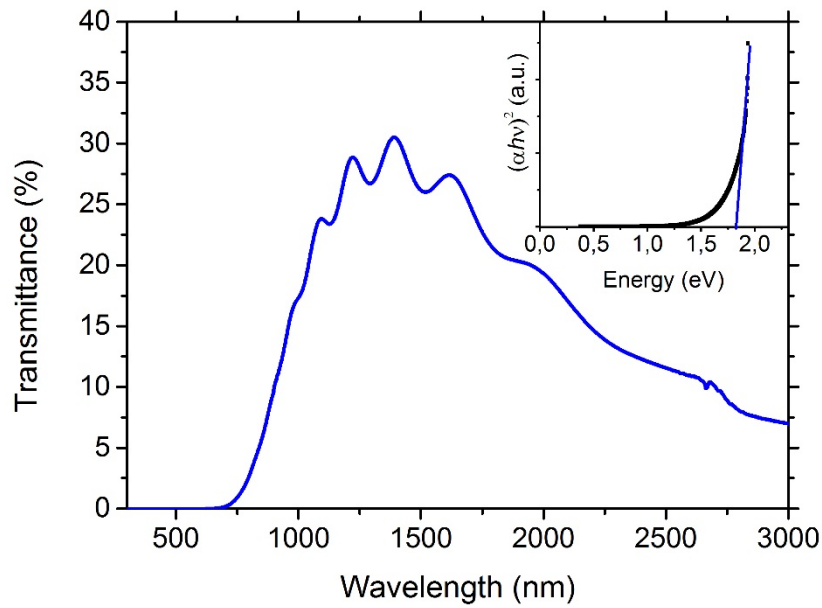


Figure 3.15 Transmittance and Tauc plot of ZnSnN_2 film.

More insights on the optical properties of the textured ZnSnN_2 were deduced by the spectroscopic ellipsometry (SE) analysis. In the case of a transparent film, such as ZnSnN_2 below the optical gap, deposited on a semi-infinite optically opaque substrate, such as silicon, SE actually determines the complex effective dielectric function, or also called pseudo-dielectric function, with a real ϵ_1 and imaginary ϵ_2 parts, taking into account the contributions from the substrate and the film's thickness, as well, due to the interference fringes originating from the film/substrate interface (Figure 3.16 a and b open symbols) [29][31].

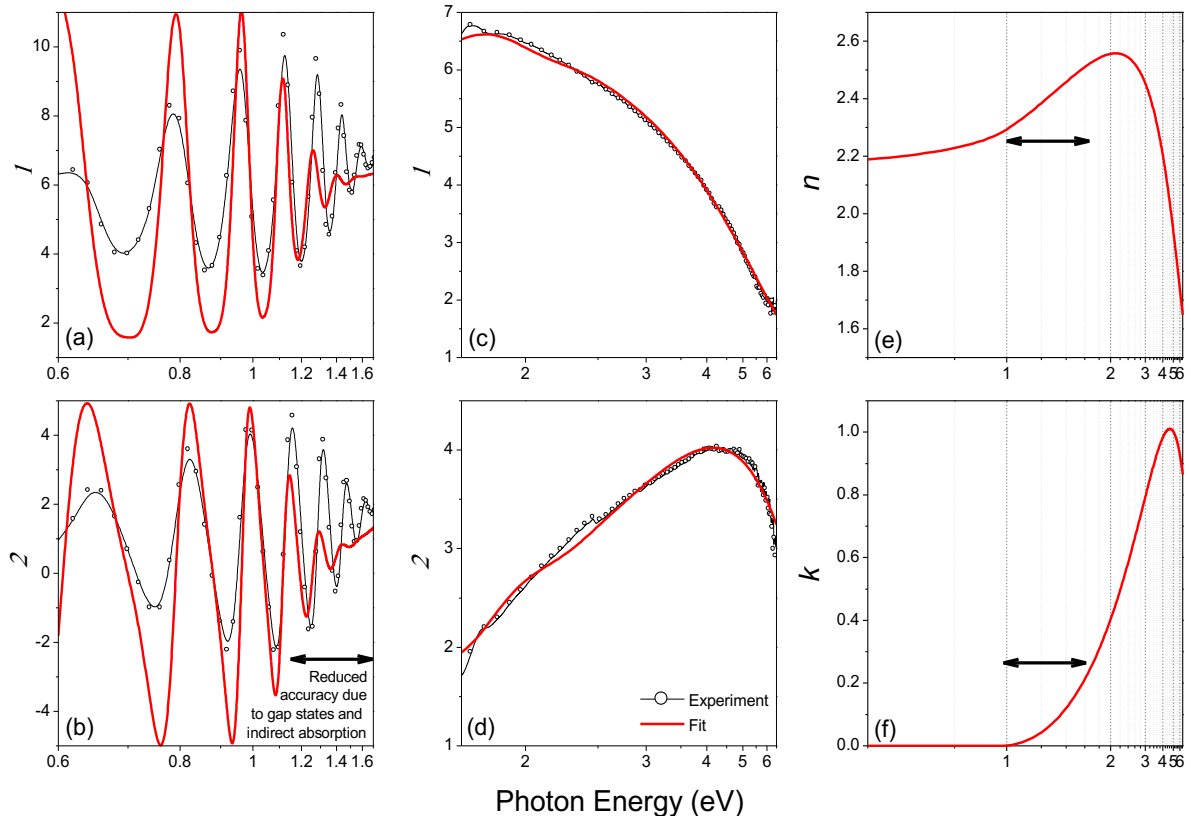


Figure 3.16 Spectra of the (a) real ϵ_1 , and (b) imaginary ϵ_2 of the effective complex dielectric function of ZnSnN_2 film in the range of optical transparency characterized by intense interference fringes. (c) Real ϵ_1 , and (d) imaginary ϵ_2 of the effective complex dielectric function of ZnSnN_2 in the range of high optical absorption, where the sample is nearly opaque. (e) Refractive index n , and (f) extinction coefficient k calculated for a hypothetical semi-infinite ZnSnN_2 based on based TL-fit dispersion parameters. The horizontal arrows indicate the spectral range of reduced accuracy in n and k values due to the inability of the TL model to account the weak indirect and defect absorption.

The absorption coefficient α can be analytically calculated from the ϵ_1 and ϵ_2 values measured by SE and shown in Figure 3.16 a,b,c,d; then Tauc plots for $r=2$ (direct gap) and $\frac{1}{2}$ (indirect gap) can be deduced (Figure 3.17: blue and magenta symbols and lines for direct and indirect gap, respectively). The Tauc plot based on SE data also determines a direct gap of 1.8 eV confirming the transmittance analysis; additional weak optical absorption below the optical gap, the so-called Urbach tail [32]–[35], is also observed. The absorption below the optical gap follows an exponential decay law below the gap value, and it is associated with gap states originating from a disorder in the material [32], [33]. In particular, the extent of this Urbach tail was found to be a characteristic measure of the topological disorder when two local geometries co-exist, such as the trigonal-tetrahedral (or sp^2 - sp^3) sites in diamond-like carbon (DLC) [34]–[37], or the tetrahedral-octahedral sites in $\text{Al}_x\text{Ti}_{1-x}\text{N}$ [29]. Given that the extent of the Urbach

tail is here far shorter than for DLC and $\text{Al}_x\text{Ti}_{1-x}\text{N}$, we may reasonably anticipate that there is no significant topological disorder for ZnSnN_2 supporting also that the Sn^{4+} sites as the exclusive Sn-constituent of ZnSnN_2 and the Sn^{2+} originating from the oxides at the grain boundaries and not from the ZnSnN_2 itself, as suggested by Mössbauer spectrometry and discussed previously. The Tauc plot using the SE data for $r=1/2$, Figure 3.17 red symbols and line, reveals the existence of an indirect gap at 0.8 eV. Although the indirect absorption is generally weak to be detected by SE [38],[39], a clear linear Tauc-type relationship is observed here, although the indirect absorption becomes so weak below 1.5 eV that the interference fringes still manifest in the Tauc plot.

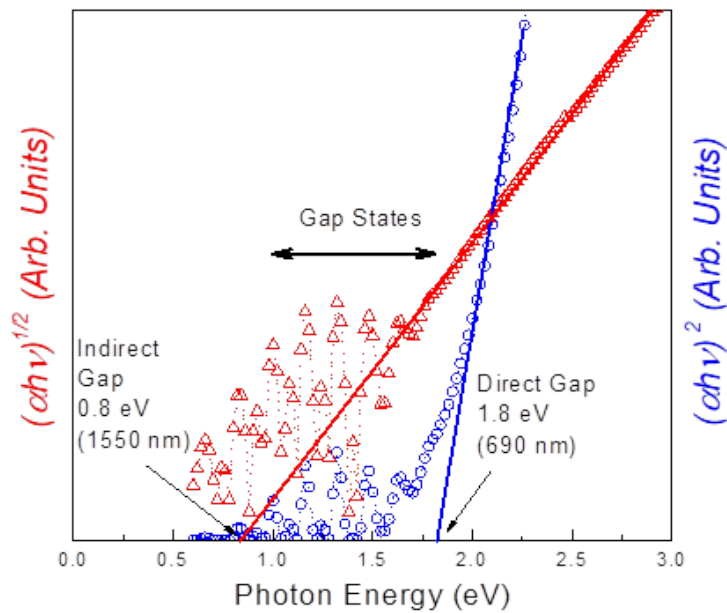


Figure 3.17 Tauc plots for $r=2$ and $1/2$ that corresponds to direct and indirect optical gap in ZnSnN_2 , respectively (blue and red symbols and lines, respectively).

A debate still exists in literature about the origin of the bandgap in ZnSnN_2 . It could be related to different parameters such as the cation disorder in the alloy. Moreover, according to literature, the bandgap energy also depends on the lattice structure that can be either wurtzite-derived orthorhombic ($\text{Pmc}2_1$ or $\text{Pna}2_1$) [5],[23] or monoclinic [23][31]. If such a comparison can be considered when analyzing purely crystalline films obtained for example by PE-MBE, the case is more difficult with polycrystalline films obtained by sputtering. In that case, most of the results report on the presence of a wurtzite phase. But the analyzed films are not generally highly textured or are previously removed to produce a powder-like sample. The calculated fundamental band gap of wurtzite-derived orthorhombic ZnSnN_2 reported in the literature is a

direct one along the Γ k-point of the Brillouin zone and it varies in the wide range from 1.4 to 2.0 eV [6],[40],[41],[42],[43], while the monoclinic ZnSnN_2 with fully disordered cation sublattice exhibits a narrower fundamental band gap, which was reported to be 0.97 eV below the direct band gap of the corresponding orthorhombic phase [40], and whose nature is questionable, as it might be a direct gap along the Γ k-point or an indirect gap between the Y and Γ k-points. Thus, our experimental value of the direct optical band gap is in agreement with the calculated values of wurtzite-derived orthorhombic ZnSnN_2 and with most of the experimental published works, while the reported indirect gap of 0.8 eV (about 1 eV below the direct in agreement with the literature [40] calls for a more detailed look into the effect of cation ordering in the lattice on the fundamental gap of ZnSnN_2 ; this is of paramount importance for applications such as photovoltaics, which require a broadband optical absorption.

SE can be also used to determine the dispersion of refractive index n and extinction coefficient k . In order to evaluate the spectral dependence of the dielectric function of ZnSnN_2 films, we fitted the experimental dielectric function spectra of Figure 3.16 a,b,c,d using the modified Tauc-Lorentz (TL) model [44], in combination with the three-phase model (air/ ZnSnN_2 film/c-Si substrate) [45]. In TL model, the imaginary part of the dielectric function is determined by multiplying the Tauc joined density of states for direct gap [46][32] by the ε_2 obtained from the Lorentz oscillator model [54] resulting in an asymmetric Lorentzian located at an energy E_0 and with broadening C . The imaginary part ε_2 of a TL oscillator is described by the following expressions [52]:

$$\varepsilon_2(E) = \frac{AE_0C(E-E_0)^2}{(E^2-E_0^2)^2+C^2E^2} \times \frac{1}{E}, \quad E > E_g \quad (3.3a)$$

$$\varepsilon_2(E) = 0, \quad E \leq E_g \quad (3.3b)$$

and the real part ε_1 is obtained by Kramers–Kronig integration. The best TL parameters and the film thickness are the result of the mean square error (MSE) minimization. In order to increase the accuracy of the fit, first we performed a fitting in the range 1.7–6.5 eV (the range dominated by the optical absorption and where the effect of thickness to the spectra is minimal), as shown in Figure 3.16 c,d, and then we performed a second fit in the entire range 0.6–6.5 eV keeping all the TL parameters constant at best values and letting the film thickness as a free parameter. By this procedure we got a film thickness value of 1.55 μm in excellent agreement with the value (1.6 μm) extracted from the profilometry and TEM experiments. Figure 3.16 a,b show that there is a remarkable agreement of the spectral positions of the interference fringes between the experimental spectra and the fits in the range 0.6–1.1 eV, which provides high confidence

to the fit results; the height of the fringes might be greatly affected by the roughness of the film, which was not taken into account in our fits. Note that the TL model does not take into account neither the Urbach nor the indirect absorption [47], therefore, the fit results might be of reduced accuracy in the spectral range 1.1–1.8 eVs, as suggested by the spectral shifts of the interference fringes between experiment and fit and indicated by the horizontal arrows in Figure 3.16. Following these procedures, we conclude to the n and k spectra reported in Figure 3.16 e,f., which are in remarkable agreement with Deng et al. [2].

3.3 Effect of base pressure before the film growth

As we have shown in the previous section, as-deposited ZnSnN_2 films contain few at. % of oxygen and the main part of this oxygen contamination is located at the column boundaries. Two main phenomena may be considered to explain the occurrence of oxygen in our films: oxygen contamination during the film growth and oxidation of the as-deposited films during air exposure. Since it is hard to reduce the air contamination after the film synthesis, we tried to manage the quantity of oxygen coming from the deposition step. This can be done by modifying the base pressure inside the chamber. In this part, ZnSnN_2 thin film have been grown with three base pressure of the sputtering chamber (1.5×10^{-5} , 9.5×10^{-6} and 6.6×10^{-6} mbar). For this series of elaboration, the deposition conditions were kept constant and only the base pressure was varied (Table 3.6). The increase of the impurities content was with decreasing the time of the pumping the chamber to obtain the base pressure. It has to mentioned that the impurities correspond to residual gas (oxygen, water vapor, ...).

Table 3.6 Experimental parameters of the series of ZnSnN_2 thin films with different base pressures

sample	Base pressure (mbar)	Voltage (V)		Flow rate	Thickness (μm)	Total pressure (Pa)
		Zn	Sn	(sccm) N ₂		
ZSN-210	1.5×10^{-5}	-270	-430	65	1.1	1.0
ZSN-211	9.5×10^{-6}	-270	-430	65	1.03	1.0
ZSN-212	6.6×10^{-6}	-270	-430	65	0.94	1.0

The influence of impurities was clearly observed in the structure of the films with the X-ray diffractogram (figure 3.18). Depending on the base pressure, the texture of the film is tuned. With 1.5×10^{-5} mbar the film is crystallized with small grains with four major peaks (100), (002), (101) and (110) for the hexagonal structure $P6_3mc$ (figure 3.18). By decreasing the base pressure to 9.5×10^{-6} mbar, the X-ray diffractogram shows that the intensity of peaks was increased, indicating a higher crystallinity of the samples. The film deposited with the lowest base pressure (6.6×10^{-6} mbar) exhibit a strong texture along the [002] direction. Barna et al. [48] have studied the effect of the presence of impurities in the thin films by sputtering. They show in they may have a real impact in grain size for the crystal growth.

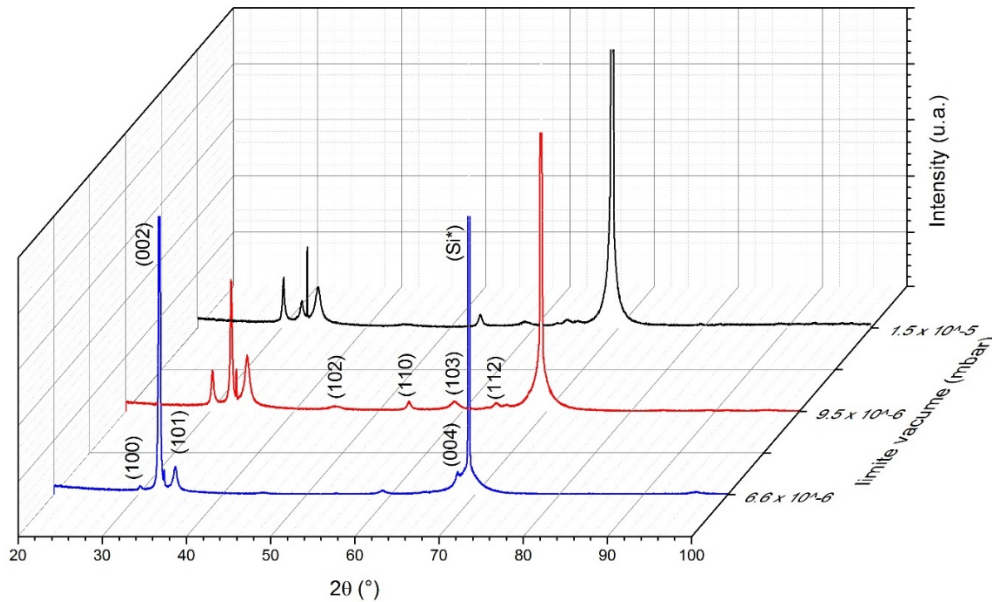


Figure 3.18 X-ray diffractograms of zinc tin nitride thin films with different vacuum limit of growth. The indexations correspond to the hexagonal structure type ($P6_3mc$).

The selected area electron diffraction (SAED) pattern of the films obtained using the lowest base pressure evidences polycrystalline material (Figure 3.19). From these diffraction rings, we have determined the interplanar spacing considering a hexagonal structure. These distances have been compared to those determined from XRD analyses. (Table 3.7). Although higher values are obtained by TEM, these results are in good agreement suggesting that the film crystallizes in the hexagonal $P6_3mc$ structure.

Table 3.7 comparison of the interplanar distance in ZnSnN₂ film deduced from electron and X-ray diffraction measurements.

Point	SAED d(Å)	DRX d(Å)	(hkl)
1	3.06	2.95	(100)
5	2.82	2.75	(002)
9	2.69	2.60	(101)
12	2.08	2.01	(102)
16	1.76	1.70	(110)
20	1.62	1.56	(103)
24	1.50	1.47	(200)

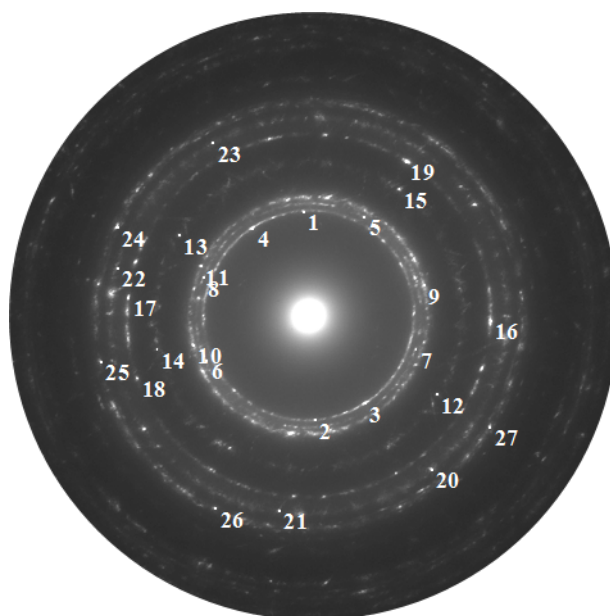


Figure 3.19 Selected area electron diffraction of ZnSnN₂ thin film with lower base pressure (ZSN-210).

Figure 3.20 shows the ¹¹⁹Sn Mössbauer spectra of the ZnSnN₂ recorded at 300 K grown with different base pressures (table 3.6). A summary of the Mössbauer parameters are given in Table 3.8. As well, the experimental curve can be fitted using two contributions only the different was to divide the site for Sn⁺⁴ in two peaks. Suggesting two sites for Sn⁺⁴ seems to be more

compatible with the hexagonal structure where we can obtain two sites for the tin element in the structure.

For ZnSnN_2 grown at a base pressure 1.5×10^{-5} mbar the contributions with an isomeric shift (IS) of (1.38 and 1.01) mm/s and a quadrupolar splitting (QS) of (0.85 and 0.85) mm/s are related to Sn^{4+} ions in tetrahedral configuration while the second one with an IS of 3.04 mm/s is related to Sn^{2+} ions. For ZnSnN_2 grown at 9.5×10^{-6} mbar the main contributions with an isomeric shift (IS) of (1.32 and 0.97) mm/s and a quadrupolar splitting (QS) of (0.93 and 0.86) mm/s are characteristic of Sn^{4+} ions in tetrahedral configuration while the second one with IS=3.06 mm/s is related to Sn^{2+} ions. Finally for ZnSnN_2 grown at a base pressure 6.6×10^{-6} mbar the main contributions with an isomeric shift (IS) of (1.30 and 0.96) mm/s and a quadrupolar splitting (QS) of (0.98 and 0.86) mm/s are characteristic of Sn^{4+} ions in tetrahedral configuration while the second one with IS=3.08 mm/s is related to Sn^{2+} ions.

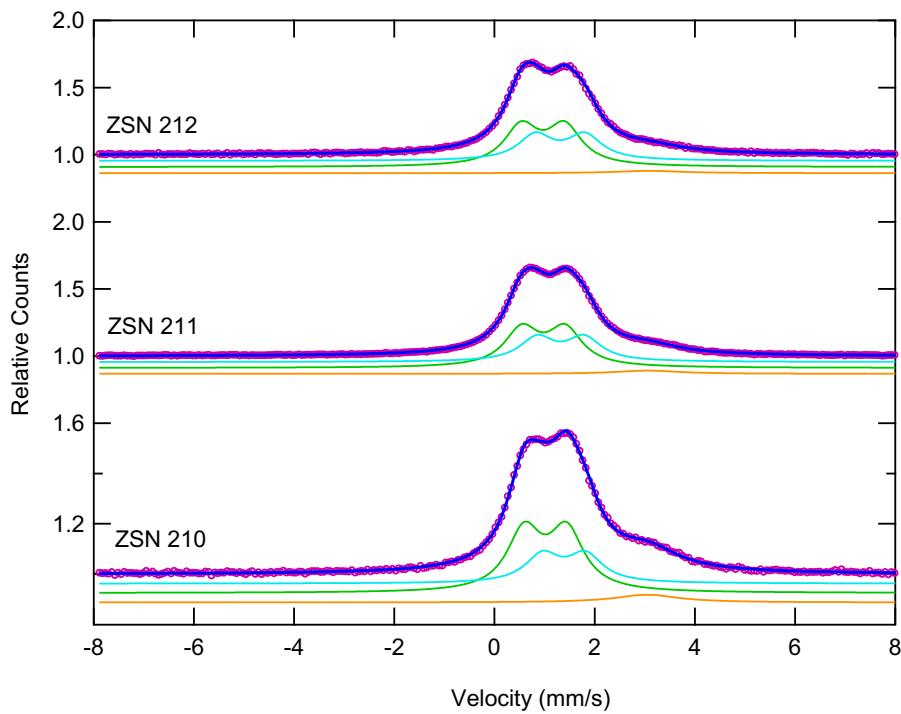


Figure 3. 20 Experimental and simulated ^{119}Sn Mössbauer spectra of ZnSnN_2 growth with different pressures.

We can note that the contribution of Sn^{2+} decreases with the base pressure. This result may be explained with the reduced oxygen content when increasing the pressure inside the chamber. This result has been confirmed by qualitative SIMS measurements (not shown here).

Table 3.8 *Hyperfine parameters of a ZnSnN₂ film growth with different base pressure (Isomeric Shift and Quadripolar Splitting) and measured ratio of the two components.*

Sample	Base Pressure (mbar)	Site	IS (mm/s)	QS (mm/s)	%
ZSN 210	1.5×10^{-5}	Sn ⁺⁴	1.38	0.85	27
		Sn ⁺⁴	1.01	0.85	59
		Sn ⁺²	3.04		14
ZSN 211	9.5×10^{-6}	Sn ⁺⁴	1.32	0.93	36
		Sn ⁺⁴	0.97	0.86	56
		Sn ⁺²	3.06		8
ZSN 212	6.6×10^{-6}	Sn ⁺⁴	1.30	0.98	36
		Sn ⁺⁴	0.96	0.86	57
		Sn ⁺²	3.08		6

The electrical resistivity of ZnSnN₂ thin films grown with different base pressures has been measured using the four-point probe method. The value of electrical resistivity at room temperature was varied with the base pressure around (1.27, 0.50 and 0.23) Ω.cm for the base pressure (1.5×10^{-5} , 9.5×10^{-6} and 6.6×10^{-6}) mbar. Figure 3.21 shows the evolution of the resistivity as a function of the base pressure. Since the effect of the base pressure is expected to change the oxygen contamination in the ZnSnN₂ columns, the low resistivity of the film deposited at the low base pressure should be related to the oxygen content of the nitride grains.

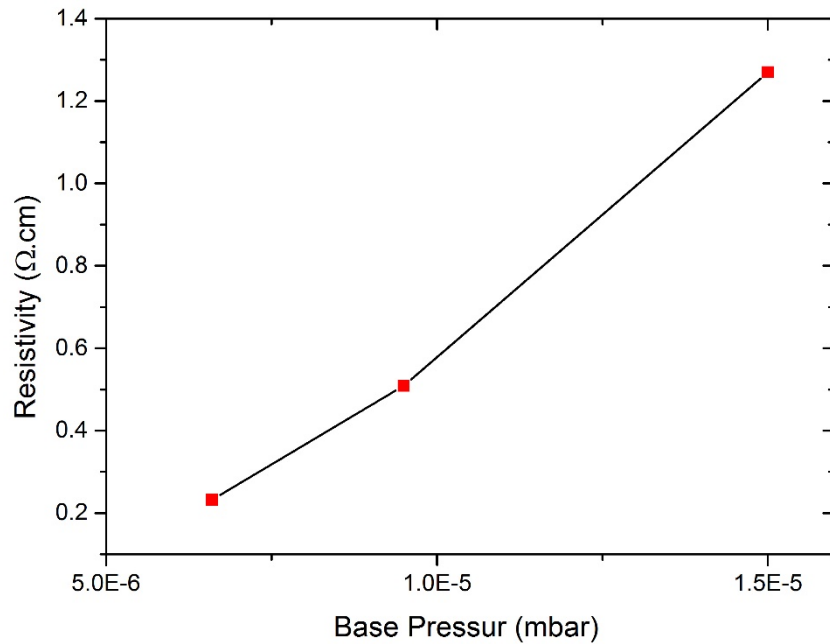


Figure 3.21 The evolution of the resistivity of $ZnSnN_2$ thin films as a function of the base pressure.

However, the film transmittance and the optical band gap of this film series have determined by UV-vis spectroscopy. Figure 3.23 show the transmission spectra of $ZnSnN_2$ thin films with different base pressures. The sample grown at a base pressure of 6.6×10^{-6} mbar exhibits similar spectra than that obtained in the previous section and in reference [49]. We may note that, when decreasing the base pressure, the part of the spectra in the NIR range (1500-3300 nm) increases.

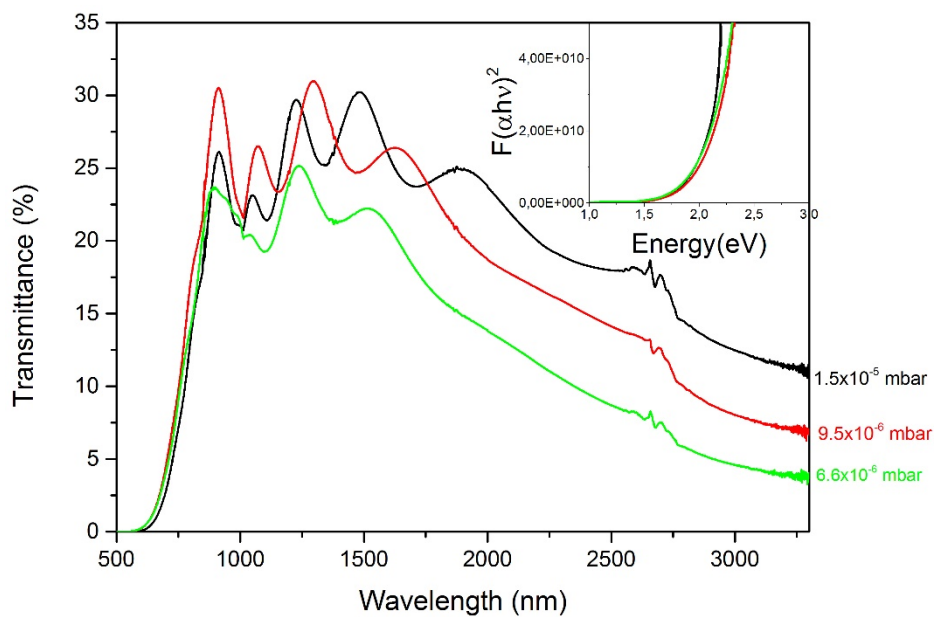


Figure 3.22 Transmission spectra of $ZnSnN_2$ thin films deposited with different base pressures and Tauc plots of $ZnSnN_2$ thin films

The absorption drop can be linked to the free carrier absorption, free carrier coming from the defect density. Here in the reduction of the droop when the base pressure increases may be interpreted as a reduction of the free carrier concentration and then a reduction of the number of defects in the materials.

3.4 Conclusion

In the first part of this chapter, we have reported the growth of zinc tin nitride by using a reactive co-sputtering process. In addition, we have investigated the effect of the different deposition parameters to obtain crystallized ZnSnN₂ films. To obtain reproducible films, we have observed that the sputtering of the zinc and tin targets has to be done by fixing the target voltage

In a second part, we have showed that highly crystalline ZnSnN₂ thin films can be deposited at room temperature on unmatched substrates: glass and silicon. After an optimization step of the applied voltage, the zinc tin nitride films exhibit a strong preferential orientation in the [001] direction considering an orthorhombic structure. The film microstructure has been characterized by cross-section TEM. The chemical composition indicates that the films are slightly under stoichiometric in tin (or over stoichiometric in zinc and nitrogen). XPS and Mössbauer spectrometry have been used to characterize the chemical environment on zinc, tin and nitrogen atoms. From XPS results, the N 1s core level can be fitted with one contribution due the bonds formed by nitrogen atoms with zinc and tin. The position of the nitrogen peak excludes the formation of bonds with Sn²⁺ ions. However, such ions have been evidenced by Mössbauer spectrometry and may correspond the oxide phase evidenced by TEM at the columns boundaries. The main part of the tin ions is evidenced by Mössbauer spectrometry as Sn⁴⁺ ions in tetrahedral configuration. Electrical and optical properties of the film have been investigated. Zinc tin nitride films exhibit an electron mobility at room temperature close to 3.8 cm² V⁻¹ s⁻¹ and an optical band gap of 1.8 eV as measured independently from UV–visible spectrometry and ellipsometry. The values of the refractive index and coefficient of extinction have been estimated. The results presented in this manuscript confirm that ZnSnN₂ is a suitable material for solar absorption.

Finally, an experimental study has been done to investigate the effect of the base pressure of the chamber on the structure and the microstructure of ZnSnN₂ thin films. Optical absorption, electrical resistivity and Mössbauer spectroscopy have been employed to determine

the physio-chemical proprieties of this study. The use of a low base pressure induces a decrease of the film oxygen concentration as confirmed by Mössbauer spectroscopy. Thus, an improvement of the film crystallinity.

Reference

- [1] S. Bouhtiyya *et al.*, « Application of sputtered ruthenium nitride thin films as electrode material for energy-storage devices », *Scr. Mater.*, vol. 68, n° 9, p. 659-662, mai 2013.
- [2] F. Deng *et al.*, « Determination of the basic optical parameters of ZnSnN₂ », *Opt. Lett.*, vol. 40, n° 7, p. 1282-1285, avr. 2015.
- [3] M. Futsuhara, K. Yoshioka, et O. Takai, « Structural, electrical and optical properties of zinc nitride thin films prepared by reactive rf magnetron sputtering », *Thin Solid Films*, vol. 322, n° 1–2, p. 274-281, juin 1998.
- [4] S. Choi, J. Kang, J. Park, et Y.-C. Kang, « Tin nitride thin films fabricated by reactive radio frequency magnetron sputtering at various nitrogen gas ratios », *Thin Solid Films*, vol. 571, Part 1, p. 84-89, nov. 2014.
- [5] L. Lahourcade, N. C. Coronel, K. T. Delaney, S. K. Shukla, N. A. Spaldin, et H. A. Atwater, « Structural and Optoelectronic Characterization of RF Sputtered ZnSnN₂ », *Adv. Mater.*, vol. 25, n° 18, p. 2562-2566, mai 2013.
- [6] R. Qin *et al.*, « Semiconducting ZnSnN₂ thin films for Si/ZnSnN₂ p-n junctions », *Appl. Phys. Lett.*, vol. 108, n° 14, p. 142104, avr. 2016.
- [7] T. D. Veal *et al.*, « Band Gap Dependence on Cation Disorder in ZnSnN₂ Solar Absorber », *Adv. Energy Mater.*, vol. 5, n° 24, p. n/a-n/a, déc. 2015.
- [8] N. Senabulya *et al.*, « Stabilization of orthorhombic phase in single-crystal ZnSnN₂ films », *AIP Adv.*, vol. 6, n° 7, p. 075019, juill. 2016.
- [9] P. C. Quayle, K. He, J. Shan, et K. Kash, « Synthesis, lattice structure, and band gap of ZnSnN₂ », *MRS Commun.*, vol. 3, n° 03, p. 135–138, 2013.
- [10] F. Kawamura, N. Yamada, M. Imai, et T. Taniguchi, « Synthesis of ZnSnN₂ crystals via a high-pressure metathesis reaction », *Cryst. Res. Technol.*, vol. 51, n° 3, p. 220-224, mars 2016.
- [11] Harold Klug et Leroy Alexander, *X-ray diffraction procedures for polycrystalline and amorphous materials*, 2^e éd. New York: John Wiley & Sons, 1974.
- [12] L. Hultman, « Thermal stability of nitride thin films », *Vacuum*, vol. 57, n° 1, p. 1-30, avr. 2000.
- [13] A. N. Fioretti *et al.*, « Combinatorial insights into doping control and transport properties of zinc tin nitride », *J. Mater. Chem. C*, vol. 3, n° 42, p. 11017-11028, oct. 2015.

- [14] D. G. Georgiev, J. P. Moening, S. Naleshwar, et A. H. Jayatissa, « Microstructure and electronic properties of zinc nitride thin films », in *2009 IEEE Nanotechnology Materials and Devices Conference*, 2009, p. 33-37.
- [15] S. Ye, « Preparation, characterization, and device applications of zinc tin nitride and zinc tin oxynitride materials ». PhD, UCLA, 2015.
- [16] M. B. Haider, « XPS Depth Profile Analysis of Zn₃N₂ Thin Films Grown at Different N₂/Ar Gas Flow Rates by RF Magnetron Sputtering », *Nanoscale Res. Lett.*, vol. 12, n° 1, p. 5, janv. 2017.
- [17] N. Tabet, M. Faiz, et A. Al-Oteibi, « XPS study of nitrogen-implanted ZnO thin films obtained by DC-Magnetron reactive plasma », *J. Electron Spectrosc. Relat. Phenom.*, vol. 163, n° 1, p. 15-18, avr. 2008.
- [18] C. M. Caskey *et al.*, « Synthesis of a mixed-valent tin nitride and considerations of its possible crystal structures », *J. Chem. Phys.*, vol. 144, n° 14, p. 144201, avr. 2016.
- [19] M. Futsuhara, K. Yoshioka, et O. Takai, « Structural, electrical and optical properties of zinc nitride thin films prepared by reactive rf magnetron sputtering », *Thin Solid Films*, vol. 322, n° 1, p. 274-281, juin 1998.
- [20] P. E. Lippens, « Interpretation of the 119Sn Mossbauer isomer shifts in complex tin chalcogenides », *Phys. Rev. B*, vol. 60, n° 7, p. 4576-4586, août 1999.
- [21] L. Baggetto, N. A. M. Verhaegh, R. A. H. Niessen, F. Roozeboom, J.-C. Jumas, et P. H. L. Notten, « Tin Nitride Thin Films as Negative Electrode Material for Lithium-Ion Solid-State Batteries », *J. Electrochem. Soc.*, vol. 157, n° 3, p. A340-A347, janv. 2010.
- [22] R. S. Lima, P. H. Dionisio, W. H. Schreiner, et C. Achete, « Magnetron sputtered tin nitride », *Solid State Commun.*, vol. 79, n° 5, p. 395-398, août 1991.
- [23] N. Feldberg *et al.*, « Growth, disorder, and physical properties of ZnSnN₂ », *Appl. Phys. Lett.*, vol. 103, n° 4, p. 042109, juill. 2013.
- [24] L. Lahourcade, N. C. Coronel, K. T. Delaney, S. K. Shukla, N. A. Spaldin, et H. A. Atwater, « Structural and Optoelectronic Characterization of RF Sputtered ZnSnN₂ », *Adv. Mater.*, vol. 25, n° 18, p. 2562-2566, mai 2013.
- [25] J. Tauc, R. Grigorovici, et A. Vancu, « Optical Properties and Electronic Structure of Amorphous Germanium », *Phys. Status Solidi B*, vol. 15, n° 2, p. 627-637.
- [26] D. B. Buchholz, J. Liu, T. J. Marks, M. Zhang, et R. P. H. Chang, « Control and Characterization of the Structural, Electrical, and Optical Properties of Amorphous

Zinc–Indium–Tin Oxide Thin Films », *ACS Appl. Mater. Interfaces*, vol. 1, n° 10, p. 2147-2153, oct. 2009.

[27] Z. Wang, U. Helmersson, et P.-O. Käll, « Optical properties of anatase TiO₂ thin films prepared by aqueous sol–gel process at low temperature », *Thin Solid Films*, vol. 405, n° 1, p. 50-54, févr. 2002.

[28] C. Charitidis, P. Patsalas, et S. Logothetidis, « Optical and mechanical performance of nanostructured cerium oxides for applications in optical devices », *J. Phys. Conf. Ser.*, vol. 10, n° 1, p. 226, 2005.

[29] N. Pliatsikas, A. Siozios, S. Kassavetis, G. Vourlias, et P. Patsalas, « Optical properties of nanostructured Al-rich Al_{1-x}Ti_xN films », *Surf. Coat. Technol.*, vol. 257, p. 63-69, oct. 2014.

[30] F. P. Koffyberg, K. Dwight, et A. Wold, « Interband transitions of semiconducting oxides determined from photoelectrolysis spectra », *Solid State Commun.*, vol. 30, n° 7, p. 433-437, mai 1979.

[31] G. Bauer et W. Richter, Éd., *Optical Characterization of Epitaxial Semiconductor Layers*. Berlin Heidelberg: Springer-Verlag, 1996.

[32] S. Zollner *et al.*, « Optical properties of bulk and thin-film SrTiO₃ on Si and Pt », *J. Vac. Sci. Technol. B Microelectron. Nanometer Struct. Process. Meas. Phenom.*, vol. 18, n° 4, p. 2242-2254, juill. 2000.

[33] A. S. Ferlauto *et al.*, « Analytical model for the optical functions of amorphous semiconductors and its applications for thin film solar cells », *Thin Solid Films*, vol. 455, p. 388-392, mai 2004.

[34] C. Mathioudakis, G. Kopidakis, P. Patsalas, et P. C. Kelires, « Disorder and optical properties of amorphous carbon », *Diam. Relat. Mater.*, vol. 16, n° 10, p. 1788-1792, oct. 2007.

[35] P. Patsalas, « Optical properties of amorphous carbons and their applications and perspectives in photonics », *Thin Solid Films*, vol. 519, n° 12, p. 3990-3996, avr. 2011.

[36] G. Fanchini et A. Tagliaferro, « Disorder and Urbach energy in hydrogenated amorphous carbon: A phenomenological model », *Appl. Phys. Lett.*, vol. 85, n° 5, p. 730-732, juill. 2004.

[37] C. Casiraghi, A. C. Ferrari, et J. Robertson, « Raman spectroscopy of hydrogenated amorphous carbons », *Phys. Rev. B*, vol. 72, n° 8, p. 085401, août 2005.

[38] R.W. Collins, A.S. Ferlauto, *Optical physics of materials*, in: H.G. Tompkins, E.A. Irene (Eds.), *Handbook of Ellipsometry*, Springer Verlag GmbH, Heidelberg, 2005, p. 182. .

- [39] A. O'Hara, T. N. Nunley, A. B. Posadas, S. Zollner, et A. A. Demkov, « Electronic and optical properties of NbO₂ », *J. Appl. Phys.*, vol. 116, n° 21, p. 213705, déc. 2014.
- [40] N. Feldberg *et al.*, « Growth, disorder, and physical properties of ZnSnN₂ », *Appl. Phys. Lett.*, vol. 103, n° 4, p. 042109, juill. 2013.
- [41] T. Wang, C. Ni, et A. Janotti, « Band alignment and p-type doping of ZnSnN₂ », *Phys. Rev. B*, vol. 95, n° 20, p. 205205, mai 2017.
- [42] P. Narang *et al.*, « Bandgap Tunability in Zn(Sn,Ge)N₂ Semiconductor Alloys », *Adv. Mater.*, vol. 26, n° 8, p. 1235-1241, févr. 2014.
- [43] A. Punya et W. R. L. Lambrecht, « Band offsets between ZnGeN₂, GaN, ZnO, and ZnSnN₂ and their potential impact for solar cells », *Phys. Rev. B*, vol. 88, n° 7, p. 075302, août 2013.
- [44] G. E. Jellison et F. A. Modine, « Parameterization of the optical functions of amorphous materials in the interband region », *Appl. Phys. Lett.*, vol. 69, n° 3, p. 371-373, juill. 1996.
- [45] R.M. Azzam, N.M. Bashara, *Ellipsometry and Polarized Light*, North Holland, Amsterdam, 1977. .
- [46] J. Tauc, R. Grigorovici, et A. Vancu, « Optical Properties and Electronic Structure of Amorphous Germanium », *Phys. Status Solidi B*, vol. 15, n° 2, p. 627-637.
- [47] G. E. Jellison et F. A. Modine, « Parameterization of the optical functions of amorphous materials in the interband region », *Appl. Phys. Lett.*, vol. 69, n° 3, p. 371-373, juill. 1996.
- [48] P. B. Barna et M. Adamik, « Growth mechanisms of polycrystalline thin films », in *Science and Technology of Thin Films*, 0 vol., WORLD SCIENTIFIC, 1995, p. 1-28.
- [49] F. Alnjiman *et al.*, « Chemical environment and functional properties of highly crystalline ZnSnN₂ thin films deposited by reactive sputtering at room temperature », *Sol. Energy Mater. Sol. Cells*, vol. 182, p. 30-36, août 2018.

Chapter 4 Microstructure and tuning the structure of ZnSnN₂ thin films	91
4.1 Focus on the structure of ZnSnN₂	91
4.1.1 Orthorhombic, monoclinic or hexagonal structures.....	91
4.1.2 Monoclinic vs orthorhombic.....	92
4.1.3 Monoclinic versus hexagonal phases.....	95
4.2 Tuning the structure of ZnSnN₂	98
4.2.1 Tuning the structure with the stoichiometry	98
4.2.2 Tuning the structure by changing the pressure	103
4.2.2.1 Tuning the structure with the working pressure	103
4.2.2.2 Tuning the structure by changing the pressure by controlling the stoichiometry	108
4.3 Conclusion	113
References.....	117

Chapter 4 Microstructure and tuning the structure of ZnSnN₂ thin films

This chapter is divided in two main parts. In the first one, a discussion about the structure of as-deposited films is presented. This discussion is based on results obtained by transmission electron microscopy and electron diffraction results. In the second part, we study influence of the growth parameters on the material properties. The influence of the stoichiometry on the structure and the electrical and optical properties of ZnSnN₂ thin films is probed. The Mossbauer spectrometry is used for tin element yielding to pull out chemical information.

4.1 Focus on the structure of ZnSnN₂

4.1.1 Orthorhombic, monoclinic or hexagonal structures

We begin this section by describing the main reported structures for ZnSnN₂. According to the literature data, ZnSnN₂ may crystallize in several structures (as mentioned in chapter 1): orthorhombic Pna2₁, orthorhombic Pmc2₁, hexagonal P6₃mc, or monoclinic P2₁. It is hard to determine the structure and the lattice parameter by XRD due to the preferred orientation of our sputtered films (see section 3.2.3). By TEM it was also difficult to distinguish the structure, due to the possibility to index the electron diffraction patterns with the four structures. The electron diffraction patterns in figure 4.1 show the possibility to index the patterns with different structures.

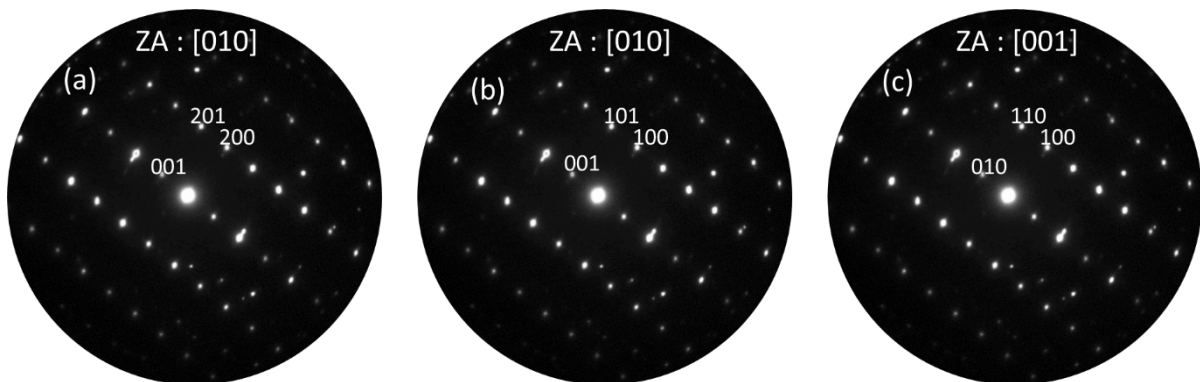


Figure 4.1 Electron diffraction pattern of ZnSnN₂ thin film. (a) indexed with orthorhombic Pna2₁ in zone axis is [010], (b) indexed with hexagonal P6₃mc in zone axis is [010], (c) indexed with monoclinic P2₁ in zone axis [001].

4.1.2 Monoclinic vs orthorhombic

For ZnSnN_2 it is challenging to determine the structure. Although it is a hard task to describe the film structure without any doubt, in the present section we show how to exclude the orthorhombic structure. Figure 4.2 shows the electron diffractions pattern simulation of two possible structures: figure 4.2 (a) for the orthorhombic and figure 4.2 (b) for monoclinic. This figure clearly evidences that TEM seems a powerful method to distinguish the orthorhombic structure and the monoclinic one. Indeed, some diffraction spots are forbidden in the $[010]$ direction of the monoclinic structure compared to the orthorhombic one. Usually, we perform TEM characterization on cross section thin foil. However, due to the possible occurrence of several columns along the thin foil cross section, the diffraction patterns may contain the signal coming from several non-oriented columns in the plane. To overcome this problem, we have chosen to do the measurement on a thin foil parallel to the film surface. It was a very hard task to prepared such a sample using focused ion beam.

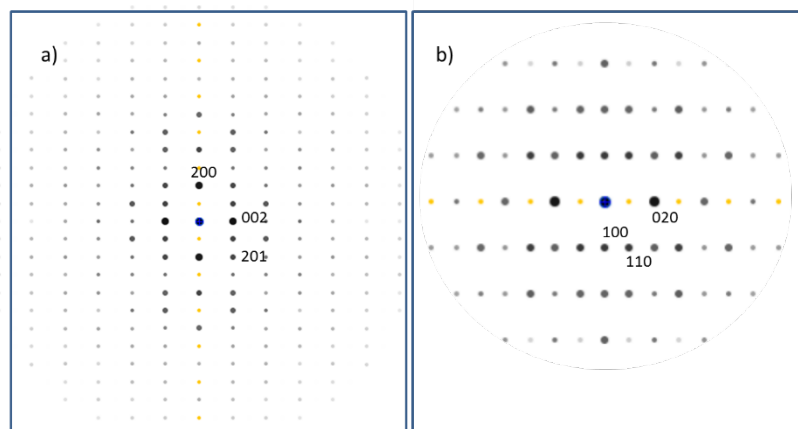


Figure 4.2 (a) Electron diffraction pattern simulation for orthorhombic structure $Pna2_1$ in zone axis $[010]$. (b) Electron diffraction pattern simulation for monoclinic structure $P2_1$ in zone axis $[001]$.

The main idea for the top view preparation was to see the direction of growth that was not accessible with the lamella cross section. Figure 4.3 shows the selected area electron diffraction (SAED) patterns of zinc tin nitride thin film from lamella top view. The SAED pattern shows diffraction rings characteristic of polycrystalline thin film. Both images are the same except the right image where we add interplanar distance values.

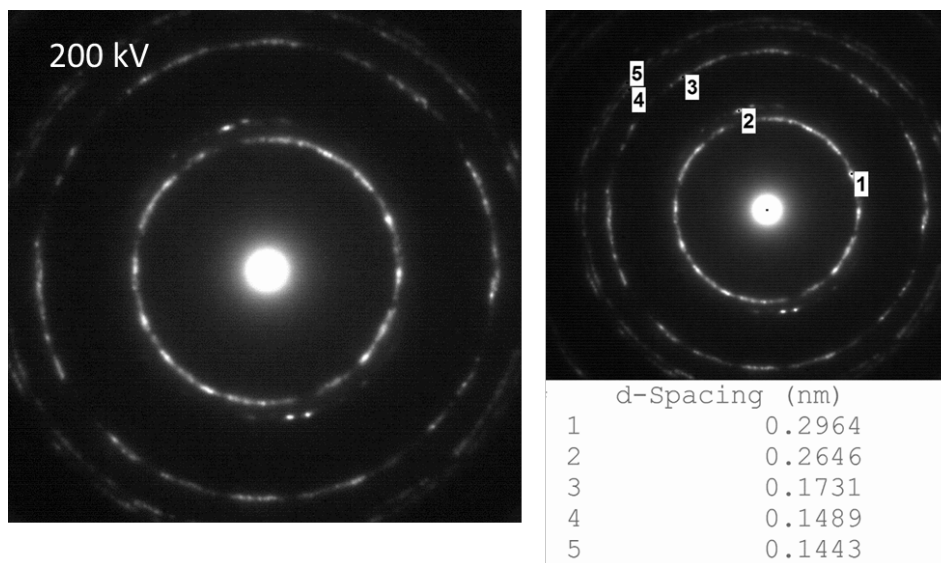
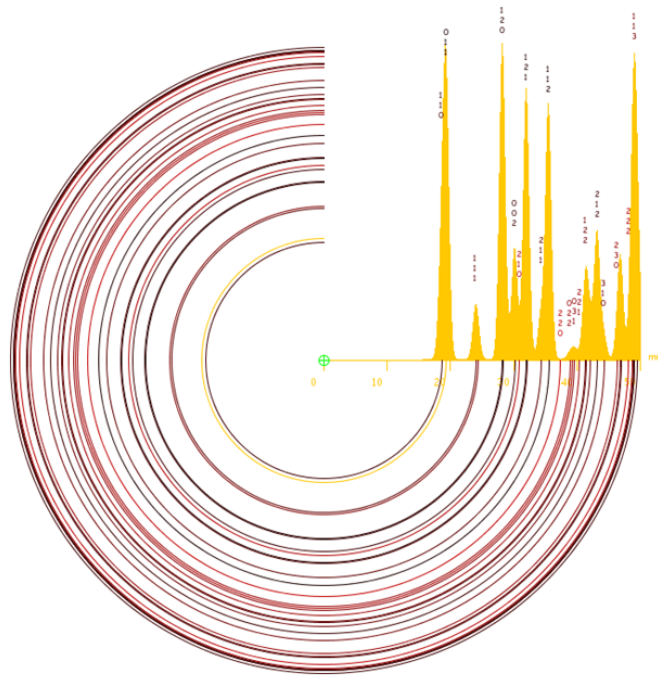


Figure 4. 3 selected area electron diffraction pattern of zinc tin nitride thin film from lamella top view. The selected area electron diffraction pattern showing diffraction rings. Right image with *d* values.

After we obtain the diffraction ring pattern, we have to do a simulation for the structure of the film. Figure 4.4 and figure 4.5 show the simulation by (JEMS electron microscopy simulation software) for the diffraction ring of ZnSnN_2 with two structures: orthorhombic and monoclinic. The image also contains the table of the indices of diffraction (h,k,l), the distances between the planes and the intensity of the peaks.

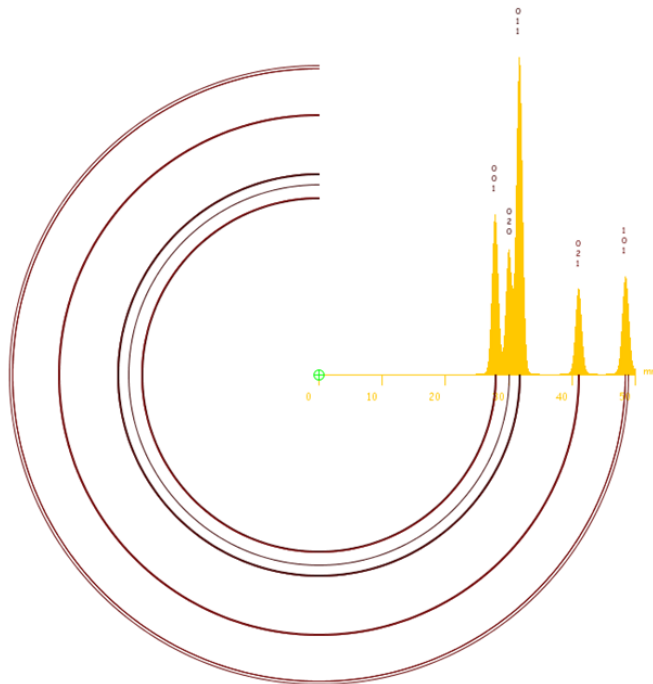
Crystal : ZnSnN2 Ortho Pna21 new



Camera length / mm : 3315
Accelerating voltage / kV : 200.0

Figure 4.4 Simulation of diffraction ring pattern of ZnSnN₂ with orthorhombic structure Pna2₁.

Crystal : ZnSnN2 Mono P21 new



Camera length / mm : 3315
Accelerating voltage / kV : 200.0

Figure 4.5 Simulation of diffraction ring pattern of $ZnSnN_2$ with monoclinic structure $P2_1$.

However, figure 4.6 shows the half part of the experimental electron diffraction pattern and also half of the simulated one. In figure 4.6 the electron ring pattern is compared to the (a) monoclinic and (b) to the orthorhombic structure. In the figure 4.6 (b) with the orthorhombic structure is clearly observed with many missing diffraction rings in the TEM image. On the other hand for the monoclinic phase only one ring is missing. This is one of our main argument to eliminate the orthorhombic phase for the $ZnSnN_2$ structure. It is a major result.

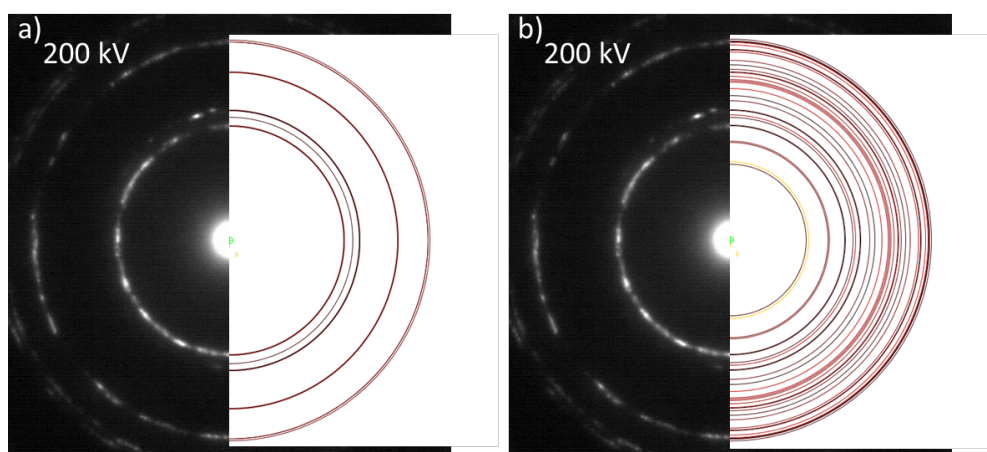


Figure 4.6 (a) Electron diffraction ring pattern with simulation ring for monoclinic structure. (b) Electron diffraction ring pattern with simulation ring for orthorhombic structure.

4.1.3 Monoclinic versus hexagonal phases

Before starting to compare and study these two structures, it must be noted that the problem was the small difference between these two structures. N. Feldberg *et al.* [1] obtained a monoclinic structure with lattice parameter $a = 3.395 \text{ \AA}$, $b = 3.400 \text{ \AA}$, $c = 5.534 \text{ \AA}$, $\alpha = 89.885^\circ$, $\beta = 90.033^\circ$, $\gamma = 120.036^\circ$. These parameters are close to the hexagonal structure. In figure 4.7 are shown the electron diffraction ring pattern with simulation ring (a) for monoclinic and (b) for hexagonal structure. The image reveals the difficulty to distinguish the differences between the two structures.

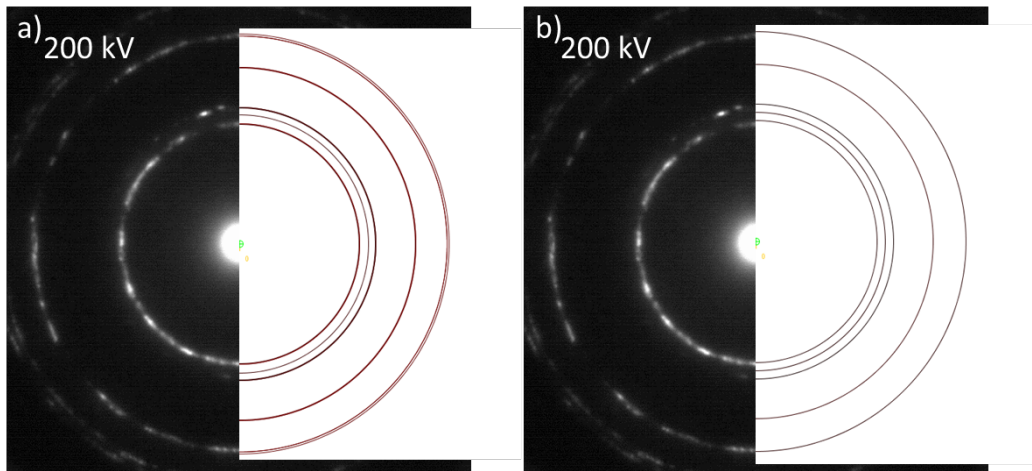


Figure 4.7 (a) Electron diffraction ring pattern with simulation ring for monoclinic structure. (b) Electron diffraction ring pattern with simulation ring for hexagonal structure.

Therefore, the SAED method does not seem to be effective or accurate enough to choose between the monoclinic and the hexagonal structure. Another method is to use the microdiffraction on tilted samples to observe different axis zone. Figure 4.8 shows the microdiffraction pattern of a zinc tin nitride thin film with (a) the experimental microdiffraction pattern, (b) the simulated microdiffraction pattern with monoclinic $P2_1$ in zone axis $[-101]$, (c) for the simulated monoclinic $P2_1$ pattern along the zone axis $[-101]$. In the simulation figure 4.8 (b,c) two reflections $(-1-1-1)$ and $(-11-1)$ are missing in the figure 4.8 (a). As seen in both the simulation (figure 4.8 (b)) and the (figure 4.8 (c)) there are two missing reflections labeled $(\bar{1}\bar{1}\bar{1})$ and $(\bar{1}1\bar{1})$ (blue arrows blue in the figure).

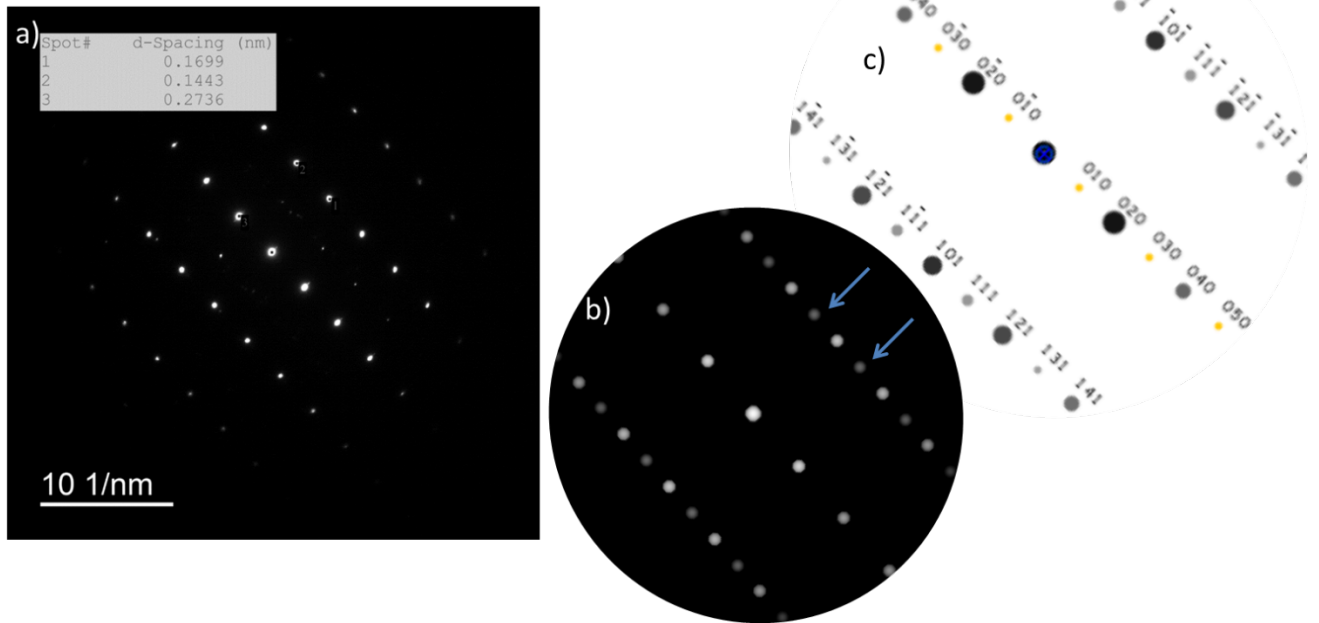


Figure 4.8 Microdiffraction pattern of the zinc tin nitride thin film, (b) simulation of microdiffraction pattern with monoclinic $P2_1$ in zone axis $[-101]$, (c) indexation for monoclinic $P2_1$ in zone axis $[-101]$.

Figure 4.9 shows the microdiffraction of the zinc tin nitride thin film. Where (a) is the microdiffraction pattern experimental $[10\bar{1}0]$, (b) indicated for hexagonal $P6_3mc$ in zone axis $[210]$, (c) simulation of microdiffraction pattern. For the hexagonal structure, all the reflection patterns are visible. This means that the calculated hexagonal structure can be compatible with the experiments. Finally, we can say that $ZnSnN_2$ thin film has a hexagonal structure with group space $P6_3mc$. However, these TEM studies does not allow the determine the space group of our films.

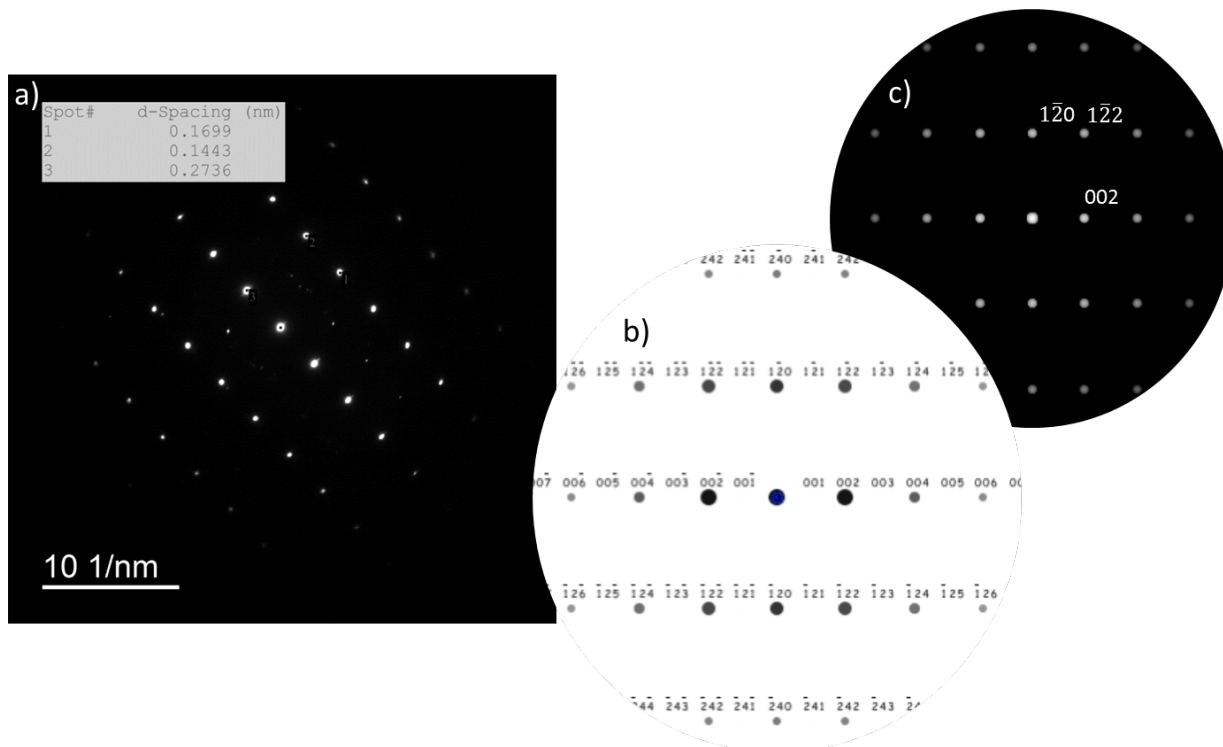


Figure 4.9 Microdiffraction pattern of the zinc tin nitride thin film, (b) indicated for hexagonal $P6_3mc$ in zone axis $[210]$, (c) simulation of microdiffraction pattern with monoclinic $P6_3mc$ in zone axis $[210]$.

4.2 Tuning the structure of $ZnSnN_2$

The properties of materials strongly depend on their structure, composition and microstructure. This section is devoted to the effect of the deposition parameters (target voltage and total pressure) on the thin film composition and structure. The realization of devices requires a good control of it together with the possibility to tune the fundamental properties of the material such as bandgap energy, doping, crystallography, etc...

4.2.1 Tuning the structure with the stoichiometry

The growth of stoichiometric $ZnSnN_2$ thin films has been achieved and described in chapter 3. In this chapter, we will describe how to tune the stoichiometry in $ZnSnN_2$ thin films. The approach will be to vary the discharge voltage ratio of the zinc and tin target. The discharge voltage for zinc target lies in the -220 to -280 V range. For the tin target, the discharge voltage was within the -450 and -480 V range. In Figure 4.10 are reported the atomic contents of Zn

and Sn in ZnSnN₂ thin films as a function of the ratio of the discharge voltage applied to the zinc and tin targets.

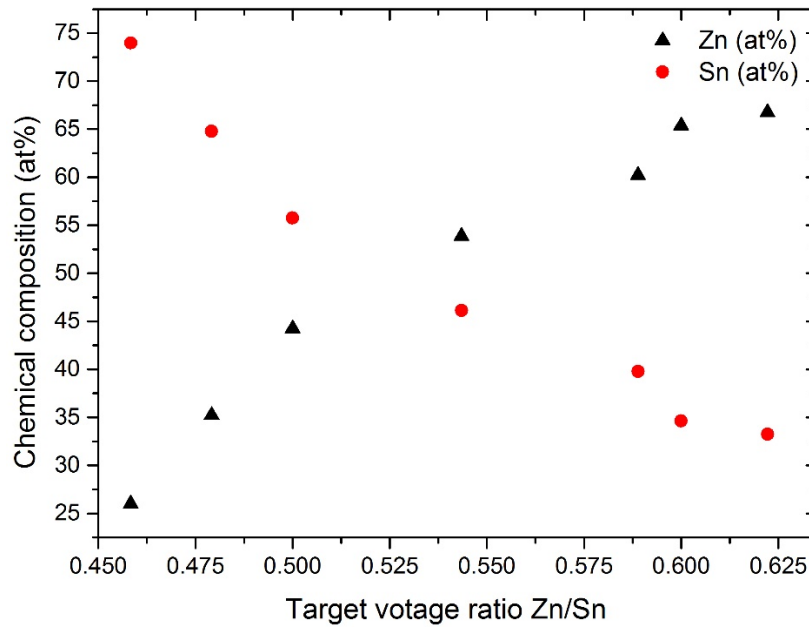


Figure 4.10 composition of ZnSnN₂ thin films as a function of the Zn/Sn voltages applied on the targets.

The growth of ZnSnN₂ with seven different stoichiometries has been achieved. The electrical parameters and film composition are shown in table (table 4.1). The atomic ratio is $r = \frac{Zn}{(Zn+Sn)}$ (at%). The target voltage ratio is a powerful parameter to tune the film atomic ratio from 0.26 to 0.67. Thus, using this parameter it is possible to deposit films with a wide range of compositions. Since the nitrogen content was not measured, we suppose that its concentration is in agreement with stoichiometric materials.

Table 4.1 Electrical parameters and composition of ZnSnN₂ thin films.

Zn (V)	Sn (V)	Zn/Sn	Zn (at.%)	Sn (at.%)	Zn/(Zn+Sn)
-220	-480	0.45	26.0	74.0	0.26
-230	-480	0.47	35.2	64.8	0.35
-240	-480	0.5	44.3	55.7	0.44
-250	-460	0.54	53.9	46.1	0.54
-265	-450	0.58	60.2	39.8	0.60
-270	-450	0.6	65.4	34.6	0.65
-280	-450	0.62	66.8	33.2	0.67

Figure 4.11 shows the X-ray diffractograms of ZnSnN_2 thin films grown with different Zn and Sn target voltages. The chemical composition and the Zn/Sn ratio have real impact on the structure and the properties of the films. ZnSnN_2 films with ratio of 0.26 exhibit an X-ray amorphous structure. Such a point is not surprising. S. Choi et al. [2] showed that by growing tin nitride thin films by reactive radio frequency magnetron sputtering, the diffractogram of tin nitride thin film was amorphous. For higher values of the Zn/Sn ratio, the as-deposited films are crystallized. However, as discussed in the previous chapter it is hard to determine the film structure from these X-ray diffractograms. Then, we use the conclusion of the section 4.1.3 by considering that the films deposited in the present chapter exhibit a hexagonal structure. When the Zn/Sn ratio is increased from 0.26 to 0.35 or 0.44 the (100), (101) and (110) diffraction peaks of the hexagonal structure of ZnSnN_2 appear.

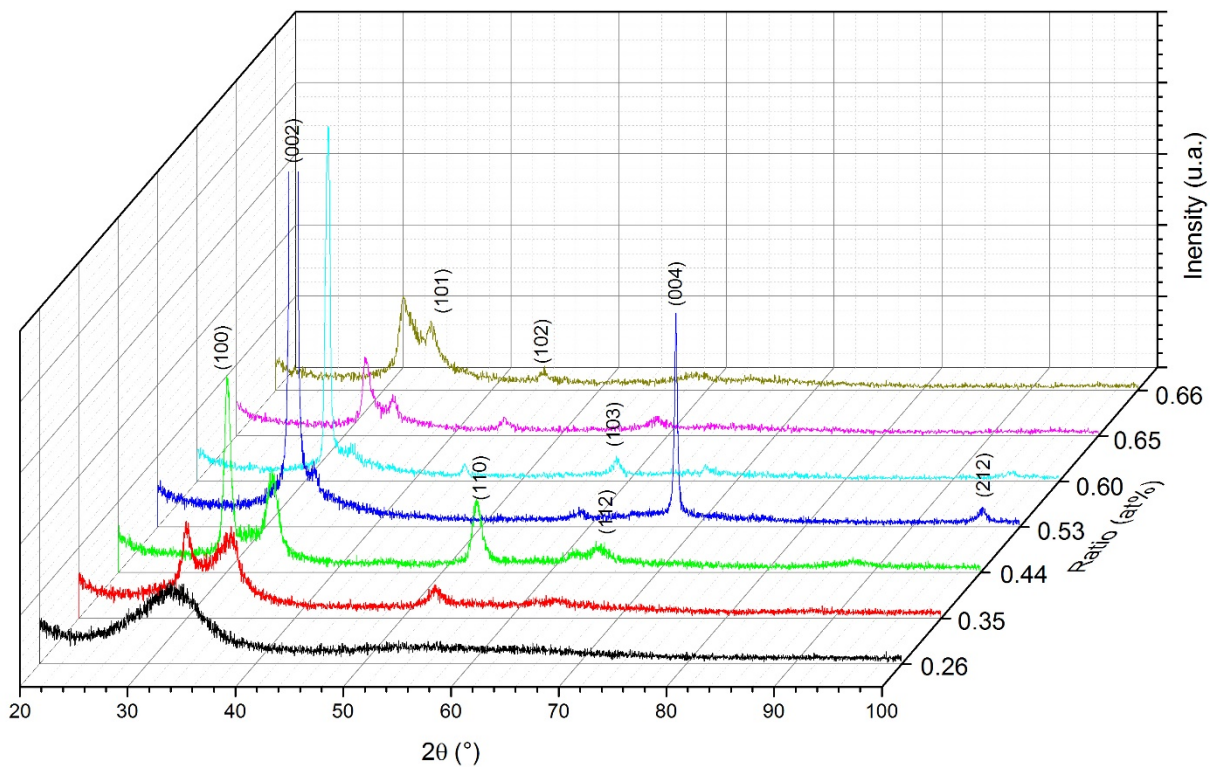


Figure 4.11 X-ray diffractograms of ZnSnN_2 thin films with different atomic Zn/Sn ratios. The indexations correspond to the hexagonal structure type ($P6_3mc$) with $a = 0.341 \text{ nm}$ and $c = 0.551 \text{ nm}$

The sample with ratio 0.53 has the same structure than that we mention in chapter 3. The diffractogram shows that the films grow with a highly preferred orientation along the [001] direction (c axis) with two clear peaks corresponding to the (002) and (004) planes. By

increasing the Zn/Sn ratio (0.60) the intensity of the (002) and (004) peaks decrease and the peak shift may be due the stress.

Finally, the zinc rich samples (ratio of 0.65 and 0.66) clearly lose the preferred orientation. We should notice that the peak (101) peak also appear and increases maybe due to the formation of Zn_3N_2 phase. We have grown Zn_3N_2 to test that hypothesis Zn_3N_2 thin films have been deposited at room temperature on glass by reactive sputtering. Figure 4.12 shows the X-ray diffractogram of the obtained films. This diffractogram only contains two main peaks (at approximately 2θ values of 31.5 and 34.0°). According to literature [3]–[6], Zn_3N_2 may crystallize in a cubic structure (Ia_3) where the (321) peak) is mainly visible. It is peak located at the same positions as the (101) $ZnSnN_2$ (34.0°). The increase of the (101) peak in the sample with $r = 0.66$ in $ZnSnN_2$ is due to the formation of Zn_3N_2 .

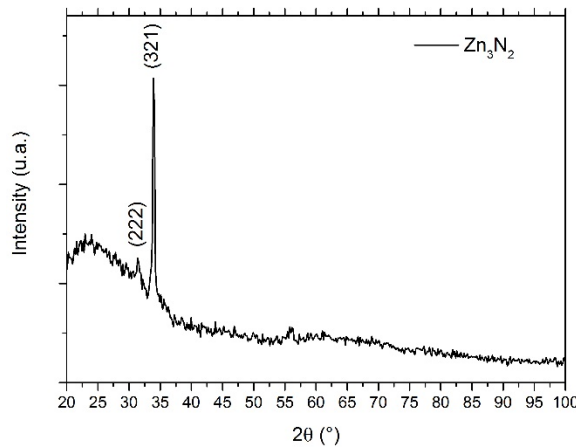


Figure 4.12 X-ray diffractograms of zinc nitride thin film. The indexations correspond to the cubic structure type (Ia_3) with $a = 0.981$ nm.

The optical band gap and optical absorption of $ZnSnN_2$ films have been studied with different stoichiometries by UV-visible spectroscopy. Figure 4.13 shows the transmission spectra of $ZnSnN_2$ thin films with different ratios r . Samples with r values of 0.44 and 0.53 are really similar to the previous spectra reported in chapter 3 and in [7]. The films are transparent in the NIR region about (25% - 40% in the wavelength 800 to 2500 nm). The transmittance decreases then partially above 1500 nm. This phenomenon is known to be present in transparent conductive oxides with high carrier concentrations [8] [9]. Such a phenomenon is not visible in samples with ratio of 0.26. 0.35. 0.60. 0.65 and 0.66. The transmittance is stable within the 1250 to 3000 nm range. The films also present prominent interference fringes caused by the multiple reflections at the three interfaces: air / $ZnSnN_2$ / glass substrate.

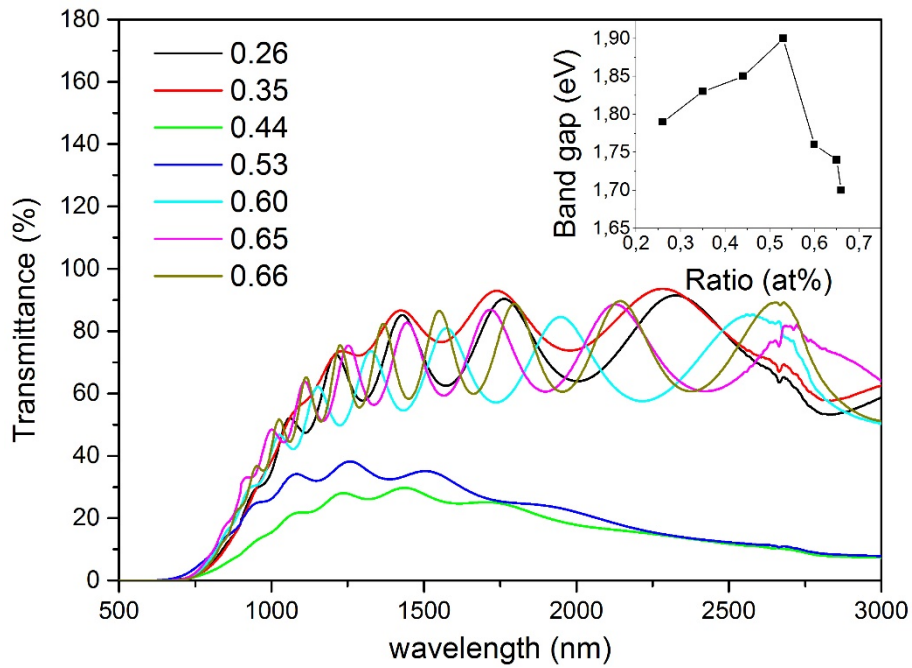


Figure 4.13 : Transmission spectra of ZnSnN₂ thin films of different ratio r . The inset is the optical band gap in function of the atomic ratio Zn / Sn.

The inset in figure 4.13 shows the optical band gaps of the samples as a function of the atomic ratio with a band gap determined by the Tauc plot method. The values of the band gap energy values ranges from 1.7 eV to 1.9 eV. The sample with $r = 0.66$ as the lowest band gap with value around 1.7 eV. The band gap increases by increasing the Sn atomic percentage until reaching a maximum with the sample with $r = 0.53$. Then, the band gap decreases for higher values of the atomic ratio. The interpretation is a little bit tricky as the different of the band gap could be related with cation disorder in the alloy and the lattice structure [9] [10].

The electrical resistivity of ZnSnN₂ thin film grown with different stoichiometries is measured by the four-point probe method (figure 4.14). The value of electrical resistivity at room temperature is low for the stoichiometric films and rich tin samples. This is normal for the ZnSnN₂ stoichiometric as we mentioned in chapter 3.

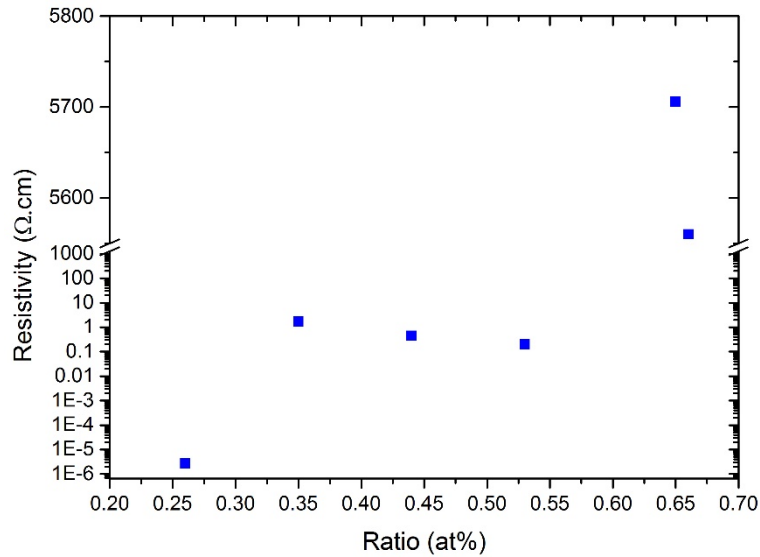


Figure 4.14 The electrical resistivity of $ZnSnN_2$ thin film grown with different stoichiometry ratio (at%).

The tin rich sample electrical behaviour is not a surprise. Inoue et al. [12] obtained a resistivity value around 10^{-1} to 10^{-2} Ωcm . For the zinc-rich samples, the resistivity increases with the atomic zinc content. The result was not expected because in literature Fatsuhara et al. [6] obtained an resistivity electrical around 10^{-2} to 10^{-3} Ωcm for zinc nitride thin films. For $ZnSnN_2$ thin films Fioretti et al [13] obtained similar evaluation of the electrical conductivity in function of the stoichiometric. Where the electrical conductivity is the invert of the electrical resistivity.

4.2.2 Tuning the structure by changing the pressure

4.2.2.1 Tuning the structure with the working pressure

The growth parameters were tuned to better understand the system and to improve the propriety of the material. In this part, $ZnSnN_2$ have been grown by changing the total working pressure. The discharge voltage was set at -250 V and -450 V for zinc and tin, respectively. The N_2 flow rate is set at 60 sccm. The total pressure was varied between 0.5 Pa to 3.0 Pa (see table 4.2).

Table 4.2 Electrical parameters and film compositions of ZnSnN₂ grown with different pressures.

Name	Pressure (Pa)	Zn voltage (V)	Sn voltage (V)	Zn (at.%)	Sn (at.%)	Zn/(Zn+Sn)	Thickness (μm)
ZSN-133	0.5	-250	-450	33	67	0.33	0.8
ZSN-132	1	-250	-450	50	50	0.5	1.2
ZSN-134	2	-250	-450	53	47	0.53	2.1
ZSN-135	3	-250	-450	53	47	0.53	2.1

Figure 4.15 shows that the atomic concentration of the two metallic elements is not stable with the pressure. By setting the discharge voltage applied to the targets was not enough to control the stoichiometry of the elements. The pressure seems to have a large influence on the stoichiometry. The influence is remarkable for the pressure of 0.5 Pa where the atomic content of Zn decreases from 50 at. % at 1 Pa to 33 at. % with 0.5 Pa. Such an effect may be related to the emission law of the sputtered atoms and/or to their transfer into the gas phase.

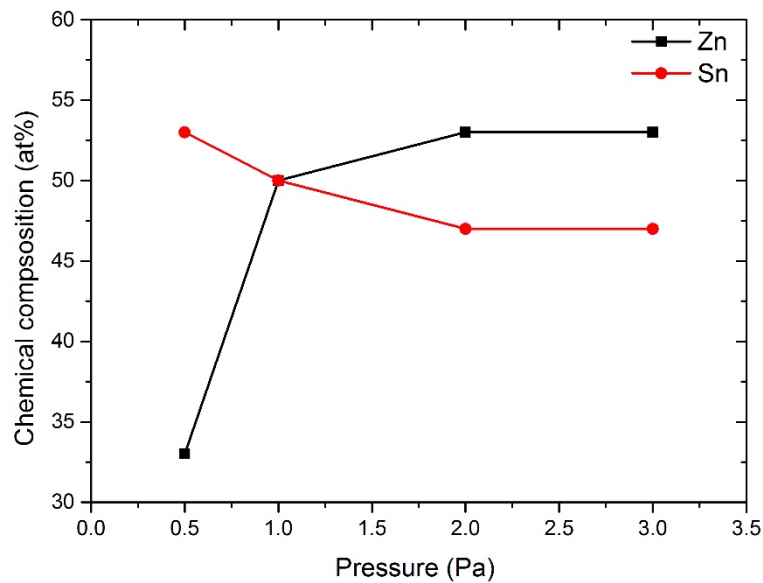


Figure 4.15 Atomic percentage of Zn (black) and Sn percentage (red) as a function of pressure.

Figure 4.16 shows the X-ray diffractograms of ZnSnN₂ grown at (0.5, 1.0, 2.0, and 3.0) Pa total pressure with fixing the discharge voltage applied to the zinc and tin targets. The influence of total pressure was clearly appearing in structure of the films. Depending on the total pressure, the texture of the film can be tuned. At 0.5 Pa the film is crystallized with small grains with two major peaks at (100) and (101) for the hexagonal structure P6₃mc. ZnSnN₂

grown with a total pressure of 1.0 Pa have the same structure those mentioned in chapter 3. The diffractogram shows that the ZnSnN_2 film grows with a strong preferred orientation along the [001] direction. Where these two peaks determined as (002) and (004) for the hexagonal structure. By increasing the total pressure of growth for 2.0 Pa the intensity of the peak (002) decreases and the preferred orientation disappears where several peaks appear in the diffractogram.

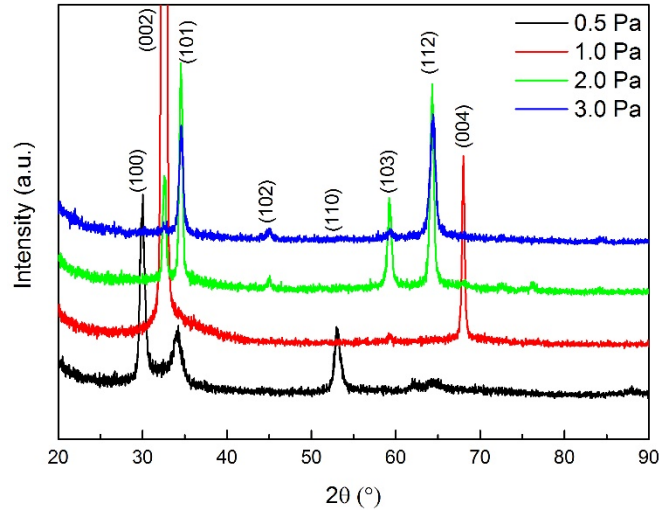


Figure 4.16 : X-ray diffractograms of ZnSnN_2 thin films with different growth pressures. The indexations correspond to the hexagonal structure ($P6_3mc$).

ZnSnN_2 grown at 3.0 Pa have the same preferred orientations than films grown at 2.0 Pa, the main difference being the peak intensity decrease. We may note that by changing the pressure all the existing peaks correspond the hexagonal structure $P6_3mc$.

As mentioned before, Mossbauer spectrometry is very powerful to obtain information about the chemical environment of tin atoms. Figure. 4.17 shows the ^{119}Sn Mossbauer spectra of the ZnSnN_2 recorded at 300 K grown with different pressure (0.5, 1.0, 2.0, 3.0) Pascal. A summary of the Mossbauer parameters are given in Table 4.3. They also are reported in Figure 4.18. As well, the experimental curves are fitted using two contributions for Sn^{+4} in two peaks. This is not easy to interpret but suggests two distinct sites for Sn^{+4} in the as-deposited films.

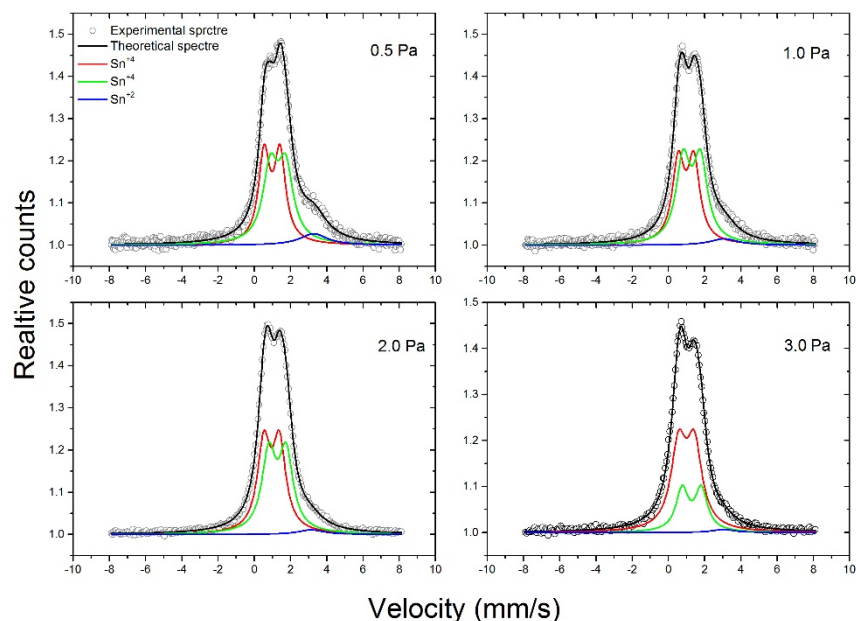


Figure 4.17 : Experimental and simulated ^{119}Sn Mossbauer spectra of ZnSnN_2 growth with different pressures.

For ZnSnN_2 films grown at 0.5 Pa the main contribution exhibits an isomeric shift (IS) of (0.98 and 1.3) mm/s and a quadrupolar splitting (QS) of (0.89 and 0.84) mm/s that are characteristic of Sn^{4+} ions in tetrahedral configuration while the second one with IS=3.27 mm/s is related to Sn^{2+} ions. The values of IS and QS slightly evolves as a function of the total pressure indicating that the structural changes evidenced by XRD do not induce a strong modification of the tin chemical environment of this film series. However, among the Sn^{4+} contributions the one observed at low IS become more present in the high pressure films. Such a result suggests that the high pressure favors one kind of Sn^{4+} position in the film structure. On the other hand, the contribution of Sn^{4+} ions and Sn^{2+} was varied with the pressure (Table 4.3). The Sn^{2+} contribution decreases from 13.7 to 2.7 % when the total pressures increases from 0.5 to 3.0 Pa. As discussed in chapter 3, this Sn^{2+} contribution results from the occurrence of tin – oxygen bonds. Thus, the increase of the total pressure induces a decrease of the oxygen contamination. Such a result seems surprising since less dense films are expected at high total pressure (most of the oxygen contamination being evidenced at the column boundaries).

Table 4.3 Hyperfine parameters of a ZnSnN₂ film growth with different pressures (Isomeric Shift and Quadripolar Splitting) and ratio of the two components.

Pressure (Pa)	Site	IS (mm/s)	QS (mm/s)	larger (mm/s)	%
0.5	Sn ⁺⁴	0.98	0.89	0.74	34.6
	Sn ⁺⁴	1.3	0.84	1	51.7
	Sn ⁺²	3.27		1.83	13.7
1	Sn ⁺⁴	0.97	0.86	0.81	38.7
	Sn ⁺⁴	1.28	0.96	0.95	53.3
	Sn ⁺²	3.06		1.83	8
2	Sn ⁺⁴	0.95	0.86	0.86	46.5
	Sn ⁺⁴	1.27	0.95	0.94	48.7
	Sn ⁺²	3.13		1.69	4.8
3	Sn ⁺⁴	0.99	0.87	1.02	72.6
	Sn ⁺⁴	1.28	1.06	0.84	24.6
	Sn ⁺²	3.04		1.43	2.7

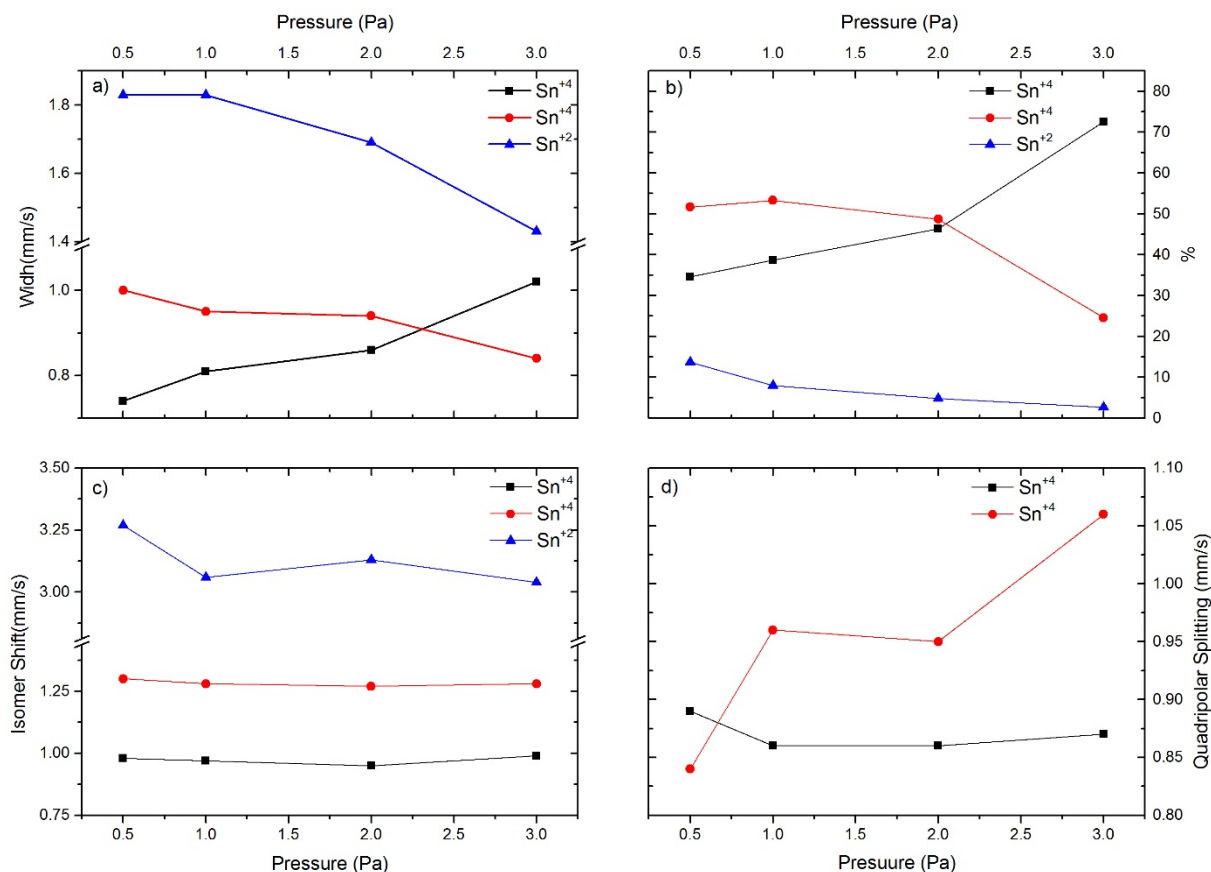


Figure 4.18 (a) The evolution of the larger of peaks of ZnSnN₂ thin films from Mossbauer spectra as a function of the pressure, (b) The evolution of the percentage of peaks of ZnSnN₂ thin films from Mossbauer spectra as a function of the pressure (c) The evolution of the Isomer shift of peaks of ZnSnN₂ thin films from Mossbauer spectra as a function of the pressure (d) The evolution of the Quadripolar splitting of peaks of ZnSnN₂ thin films from Mossbauer spectra as a function of the pressure.

4.2.2.2 Tuning the structure by changing the pressure by controlling the stoichiometry

In the previous section, we have shown that the evolution of the total pressure induces a change in the film composition. Thus, it is hard to distinguish from the previous results the effect of the sole total pressure to those of the film composition evolution. Thus, to bring information about the effect of the total pressure, it is necessary to adjust the film composition. In this part, ZnSnN₂ films have been grown at various total pressures but we also vary the discharge voltage to try to conserve the stoichiometry of the films. The discharge voltage was varied between -250 to -240 V for the zinc target and it was varied between -430 to -450 V for the tin. The flow rate of N₂ was fixed to a value 60 sccm. The total pressure was varied between (0.5, 1.0, 1.5,

2.0, 2.5 and 3.0) (see table (4.4)). We should note that ZnSnN₂ thin films grown with 0.5 Pa still are off stoichiometric with a ratio $\frac{Zn}{(Zn+Sn)}$ (at%) = 0.39.

Table 4.4 : Electrical parameters and composition of ZnSnN₂ grown with different pressures

Name	Pressure (Pa)	Zn voltage (V)	Sn voltage (V)	Zn (at.%)	Sn (at.%)	Zn/(Zn+Sn)	Thickness (μm)
ZSN-138	0.5	-250	-430	39	61	0.39	0.7
ZSN-137	1.0	-250	-450	48	52	0.48	1.3
ZSN-139	1.5	-245	-450	48	52	0.48	1.7
ZSN-140	2.0	-240	-450	47	53	0.47	1.7
ZSN-141	2.5	-240	-450	47	53	0.47	1.5
ZSN-142	3.0	-240	-450	47	53	0.47	1.5

Figure 4.19 shows the X-ray diffractograms of zinc tin nitride thin films grown at (0.5, 1.0, 1.5, 2.0, 2.5 and 3.0) Pa. The influence of total pressure was clearly observed in the structure of the films. Depending on the total pressure, the texture of the film is tuned. At 0.5 Pa the film is crystalized with small grains with four major peaks (100), (002), (101) and (110) for the hexagonal structure P6₃mc. As usual, ZnSnN₂ grown with total pressure 1.0 Pa have the same structure we mentioned in chapter 3. The diffractogram shows that the ZnSnN₂ films grown with a strong preferred orientation along the [001] direction. These two peaks at (002) and (004) correspond to the hexagonal structure. At 1.5 Pa the film has the same texture as with 1.0 Pa the only difference was the increase of the (101) and (103) peak intensity. By increasing the total pressure at 2.0, 2.5 or 3.0 Pa the intensity of the (002) peak decreases and the preferred orientation disappears while several additional peaks appear in the diffractogram.

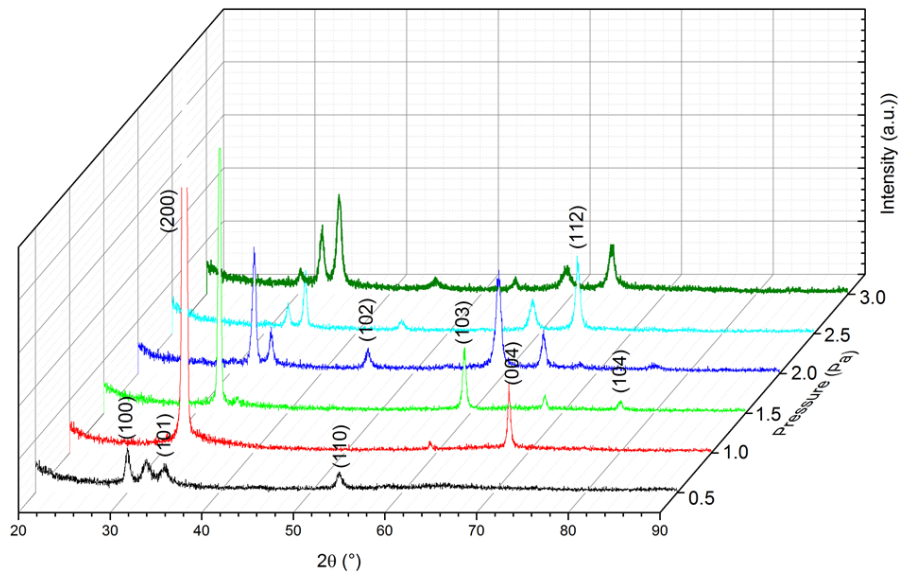


Figure 4.19 : X-ray diffractograms of zinc tin nitride thin films deposited at different total pressures. The indexations correspond to the hexagonal structure type ($P6_3mc$).

The microstructure of $ZnSnN_2$ thin films deposited with different pressures have been studied. Top-view SEM images of $ZnSnN_2$ thin films deposited at (0.5, 1.0, 1.5, 2.0, 2.5 and 3.0) Pa are shown in Figure. 4.20 (a), (b), (c), (d), (e) and 4.20 (f), respectively. As well for the structure, the influence of the total pressure was clearly appearing in microstructure in the films, which demonstrates clearly that the film grain size of film increases with the total pressure. The grain size estimated by the top-view SEM is presented in Table 4.7. Although the films have been deposited at high pressure (3 Pa), the SEM top view analysis does not evidence a high porosity. The increase of the deposition pressure also induces a change in the grain shape that may be related to the evolution of the film preferred orientation revealed by XRD.

Table 4.5 The grain size of $ZnSnN_2$ thin films evolution with the pressure.

Pressure (Pa)	Grain size range(nm)
0.5	40-57
1.0	69-76
1.5	69-77
2.0	92-125
2.5	100-113
3.0	87-106

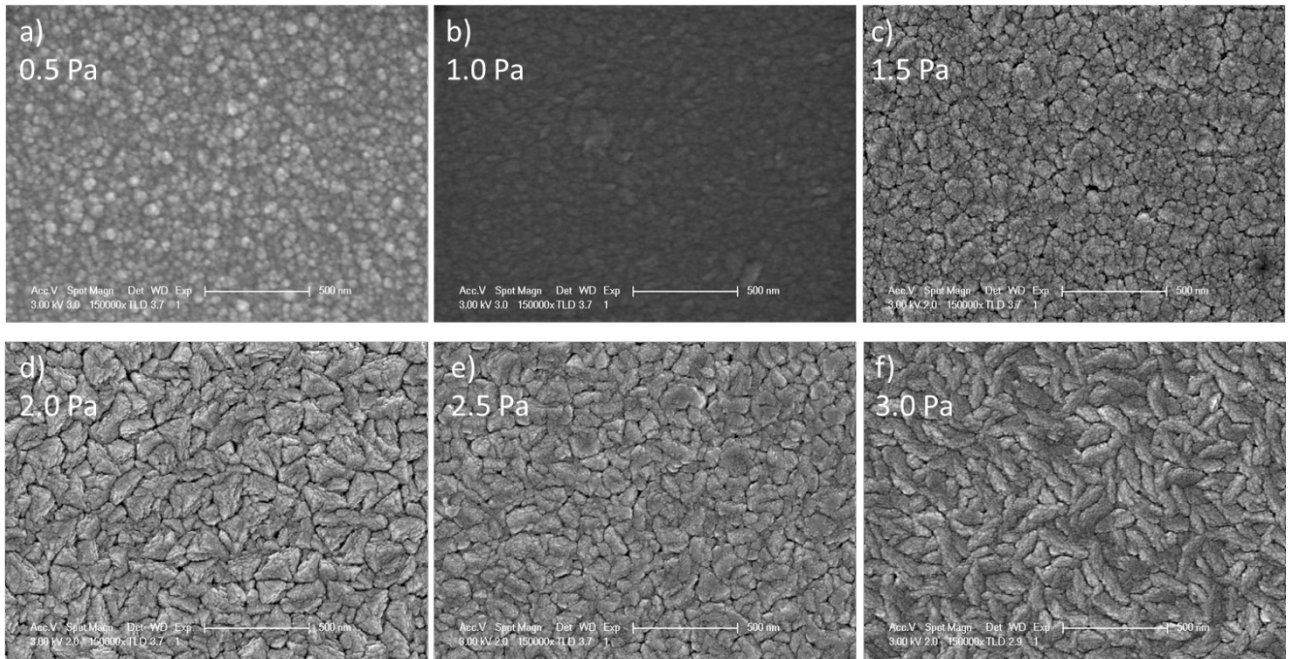


Figure 4.20 SEM images of $ZnSnN_2$ films grown with different pressures: (a) 0.5 Pa, (b) 1.0 Pa, (c) 1.5 Pa, (d) 2.0 Pa, (e) 2.5 Pa, and (f) 3.0 Pa.

The optical band gap and the optical absorption for $ZnSnN_2$ with different pressures by UV-visible spectroscopy have been determined. Figure 4.21 shows the transmission spectra of $ZnSnN_2$ thin films with different pressures. The sample grown at a total pressure of 1 Pa is similar to the spectra obtained in chapter 3 and presented in [7]. The film is transparent in the NIR region about (25% - 35%). The transmittance decreases partially above 1500 nm. All the films grown with different pressures have this same behavior. As mentioned before in (4.2.1) such a behavior appears in transparent conductors with high carrier concentrations [8] [9].

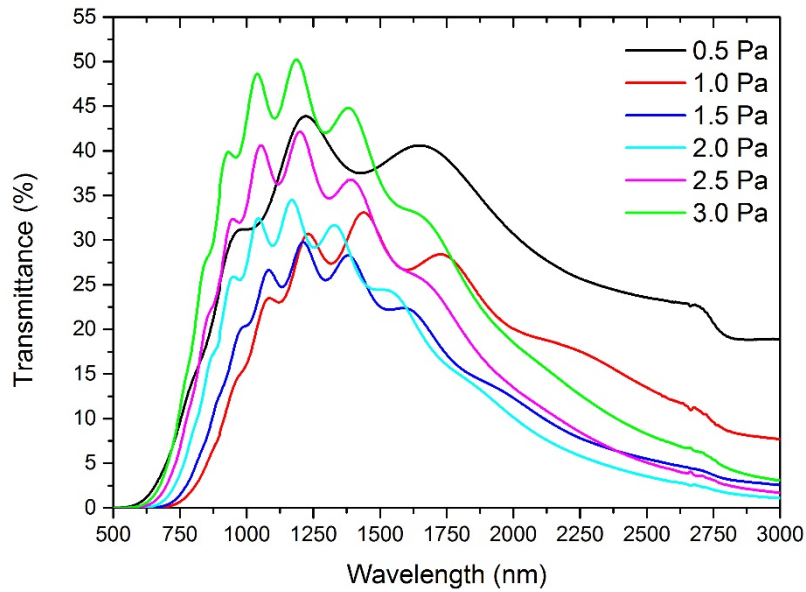


Figure 4.21: Transmission spectra of ZnSnN_2 thin films deposited with different pressures.

The band gaps were determined by using the Tauc plot method (see chapter 2). The values of the band gap range between 1.77 eV to 2.19 eV (table 4.6). The sample grown with 1.0 Pa has the lowest band gap with a value of 1.77 eV. By increasing the total pressure the band gap increases until obtaining the maximum with the sample at 3.0 Pa and its bandgap becomes 2.14 eV. We must note that the sample grown at 0.5 Pa has the highest value in this series of samples but we can exclude the reason linked to the off-stoichiometry of the sample.

In chapter 2 we mentioned the Urbach energy (Urbach energy E_U) in semiconductor materials with low crystallinity or amorphous materials due to localized states that extend in the optical band gap. As well, the Urbach energies have been determined for this series. We may exclude the value for the sample 0.5 Pa. ZnSnN_2 growth with 2.5 and 3.0 Pa have the highest values of Urbach energy where the minimum with 1.5 Pa.

Ellipsometry spectroscopy has been tried to confirm the UV-visible bandgap measurements. The values obtained with ellipsometry are shown in table 4.5. In figure 4.11 are shown the results obtained from UV-visible and ellipsometry spectroscopies. Figure 4.22 (a) presents the comparison between the optical band gaps obtain from UV-visible and ellipsometry spectra. For the optical band gaps the difference between the two values was in the range of error measurement, i.e. approx. 0.1 eV, except for two samples where the difference is higher than 0.2 and 0.3 eV for the samples deposited at 3 Pa and 0.5 Pa, respectively. Except for the sample deposited at 0.5 Pa (i.e., with another stoichiometry) both methods show a progressive enlargement of the band gap with the total pressure.

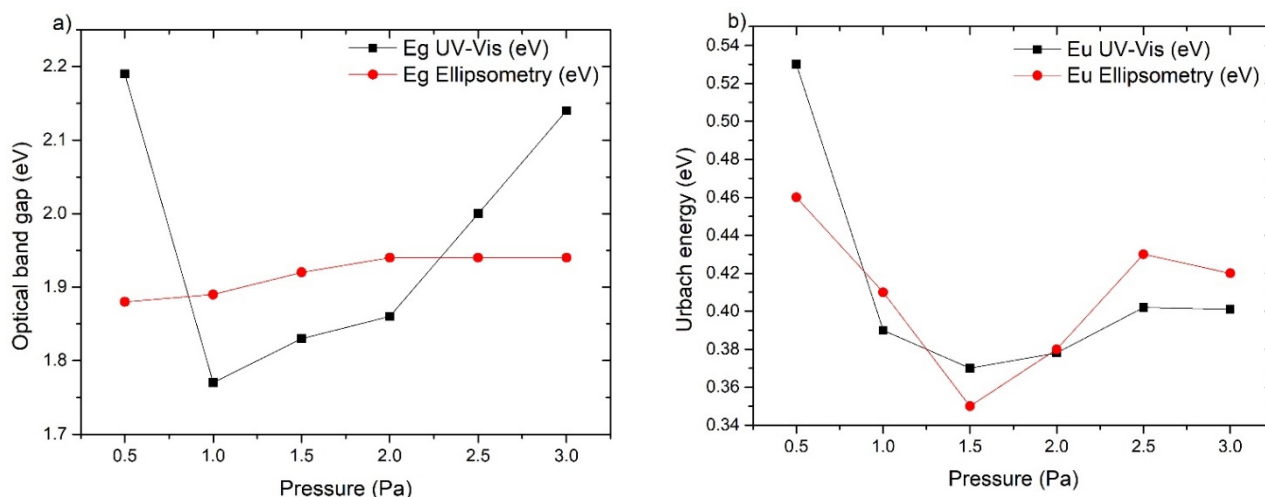


Figure 4.22 (a) Comparison between the optical band gaps obtain from UV-Vis and ellipsometry spectra, (b) comparison between the Urbach energies obtain from UV-Vis and ellipsometry spectra.

The figure 4.22 (b) shows the comparison between the Urbach energies obtain from UV-visible and ellipsometry spectra. For the Urbach energy the difference between the two values was in the range of error of measurement around 0.02 eV, except one value where the error more than 0.07 the sample 0.5 Pa. The evolution of the Urbach energy with the pressure was looking closely. A minimum of the Urbach energy at 1.5 Pa and maximum with 0.5 Pa which a good correlation with X-ray diffraction in function of the grain size.

Table 4.6 comparison between the optical band gaps and Urbach energy obtain from UV-visible and ellipsometry spectra for ZnSnN2 thin films growth with different pressures

Pressure (Pa)	Eg UV-Vis (eV)	Eg Ellipsometry (eV)	Eu UV-Vis (eV)	Eu Ellipsometry (eV)
0.5	2.19	1.88	0.53	0.46
1	1.77	1.89	0.39	0.41
1.5	1.83	1.92	0.37	0.35
2	1.86	1.94	0.378	0.38
2.5	2	1.94	0.402	0.43
3	2.14	1.94	0.401	0.42

The electrical resistivity of ZnSnN₂ thin films grown with different pressures have been measured using the four-point probe method. The value of electrical resistivity at room temperature tends to increase as a function of the pressure (Figure 4.23).

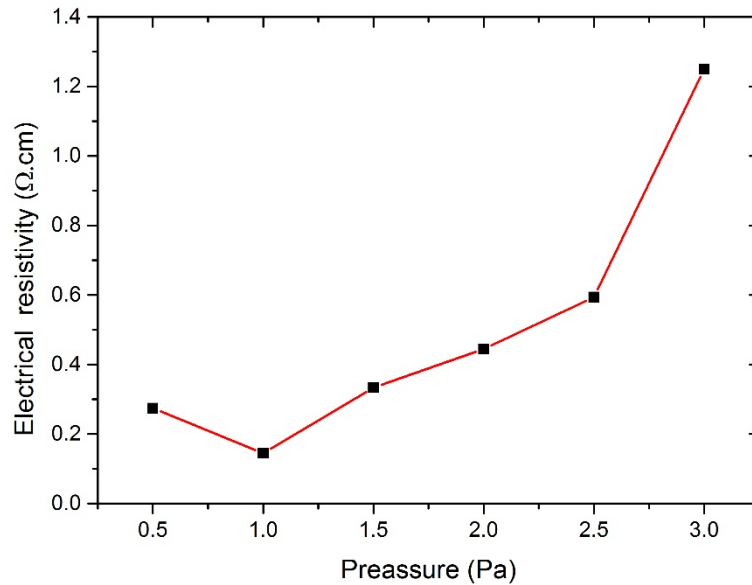


Figure 4.23 The evolution of the resistivity of ZnSnN₂ thin films as a function of the pressure.

The electron concentration of ZnSnN₂ thin film as a function of the total pressure is determined by Hall effect measurements (figure 4.24) and the values are reported in Table 4.7. The minimum value for the electron concentration was around $5.37 \times 10^{18} \pm 0.1 \text{ cm}^{-3}$ for the sample grown with a total pressure 1.5 Pa. While this sample give the highest value of electron mobility around $3.772 \text{ cm}^2 \text{ V}^{-1} \text{ s}^{-1}$. A minimum of the electron concentration is obtained at 1.5 Pa in a good correlation with Urbach energy mentionned before.

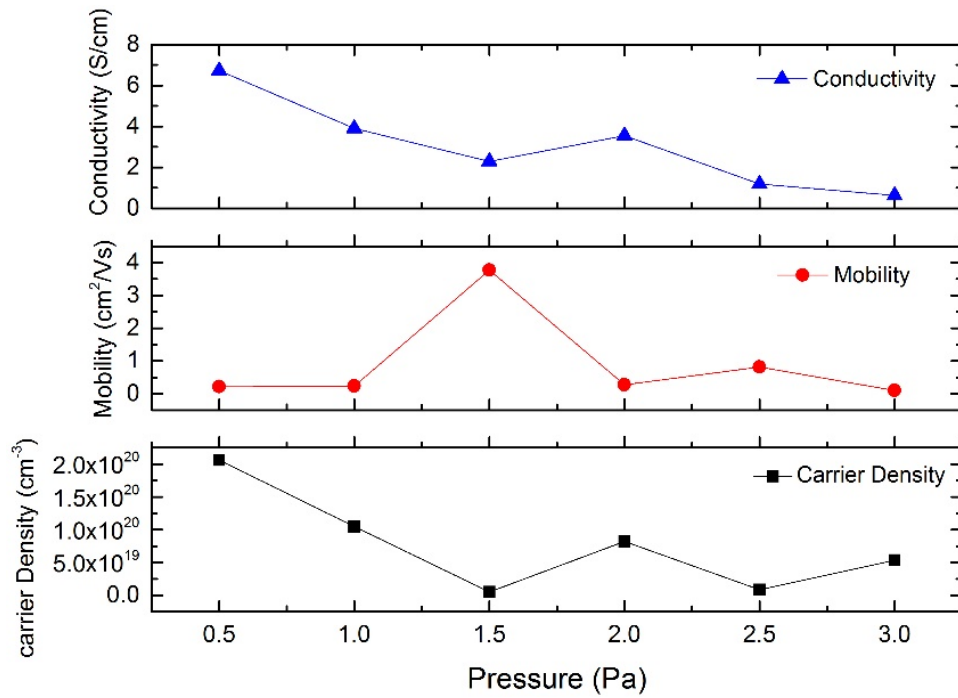


Figure 4.24 In black the evolution of the carrier density of ZnSnN₂ thin films as a function of the pressure, in red the evolution of the mobility of ZnSnN₂ thin films as a function of the pressure, in blue the evolution of the conductivity of ZnSnN₂ thin films as a function of the pressure.

Table 4.7 The values of the Hall effect measurements for ZnSnN₂ thin film growth with different pressure

Pressure (Pa)	Carrier Density (n-type. cm ⁻³)	Mobility (cm ² /Vs)	Conductivity (S/cm)
0.5	2.06x10 ⁺²⁰	0.217	6.72
1	1.05x10 ⁺²⁰	0.238	3.90
1.5	5.37x10 ⁺¹⁸	3.772	2.28
2	8.23x10 ⁺¹⁹	0.273	3.55
2.5	8.42x10 ⁺¹⁸	0.816	1.19
3	5.37x10 ⁺¹⁹	0.103	0.63

4.3 Conclusion

In the first part of this chapter, we have presented a discussion on the structure of ZnSnN₂ film. This relevant information has been obtained using electron diffraction. The results show that both monoclinic and orthorhombic structures can be excluded. Thus, our films crystallize in a hexagonal structure.

In the second part, we have shown the effect of changing the stoichiometric between zinc and tin element in ZnSnN_2 thin films. The growth of stoichiometric ZnSnN_2 thin films or off-stoichiometric ones can be used to tune the structure of the films. The optical band gap has been determined as a function of the stoichiometry. For the electrical resistivity, zinc tin nitride films showed a strong variation depending on their stoichiometry. In this part, we also study the effect of the total working pressure on the film properties. The total pressure was varied between 0.5 to 3.0 Pa. Optical absorption, electrical resistivity and Mössbauer spectroscopy have been employed to determine the physio-chemical properties of this study.

References

- [1] N. Feldberg *et al.*, « ZnSnN₂: A new earth-abundant element semiconductor for solar cells », in *2012 38th IEEE Photovoltaic Specialists Conference (PVSC)*, 2012, p. 002524-002527.
- [2] S. Choi, J. Kang, J. Park, et Y.-C. Kang, « Tin nitride thin films fabricated by reactive radio frequency magnetron sputtering at various nitrogen gas ratios », *Thin Solid Films*, vol. 571, Part 1, p. 84-89, nov. 2014.
- [3] W. S. Khan et C. Cao, « Synthesis, growth mechanism and optical characterization of zinc nitride hollow structures », *J. Cryst. Growth*, vol. 312, n° 11, p. 1838-1843, mai 2010.
- [4] Z. Fu-Jian *et al.*, « Thermal Decomposition Behaviour of Zn₃N₂ Powder », *Chin. Phys. Lett.*, vol. 22, n° 4, p. 907, 2005.
- [5] J. M. Khoshman *et al.*, « Growth and surface characterization of magnetron sputtered zinc nitride thin films », *Thin Solid Films*, vol. 520, n° 24, p. 7230-7235, oct. 2012.
- [6] M. Futsuhara, K. Yoshioka, et O. Takai, « Structural, electrical and optical properties of zinc nitride thin films prepared by reactive rf magnetron sputtering », *Thin Solid Films*, vol. 322, n° 1-2, p. 274-281, juin 1998.
- [7] F. Alnjiman *et al.*, « Chemical environment and functional properties of highly crystalline ZnSnN₂ thin films deposited by reactive sputtering at room temperature », *Sol. Energy Mater. Sol. Cells*, vol. 182, p. 30-36, août 2018.
- [8] M. D. Benoy, E. M. Mohammed, M. Suresh Babu, P. . Binu, et B. Pradeep, « Thickness dependence of the properties of indium tin oxide (ITO) FILMS prepared by activated reactive evaporation », *Braz. J. Phys.*, vol. 39, p. 629-632, 2009.
- [9] M. Mizuhashi, « Electrical properties of vacuum-deposited indium oxide and indium tin oxide films », *Thin Solid Films*, vol. 70, n° 1, p. 91-100, juill. 1980.
- [10] L. Lahourcade, N. C. Coronel, K. T. Delaney, S. K. Shukla, N. A. Spaldin, et H. A. Atwater, « Structural and Optoelectronic Characterization of RF Sputtered ZnSnN₂ », *Adv. Mater.*, vol. 25, n° 18, p. 2562-2566, mai 2013.
- [11] N. Feldberg *et al.*, « Growth, disorder, and physical properties of ZnSnN₂ », *Appl. Phys. Lett.*, vol. 103, n° 4, p. 042109, juill. 2013.
- [12] Y. Inoue, M. Nomiya, et O. Takai, « Physical properties of reactive sputtered tin-nitride thin films », *Vacuum*, vol. 51, n° 4, p. 673-676, déc. 1998.

[13] A. N. Fioretti *et al.*, « Combinatorial insights into doping control and transport properties of zinc tin nitride », *J. Mater. Chem. C*, vol. 3, n° 42, p. 11017-11028, oct. 2015.

General conclusions

In this work, ZnSnN₂ thin films have been synthesized by reactive magnetron sputtering. The films are potentially interesting for advanced optoelectronic realization such as solar cells or emitters. The structure, microstructure, chemical and physical properties have been studied. They are strongly influenced by experimental parameters.

The first chapter is dedicated to a bibliographic overview of the topic. We describe the issues of Earth abundant materials with respect to the scarcity of some elements. Then, we stressed the issue of the energy needs and more especially the question of the production of energy, the sun being then a real opportunity as a free source of incoming energy. The photovoltaic technologies are under development but the different approaches suffer from material or technological problems to be overcome to produce electricity through green technology, that is to say with cheap mass production possibilities and without scarce materials. We described then the new material we would like to study: ZnSnN₂. We showed the main advantages for photovoltaic objectives by stressing that a lot of work remains to be done for a good understanding of the material properties and for a good control of the growth process. More especially, we underlined that the crystallographic structure remains until now an open issue.

In the second chapter, we have detailed the experimental tool used for the growth: the reactive magnetron co-sputtering chamber. In addition, we described the main characterization methods used in this work.

In the first part of the third chapter we focus on the study of deposition parameters and growth process. We investigated the effect of the different deposition parameters to obtain crystallized ZnSnN₂ films such as total pressure, electrical parameters, etc... In a second part of this chapter, we show that highly crystalline ZnSnN₂ thin films can be obtained at room temperature by using a reactive co-sputtering process. Zinc tin nitride films exhibit then a strong preferential orientation in the [001] direction considering that the films crystallize in an orthorhombic structure. The film microstructure is characterized by cross-section TEM, ZnSnN₂ thin films have columnar microstructure with column width of approx. 80 nm. The chemical environment of zinc, tin and nitrogen atoms are probed by XPS, EDX and Mössbauer spectrometry. Mössbauer spectrometry clearly evidences that the main part of tin is present as Sn⁴⁺ in tetrahedral position, but Sn²⁺ is also evidenced. The occurrence of Sn²⁺ may be related to the oxide phase observed by TEM at the column boundaries. The electrical and optical

properties of the film have been investigated. The optical band gap has been measured with two methods: ellipsometry and UV –visible spectroscopy. The optical band gap is approx. 1.8 eV. In the end of this chapter, an experimental study has been done to investigate the effect of the impurities base pressure of the chamber on the structure and the microstructure of ZnSnN₂ thin films. The use of a low base pressure strongly decreases the oxygen contamination of the as-deposited films as confirmed by Mössbauer spectrometry. Thus, an improvement of the film crystallinity and of the electrical properties has been noticed.

In the first part of the last chapter, we focus on the analysis of the ZnSnN₂ thin films. We brought a new highlight to the problem of structure determination for zinc tin nitride thin film that remains an open question until now. Electron diffraction results show that both monoclinic and orthorhombic structures can be excluded. Thus, our ZnSnN₂ thin films crystallize in the hexagonal structure. The methodology developed for the first time in the present work to determine the film structure using electron diffraction is very powerful and allows to answer to one of the unsolved question about the structure of ZnSnN₂ films. In the second part, we describe the effect of the stoichiometry between zinc and tin elements on the film structure and properties. By adjusting the voltage applied to the zinc and tin targets, it was possible to obtain either stoichiometric or off-stoichiometric ZnSnN₂ films. Changing the stoichiometric ratio between the Zn and Sn atoms have a real impact on the structure and the microstructure of the films. The optical band gap has been determined as a function of the film stoichiometry. The increase of the Zn/Sn atomic ratio induces first an increase from approx. 1.8 to 1.9 eV and then a decrease up to 1.7 eV. On the other hand, the electrical resistivity tends to increase monotonously with the Zn/Sn atomic ratio. We have also studied the effect of the deposition pressure on the film properties. However, the change of the total pressure induces a change of the film stoichiometry. In order to only determine the total pressure effect, we have adjusted the target voltage to keep constant the Zn/Sn atomic ratio. The film deposited at 1 Pa exhibits a strong texture along the [001] direction of the hexagonal structure. The optical band gap has been measured using UV-visible spectrometry and ellipsometry. Both methods show an increase of the band gap when the total pressure increases from 1.0 to 3.0 Pa, the optical band gap being ranging between 1.77 to 2.19 eV. The electrical resistivity increases with the total pressure. The Hall effect measurements show the lowest value for the carrier density (approx. $5.37 \times 10^{18} \text{ cm}^{-3}$) and the highest electron mobility ($3.77 \text{ cm}^2 \text{ V}^{-1} \text{ s}^{-1}$) for ZnSnN₂ grown at 1.5 Pa.

This work brings relevant information about the elaboration and the characterization of ZnSnN₂ thin films but, further investigations seem necessary. Although we have clearly shown that our

films crystallize in a hexagonal structure we have not determined the space group of ZnSnN_2 . Measurements at the synchrotron SOLEIL would be helpful to answer to this question. Such analyses will be done before the end of 2018. In order to use zinc tin nitride as absorber in solar cells, the next step will be the elaboration of cells with p-type material. Our group has a large experience on copper-based materials that exhibit a p-type conductivity. First elaboration of solar cells will be done within the next months.

Abstract: Zinc tin nitride (ZnSnN_2) thin films have been deposited by reactive magnetron co-sputtering at room temperature. The stoichiometry of the films has been controlled by optimizing the deposition conditions such as the voltage applied to the metallic targets, the deposition pressure and the composition of the gas mixture. By using the optimized parameters, the deposited films are highly crystallized on the different used substrates. A special attention has been devoted to the determination of the film structure. Among the various structures reported in the literature, we have shown by transmission electron microscopy that the films crystallised in a hexagonal structure. Nevertheless, the structure of our films does not fit with that reported in the literature for the hexagonal ZnSnN_2 material. In addition to this structural study, we have performed fine characterization using conversion electron Mossbauer spectrometry and X-ray photoemission spectroscopy. Both methods show that the optimized films contain Sn^{4+} ions in tetrahedral configuration. Nevertheless, oxygen contamination at the column boundaries has been evidenced. The electrical and optical properties of the films have been determined has a function of the film composition. The results obtained in this PhD work clearly evidence that ZnSnN_2 is a suitable material for photovoltaic applications.

Key words: ZnSnN_2 , thin films, PVD, structural characterization, optical and electrical properties, Mossbauer spectroscopy, photovoltaic cells.

Résumé : Des films de nitrure de zinc et d'étain (ZnSnN_2) ont été élaborés par co-pulvérisation magnétron réactive à des températures proches de l'ambiante. La composition chimique des revêtements a été optimisée en ajustant les paramètres de dépôt comme la tension appliquée aux cibles métalliques, la pression de travail et la composition du gaz plasmagène. Dans les conditions optimisées, les films sont fortement cristallisés sur les différents types de substrats testés. Une étude approfondie sur la structure des films a été entreprise par microscopie électronique en transmission. Nous avons ainsi pu montrer que nos films de ZnSnN_2 cristallisent dans le système hexagonal. Toutefois, cette structure diffère de celles présentées dans la littérature pour le nitrure de zinc et d'étain. Des études sur l'environnement chimique des éléments constitutifs des revêtements ont également été menées par spectrométrie Mössbauer et par photoémission X. Elles montrent que l'étain est présent dans nos films sous forme de Sn^{4+} en configuration tétraédrique. Nous avons également pu montrer que l'oxygène présent dans nos films est principalement localisé dans les zones inter-colonnaires. Enfin, les propriétés optiques et électriques de nos films ont été estimées en fonction de leur composition chimique. L'ensemble des résultats obtenus durant ce travail démontre la pertinence de ZnSnN_2 pour des applications futures en tant que couche absorbante dans les cellules photovoltaïques.

Mots clés : ZnSnN_2 , films minces, PVD, caractérisations structurales, propriétés optiques et électriques, spectroscopie Mössbauer, cellules photovoltaïques

Résumé du travail et des principaux résultats obtenus

Au regard du réchauffement climatique et de l'utilisation des matières fossiles qui ne cesse d'augmenter, il semble nécessaire de développer de nouvelles sources d'énergie renouvelables permettant de suppléer à une partie de ces énergies fossiles. Ainsi, par exemple, dans son nouveau projet "énergie et changement climatique" de janvier 2007, la Commission Européenne a proposé de fixer, à l'échelle européenne, la part des énergies renouvelables à 20 % de la consommation globale de l'Union Européenne d'ici 2020. De nombreuses pistes sont ainsi actuellement étudiées ou en voie de développement comme, par exemple, l'énergie solaire.

L'industrie optoélectronique se développe actuellement principalement via l'utilisation de classes de matériaux spécifiques. Dans le domaine de l'éclairage, si les LED UV GaN classiques sont bien maîtrisées, il demeure important de trouver et de développer des matériaux alternatifs. Ce besoin à court également dans le domaine du photovoltaïque, l'énergie solaire constituant l'un des principaux pivots des systèmes d'énergie renouvelable du futur. Pour relever ces défis et développer de nouveaux marchés, la découverte de nouveaux matériaux est essentielle.

Les matériaux III-V sont couramment utilisés en tant que couches actives dans les LED, transistors, cellules solaires et dispositifs mécaniques. La filière principale est basée sur l'utilisation des alliages InGaN. Ces couches contiennent cependant de l'indium et du gallium. La volatilité importante de leurs prix et de leur offre au cours des dernières années a suscité de vives inquiétudes compte tenu de leurs rôles critiques et de leur utilisation dans une vaste gamme de dispositifs électroniques à grande échelle. De plus, à l'heure actuelle, les matériaux cristallins III-V nécessitent l'utilisation de techniques de croissance épitaxiales à coût élevé et à complexité importante. Par conséquent, il est important d'étudier et de développer de nouveaux matériaux abondants et aux propriétés optimisées pour la réalisation de dispositifs optoélectroniques innovants et au coût compétitif pour une production de masse.

Dans ce travail, nous visons à développer un nouveau type de matériau nitruré peu coûteux et constitué d'éléments abondants. L'étude de ce matériau innovant est ambitieuse mais a déjà débuté dans divers pays (Chine, Inde, États-Unis). Les études se concentrent sur la famille

des alliages Zn-IV-N₂ qui est prometteuse car son énergie de bande interdite pourrait couvrir le spectre solaire et remplacer ainsi avantageusement les alliages InGaN. Néanmoins, les données sur ces alliages de ZnSnN₂ restent rares et parfois contradictoires. De nombreux efforts restent à faire pour mieux comprendre ses propriétés fondamentales. Par exemple, la structure cristallographique du matériau n'est pas clairement définie. De plus, les alliages de ZnSnN₂ semblent être difficiles à contrôler par la croissance de la PVD. Tous ces aspects sont étudiés dans ce travail. Nous avons choisi d'utiliser la pulvérisation cathodique par magnétron réactif, une technique de production facilement évolutive à un coût relativement bas.

Dans le premier chapitre de ce manuscrit est décrit le vaste contexte du photovoltaïque et de quelques préoccupations connexes. Nous décrivons ensuite plus particulièrement les solutions proposées dans la littérature pour le développement de nouveaux matériaux. Parmi les suggestions récentes de la littérature, l'alliage ZnSnN₂ semble être un bon candidat. L'état de l'art de ces matériaux est ensuite abordé ainsi que les principaux les points clés du travail encore à mener.

Dans le deuxième chapitre de ce manuscrit, nous décrivons les techniques de croissance et de caractérisation utilisées au cours de ce travail de thèse et qui sont, pour la plupart, disponibles sur le site de l'Institut Jean Lamour ou est réalisé ce travail.

Le troisième chapitre est consacré à l'optimisation du procédé de croissance. Dans la première partie du troisième chapitre, nous nous concentrons sur l'étude des paramètres de dépôt et du processus de croissance. Nous avons étudié l'effet des différents paramètres de dépôt pour obtenir des films de ZnSnN₂ cristallisés tels que la pression totale, les paramètres électriques, etc. Dans une seconde partie de ce chapitre, nous montrons que des films minces de ZnSnN₂ hautement cristallins peuvent être obtenus à température ambiante en utilisant un processus de co-pulvérisation cathodique réactif. Les films de nitrure d'étain de zinc présentent alors une forte orientation préférentielle dans la direction [001] étant donné qu'ils cristallisent dans une structure orthorhombique. La microstructure du film est caractérisée par TEM en section transversale. Les films minces de ZnSnN₂ présentent une microstructure colonnaire avec une largeur de colonne d'environ 80 nm. Les environnements chimiques des atomes de zinc, d'étain et d'azote sont analysés par spectrométrie XPS, EDX et Mössbauer. La spectrométrie Mössbauer montre clairement que la majeure partie de l'étain est présente sous forme de Sn⁴⁺ en position tétraédrique, mais que Sn²⁺ existe également. L'apparition de Sn²⁺

+ peut être liée à la phase d'oxyde observée par TEM aux limites des colonnes. Les propriétés électriques et optiques du film ont été étudiées. Le gap optique d'interdiction a été mesuré selon deux méthodes: l'ellipsométrie et la spectroscopie UV-visible. La bande interdite optique est d'environ 1,8 eV. À la fin de ce chapitre, une étude expérimentale a été réalisée pour étudier l'effet de la pression de base de la chambre des impuretés sur la structure et la microstructure des films minces de ZnSnN₂. L'utilisation d'une faible pression de base diminue fortement la contamination en oxygène des films tels que déposés, comme l'a confirmé la spectrométrie Mössbauer. Ainsi, une amélioration de la cristallinité du film et des propriétés électriques a été constatée.

Dans la première partie du dernier chapitre, nous nous concentrons sur l'analyse des couches minces de ZnSnN₂. Nous apportons une contribution importante à la détermination de la structure du film mince de nitrure d'étain zinc qui reste une question ouverte à ce jour. Les résultats de la diffraction électronique montrent notamment que les structures monocliniques et orthorhombiques peuvent être exclues. Nos minces de ZnSnN₂ cristallisent ainsi dans la structure hexagonale. La méthodologie développée pour la première fois au cours de ce travail pour la détermination la structure par diffraction électronique est très puissante et permet de répondre à l'une des questions non résolues sur la structure des films de ZnSnN₂. Dans la deuxième partie, nous décrivons l'effet de la stoechiométrie entre les éléments de zinc et d'étain sur la structure et les propriétés du film. En ajustant la tension appliquée aux cibles en zinc et en étain, il a été possible d'obtenir des films de ZnSnN₂ stoechiométriques ou non stoechiométriques. La modification du rapport entre atomes de Zn et de Sn a un impact réel sur la structure et la microstructure des films. La bande interdite optique a ainsi été déterminée en fonction de la stoechiométrie du film. L'augmentation du rapport atomique Zn / Sn induit d'abord une augmentation d'environ 1,8 à 1,9 eV puis une diminution jusqu'à 1,7 eV. D'autre part, la résistivité électrique tend à augmenter de façon monotone avec le rapport atomique Zn / Sn. Nous avons également étudié l'effet de la pression de dépôt sur les propriétés du film. Le changement de la pression totale induit un changement de la stoechiométrie du film. Afin d'isoler l'effet de pression totale, nous avons ajusté la tension cible pour maintenir constant le rapport atomique Zn / Sn. Le film déposé à 1 Pa présente une texture forte le long de la direction [001] de la structure hexagonale. La bande interdite optique a été mesurée par spectrométrie UV-visible et ellipsométrie. Les deux méthodes montrent une augmentation de la bande interdite lorsque la pression totale augmente de 1,0 à 3,0 Pa, la bande interdite optique se situant

alors entre 1,77 et 2,19 eV. La résistivité électrique augmente avec la pression totale. Les mesures à effet Hall montrent la valeur minimale de densité de porteurs (environ $5,37 \times 10^{18}$ cm⁻³) et mobilité électronique maximale (3,77 cm² V⁻¹ s⁻¹) pour ZnSnN₂ élaboré à 1,5 Pa.